ISSN 2616-8170

Robotics Society of Taiwan

iRobotics

VOLUME 2
NUMBER 4
DECEMBER 2019

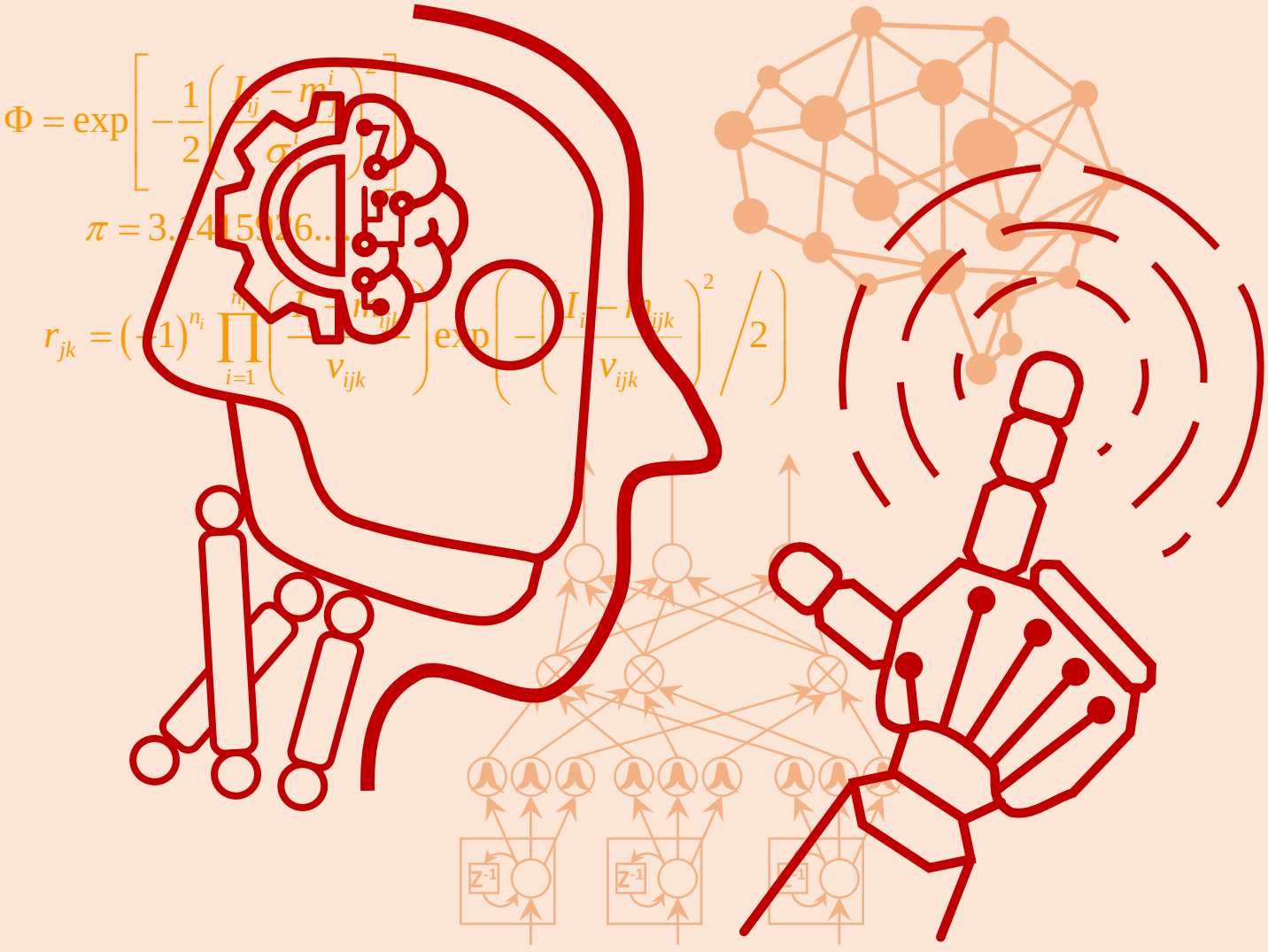

PUBLISHED BY THE ROBOTICS SOCIETY OF TAIWAN

*i*Robotics

PUBLISHER

Robotics Society of TAIWAN (RST)
Society President: Ching-Chih Tsai

Department of Electrical Engineering, National Chung Hsing University
Taichung, Taiwan

Tel: +886-4-2285-1549#601
URL: http://www.rst.org.tw

The ***i*Robotics** is published quarterly each year by the Robotics Society of Taiwan (RST). Institutional rate: US$140 annually; individual annual subscription rate: US$50 for nonmembers, US$25 for members (including postage). Note that another US$100 is needed if the express is required.

Robotic Calligraphy System Using Delta-like Robot Manipulator and Virtual Brush Model

Yi-Hsing Chien, Min-Jie Hsu, Li-An Yu, Wei-Yen Wang, *Fellow, RST*, and Chen-Chien Hsu

***Abstract*—In this paper, a virtual brush model based on a Delta-like robot manipulator is presented to obtain the coordinates to draw Chinese character calligraphy. The aim of this research topic is to develop and promote cross-cultural technology integration. Although in recent years there has been an increase in the research and development of a virtual calligraphy-writing system, work in this field is still rather limited. In our mechanism system, we design a Delta-like robot manipulator with hybrid kinematic structure to simultaneously maintain both stabilities and accuracies. Moreover, to interpret and analyze the deformation of the brush appropriately, we adopt a tool of droplet operation. Finally, the results of drawing a Chinese character calligraphy "永", which means eternal, validate the effectiveness of the proposed robotic calligraphy system.**

***Index Terms*—Robotic calligraphy system, Delta-like robot manipulator, virtual brush model, Chinese character calligraphy.**

I. Introduction

In the last few decades, various studies of robotic calligraphy system ware discussed in [1-13]. One of the related research topics is virtual brush model [1-8]. Yao et al. [1] analyzed the trajectory extraction method of the writing-brush in Chinese character calligraphy using image and curve processing techniques and the calligraphy knowledge. In [2], modeling of ancient-style Chinese character was presented. Firstly, the Chinese character skeleton was detected from the thinned image. Then the skeleton was modeled by B-splines functions. Fujioka et al. [3] developed a scheme for generating cursive characters by employing a function approximation method in control theory. Similarly, characters were acquired as the trace of virtual writing-brush. Although they only considered Japanese Kana characters, the method should be suitable for other languages as well. Nevertheless, these approaches only focus on stroke trajectories but do not consider the geometric information of the Chinese characters in detail.

In [4], a parameterized physical brush model was proposed and this model utilized a simplified evaluation algorithm to approximate the effect while maintaining the ability to express most of the special effects of Chinese calligraphy. The papers by Chu et al. [5, 6] presented a brush model consisting of a skeleton and a surface, which is deformed through constrained energy minimization. This model can imitate brush flattening and bristle spreading by reason of brush bending and lateral friction during the drawing process. Subsequently, Bai et al. [7] developed a framework which consists of brush geometry model and brush dynamic motion model. Several points were utilized to simulate the brush bundle, and this scheme can effectively decrease the complexity inherent in the conventional bristle-level method. Wong et al. [8] focused on calligraphic image analysis. They described a statistical-based approach for automatically constructing parameters of virtual brush model. However, all of the work above focused on synthesizing Chinese character calligraphy rather than aimed at combining mathematical model theory with hardware devices.

In past studies [9-13], some hardware approaches were presented to implement the robotic calligraphy system. A part of researches focused on constructing robot mechanism based on XYZ linear stage in the calligraphy-writing system. For instance, Man et al. [9] proposed a machinery arm which is a XYZ-coordinate axis system. When drawing a Chinese character calligraphy, the moving track of the machinery arm is a continuous curve including many points in space. Lo et al. [10] constructed a robot drawing platform which consists of a x-y-z axis translational mechanism and a robot gripper with a z-axis rotation degree. By using this platform, they presented some preliminary results of the footprint analysis and nonparametric modeling of Chinese calligraphy. In [11], a robotic calligraphy system with a delta-like parallel manipulator was developed and it can automatically modify the motion of the robotic arm using image process techniques for drawing Chinese calligraphy. However, the above hardware mechanisms cannot effectively imitate human wrist movement. Hence, the results of calligraphy-writing were not good enough. In order to improve the manipulability of the robot, Sun et al. [12] developed a calligraphy robot with a 6-DOF series robotic arm. This robotic arm could mimic the motion of human calligraphy writing. In [13], a KUKA lightweight robot (LWR) with an attached camera was utilized to demonstrate the results of Chinese characters writing. However, the stroke analysis of the virtual brush model is a lack of their approaches.

This paper is an attempt to supplement the findings of these earlier studies. Firstly, a novel virtual brush model based on droplet operation is proposed and it addresses some limitations including character and style. Therefore, we can draw the current Chinese character calligraphy from textbooks and construct new characters. On the other hand, the proposed model theory only utilizes simple mathematical operation and does not take much time to calculate complex parameters for synthesizing Chinese character. Moreover, we improve the previous proposed robot mechanism [11] with Delta-like robot manipulator to yield a total of 5-DOF for the brush pen movement. Because of the parallel closed-chain designed, the overall rigidity of the machine is stronger and the inertia of movements is smaller as well than series robot manipulator. Besides, the lower stages of our robot manipulator can tilt the brush pen to realistically mimic the calligraphy posture.

Wei-Yen Wang, Yi-Hsing Chien, Min-Jie Hsu, Li-An Yu, and Chen-Chien Hsu are with the Department of Electrical Engineering, National Taiwan Normal University, Taipei, 106, Taiwan.

The authors deeply acknowledge finance support from the Ministry of Science and Technology (MOST), Taiwan, ROC, under contract MOST 108-2634-F-003-002 and MOST 108-2634-F-003-003

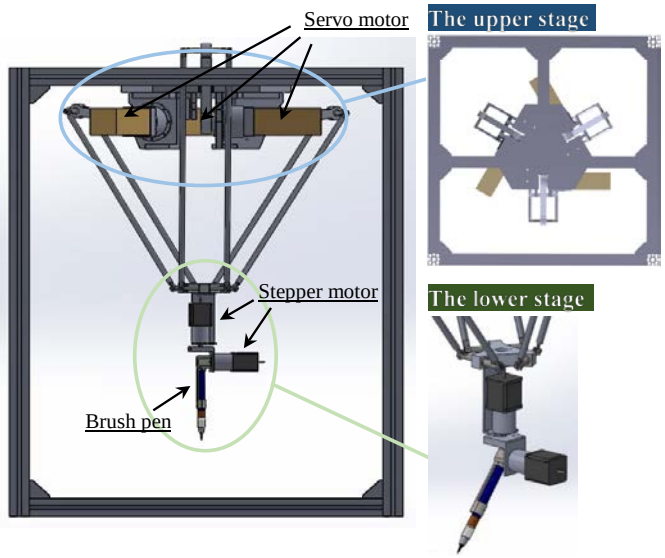

Figure 1. 3D layouts of the mechanical system.

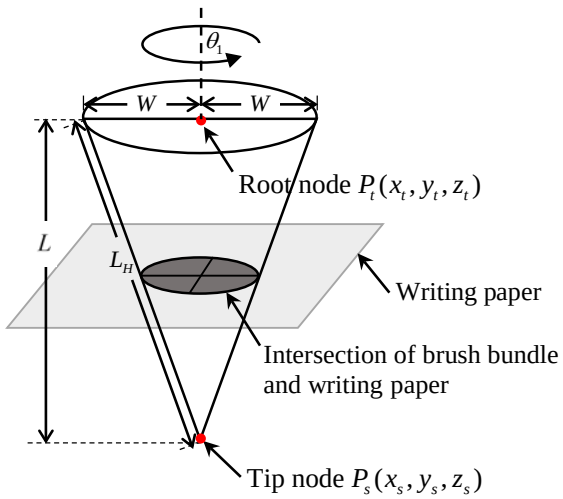

Figure 2. Brush bundle in normal state [8, 14].

The rest of this paper is organized as follows. Section II demonstrates the configuration of our mechanical system. Section III presents a virtual brush model based on droplet operation. Section IV reveals the simulation results to verify the performances of the proposed robotic calligraphy system. The conclusions of this paper are given in Section V.

II. Configuration of Mechanical System

In this section, we introduce a mechanism of delta-like robot manipulator with serial-parallel design. Firstly, because SolidWorks offers complete 3D software tools, it is utilized to design the whole mechanical structure. Fig. 1 demonstrates the 3D layouts of the proposed Delta-like robot manipulator.

The actuating modules are disposed on the upper stage, and they are connected to the lower stage respectively to drive the lower stage. Each of the actuating modules includes an actuator, a transmission element, a shaft, a coupler and a pair of bearings. The actuator is disposed on the upper stage and includes an output shaft. The transmission element connects the actuator with the lower stage. The shaft is joined to the transmission element. The bearings are disposed on the upper stage and they are utilized to support the shaft. The coupler connects the output shaft and the shaft.

Because the joint of delta-like robot manipulator requires full degree of freedom in ideal, there should be two-axes rotation at least. Ball joint is easy to implement for dealing with full degree of freedom, but that causes the material wear away faster. In order to increase the stability of whole structure, replacing the ball joint with other design is necessary. We adopt the combination of two mechanisms which have two-axis rotation as our joint instead of ball joint. The first mechanism is a cylinder connected to the lower arm, and we utilize ball bearings for each one-axis rotation. In order to hold the rotational cylinder, we utilize four snap rings to prevent this mechanism from sliding. The other mechanism connects the rotational cylinder to under platform with ball bearings, and we also hold the rotational cylinder with snap rings to prevent the mechanism from mechanical vibration and sliding. Using these two mechanisms design, both stability and durability of the proposed robot manipulator are increased.

III. A Virtual Brush Model Based on Droplet Operation

The brush model can be roughly implemented through the shape of the brush bundle, the brush stem orientation, and the three-dimensional brush motion [8, 14]. Based on the earlier studies, we design a novel brush model consists of three components, that is, brush geometry, brush dynamics, and combination of droplets. The details are presented in the following sub-sections.

A. Brush geometry

Firstly, the physical properties of the brush bundle are modelled to benefit synthesis of Chinese character calligraphy. It is similar to the previous studies [15-17], in that we define the center point of the upper stage shown in Fig. 1 as origin. Fig. 2 demonstrates the brush bundle in normal state. The major parameters utilized in this model are the radius W, height of the brush bundle L, length of brush bundle L_H, root node $P_t(x_t, y_t, z_t)$, tip node $P_s(x_s, y_s, z_s)$, and angle of rotation θ_1.

B. Brush dynamics

In the brush dynamic motion model, the intersection of the brush bundle and the writing paper is modelled utilizing a droplet whose principal axes can be dynamically adjusted by motor control of the upper and lower stages of the proposed Delta-like robot manipulator. The diagram of brush-paper intersection in painting state is shown in Fig. 3. The major parameters in this model are the instantaneous positions of the tip node $P_s(x_s, y_s, z_s)$ and the brush belly nodes $P_e(x_e, y_e, z_e)$, $P_r(x_r, y_r, z_r)$, and $P_l(x_l, y_l, z_l)$, which is the set of semi-ellipse parameters on the writing paper. Moreover, to realistically mimic the calligraphy posture, the brush pen in the dynamic motion model can be tilted an angle θ_2. Incidentally, according to the position of the point P_t, the rotation angle θ_1, and the tilted angle θ_2, many different shapes and sizes of virtual droplets can be product.

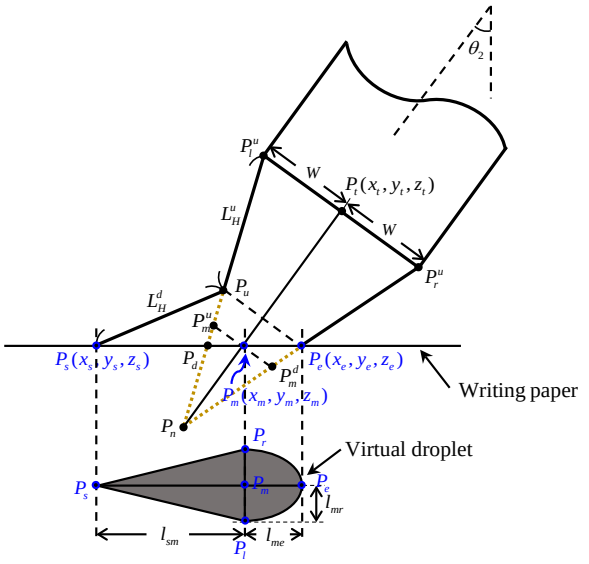

Figure 3. Brush bundle in painting state.

After that, we define the center of the semi-ellipse as $P_m(x_m, y_m, z_m)$, and the formulae below are utilized to compute the radii l_{mr} and l_{me} of the semi-ellipses.

$$l_{mr} = W - \frac{W}{L}(z_t - z_m)\sec\theta_2 \tag{1}$$

$$\begin{aligned} l_{me} &= (z_t - z_m)\tan\theta_2 + W\cos\theta_2 \\ &\quad -(z_t - z_m - W\sin\theta_2)\cot\left(\tan^{-1}\left(\frac{L}{W}\right) - \theta_2\right) \end{aligned} \tag{2}$$

As shown in Fig. 3, the shape of droplet in the virtual brush model can be clearly looked upon the combination of a semi-ellipse and a triangle. The line segments $\overline{P_l P_r} = 2l_{mr}$ and $\overline{P_s P_m} = l_{sm}$ are defined as the base and the height of the triangle, respectively. The formulae of l_{sm} are shown in (3)-(5).

$$\begin{aligned} l_{sm} &= L_H^u \sin\left(\tan^{-1}\left(\frac{L}{W}\right) - 90^\circ + \theta_2\right) \\ &\quad + W\cos\theta_2 - (z_t - z_m)\tan\theta_2 \\ &\quad + \sqrt{\left(L_H^d\right)^2 - \left(\begin{array}{l} z_t - z_m + W\sin\theta_2 \\ -L_H^u\cos\left(\tan^{-1}\left(\frac{L}{W}\right) - 90^\circ + \theta_2\right) \end{array}\right)^2} \end{aligned} \tag{3}$$

where

$$L_H^u = (z_t - z_m - W\sin\theta_2)\csc\left(\tan^{-1}\left(\frac{L}{W}\right) - \theta_2\right) \tag{4}$$

$$\begin{aligned} L_H^d &= \sqrt{L^2 + W^2} - L_H^u \\ &= \sqrt{L^2 + W^2} - (z_t - z_m - W\sin\theta_2)\csc\left(\tan^{-1}\left(\frac{L}{W}\right) - \theta_2\right) \end{aligned} \tag{5}$$

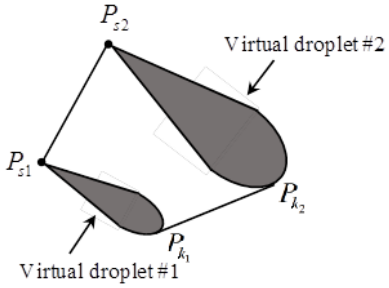

Figure 4. Diagram of combination of two adjacent droplets.

C. *Combination of droplets*

After the virtual parameterized droplet model is well-defined, we can simulate the Chinese character calligraphy by merging a number of virtual droplets. As mentioned in the previous sub-section, the shape of droplet can be looked upon the combination of a semi-ellipse and a triangle. When merging droplets, it is a significant step for combining two semi-ellipses. The diagram of combination of two adjacent droplets is illustrated in Fig. 4.

Firstly, we suppose two complete ellipse formulae as follows:

$$\tau_a x^2 + \tau_b xy + \tau_c y^2 + \tau_d x + \tau_e y + \tau_f = 0 \tag{6}$$

and

$$\tau_g x^2 + \tau_h xy + \tau_i y^2 + \tau_j x + \tau_k y + \tau_l = 0 \tag{7}$$

The common tangent line is defined as $y=Mx+N$, and the above equations are rewritten as

$$\begin{aligned} &\tau_a x^2 + \tau_b x(Mx+N) + \tau_c (Mx+N)^2 \\ &\quad + \tau_d x + \tau_e (Mx+N) + \tau_f = 0 \end{aligned} \tag{8}$$

and

$$\begin{aligned} &\tau_g x^2 + \tau_h x(Mx+N) + \tau_i (Mx+N)^2 \\ &\quad + \tau_j x + \tau_k (Mx+N) + \tau_l = 0 \end{aligned} \tag{9}$$

Because the discriminant functions of (8) and (9) both equal to 0, the above equations are rewritten as

$$\begin{aligned} &(\tau_b N + 2\tau_c MN + \tau_d + \tau_e M)^2 \\ &-4(\tau_a + \tau_b M + \tau_c M^2)(\tau_c N^2 + \tau_e N + \tau_f) = 0 \end{aligned} \tag{10}$$

and

$$\begin{aligned} &(\tau_h N + 2\tau_i MN + \tau_j + \tau_k M)^2 \\ &-4(\tau_g + \tau_h M + \tau_i M^2)(\tau_i N^2 + \tau_k N + \tau_l) = 0 \end{aligned} \tag{11}$$

After that, solving simultaneous equations (10) and (11), we obtain the exterior common tangents of the two ellipses. Due to the known positions of two tip nodes P_{s1} and P_{s2} as shown in Fig. 4, the points P_{k1} and P_{k2} of tangency can be derived. Then we can combine two adjacent droplets to synthesize Chinese character calligraphy. Finally, using the proposed droplet operations, various kinds of character calligraphies in different styles can be synthesized and simulated in our virtual brush model.

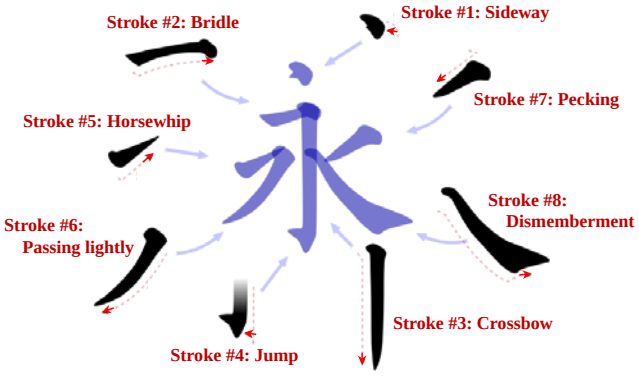

Figure 5. The Chinese character "永" [19].

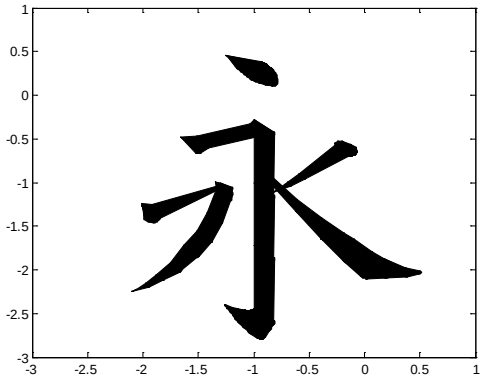

Figure 6. The simulation results using the proposed robotic calligraphy system.

IV. Simulation Results

The ancient scholars divided all Chinese characters into six categories [18], that is, pictographs, ideographic, compound ideographs, phono-semantic compound characters, rebus (phonetic loan) characters, and derivative cognates. No matter which categories, these characters can be constructed of one or several strokes. Because the Chinese character "永" includes eight common strokes, we utilize this character to verify the performance of our virtual brush model. For this character, we separate the sequence numbers and stroke directions in red shown in Fig. 5.

The proposed virtual brush model is implemented on Windows platform, and the programming language is MATLAB. The major parameters of this model are shown as: the radius of brush bundle W=2.5 mm, length of brush bundle L=16 mm, and length of brush shaft l_p=25 cm. The size of self-made Delta-like robot manipulator is 75 cm in length × 75 cm in width × 90 cm in height. The distance $|z_m|$ from the upper stages of the robot manipulator to blank paper is set as 83 cm. The size of the brush-writable area is set as 50 cm in length × 50 cm in width. Currently, we select eight classes (i.e., sideway, bridle, crossbow, jump, horsewhip, passing lightly, pecking, and dismemberment) for stroke patterns of the Chinese character calligraphy. Some simulation results are shown in Figs. 6-14. The results reflected in Fig. 6 present a successful implementation of drawing Chinese character calligraphy in regular script. Figs. 7-14 demonstrate the eight classes for stroke patterns and the values of the corresponding parameters, i.e., x_t, y_t, z_t, θ_1, and θ_2.

As observed in simulation results, the proposed robotic calligraphy system can guide users to obtain the suitable coordinates of the brush bundle center to draw elegant Chinese character calligraphy or calligraphy similar to copybook template.

V. Conclusion

In this paper, we present the results of drawing Chinese character calligraphy with the delta-like robot manipulator in virtual writing environment. This self-made virtual environment is a tool that helps users to more quickly design suitable parameters for robot manipulator than directly operating equipment. A simplified and effective virtual brush model based on droplet operation is proposed. The layout of droplets is the major feature of the model. Finally, simulation results indicate the effectiveness and applicability of the proposed robotic system for drawing Chinese character calligraphy.

Acknowledgment

This work was financially supported by the "Chinese Language and Technology Center" of National Taiwan Normal University (NTNU) from The Featured Areas Research Center Program within the framework of the Higher Education Sprout Project by the Ministry of Education (MOE) in Taiwan, and Ministry of Science and Technology, Taiwan, under Grants no. MOST 108-2634-F-003-002 and MOST 108-2634-F-003-003 through Pervasive Artificial Intelligence Research (PAIR) Labs. We are grateful to the National Center for High-performance Computing for computer time and facilities to conduct this research.

References

[1] F. Yao, G. Shao, and J. Yi, "Extracting the Trajectory of Writing Brush in Chinese Character Calligraphy," Engineering Applications of Artificial Intelligence, vol. 17, no. 6, pp. 631-644, Sept. 2004.

[2] F. Yao and G. Shao, "Modeling of Ancient-style Chinese Character and Its Application to CCC Robot," in Proc. of the 2006 IEEE International Conference on Networking, Sensing and Control, Aug. 2006.

[3] H. Fujioka, H. Kano, H. Nakata, and H. Shinoda, "Constructing and Reconstructing Characters, Words, and Sentences by Synthesizing Writing Motions," IEEE Trans. on Systems, Man, and Cybernetics-Part A: Systems and Humans, vol. 36, no. 4, pp. 661-670, July 2006.

[4] X.-F. Mi, M. Tang, and J.-X. Dong, "Droplet: A Virtual Brush Model to Simulate Chinese Calligraphy and Painting," Journal of Computer Science and Technology, vol. 19, no. 3, pp. 393-404, May 2004.

[5] N. S.-H. Chu and C.-L. Tai, "An Efficient Brush Model for Physically-Based 3D Painting," in Proc. of the 10th Pacific Conference on Computer Graphics and Applications, Oct. 2002.

[6] N. S.-H. Chu and C.-L. Tai, "Real-Time Painting with an Expressive Virtual Chinese Brush," IEEE Computer Graphics and Applications, vol. 24, no. 5, pp. 76-85, 2004.

[7] B. Bai, K.-W. Wong, and Y. Zhang, "A Virtual Chinese Hairy Brush Model for E-Learning," in Proc. of the International Conference on Web-Based Learning, Aug. 2007, pp. 320-330.

[8] S. T. S. Wong, H. Leung, and H. H. S. Ip, "Model-based Analysis of Chinese Calligraphy Images," Computer Vision and Image Understanding, vol. 109, pp. 69-85, 2008.

[9] Y. Man, C. Bian, H. Zhao, C. Xu, and S. Ren, "A Kind of Calligraphy Robot," in Proc. of the 3rd International Conference on Information Sciences and Interaction Sciences, June 2010, pp. 635-638.

[10] K. W. Lo, K. W. Kwok, S. M. Wong, and Y. Yam, "Brush Footprint Acquisition and Preliminary Analysis for Chinese Calligraphy using a Robot Drawing Platform," in Proc. of the 2006 IEEE/RSJ International Conference on Intelligent Robots and Systems, Oct. 2006.

[11] M.-J. Hsu, Y.-H. Chien, W.-Y. Wang, and C.-C. Hsu, "Design and Implementation of Robotic Calligraphy System," in Proc. of the 2017 International Conference on Advanced Robotics and Intelligent Systems, Sept. 2017.

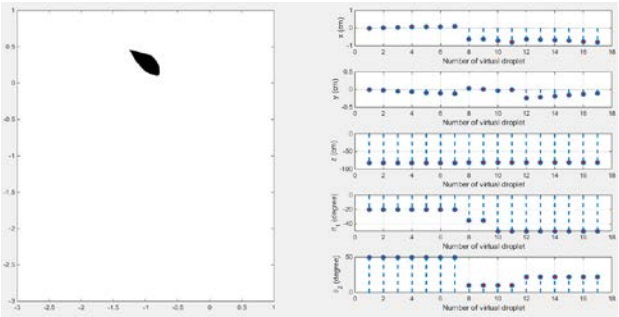

Figure 7. The values of the corresponding parameters for stroke pattern "sideway".

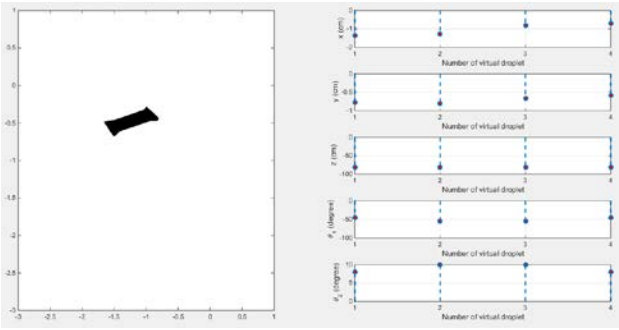

Figure 8. The values of the corresponding parameters for stroke pattern "bridle".

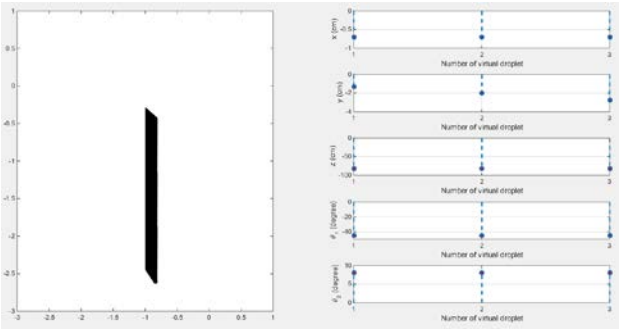

Figure 9. The values of the corresponding parameters for stroke pattern "crossbow".

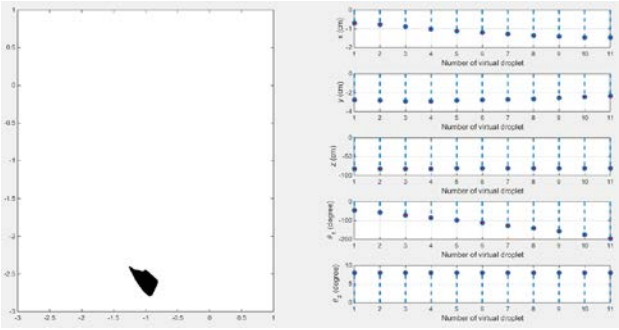

Figure 10. The values of the corresponding parameters for stroke pattern "jump".

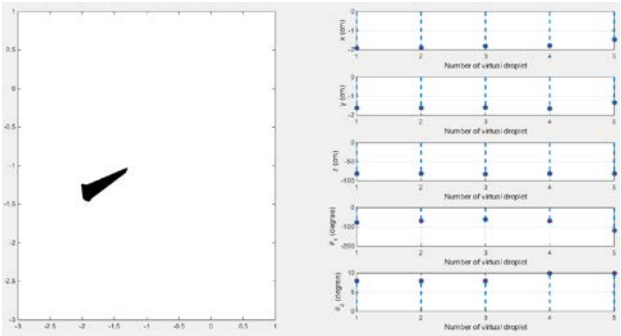

Figure 11. The values of the corresponding parameters for stroke pattern "horsewhip".

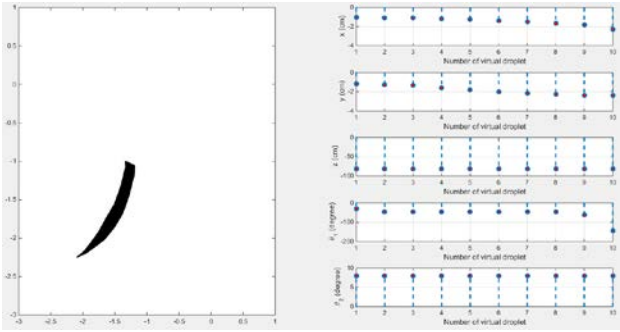

Figure 12. The values of the corresponding parameters for stroke pattern "passing lightly".

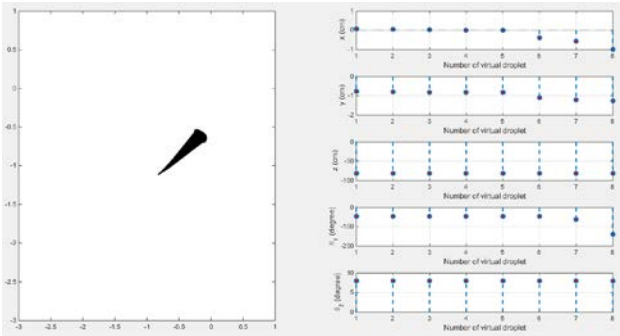

Figure 13. The values of the corresponding parameters for stroke pattern "pecking".

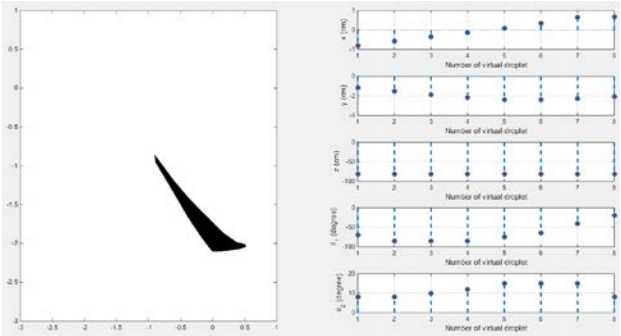

Figure 14. The values of the corresponding parameters for stroke pattern "dismemberment".

[12] Y. Sun and Y. Xu, "A Calligraphy Robot - Callibot: Design, Analysis and Applications," in Proc. of the 2013 IEEE International Conference on Robotics and Biomimetics, Dec. 2013, pp. 185-190.
[13] N. Huebel, E. Mueggler, M. Waibel, and R. D'Andrea, "Towards Robotic Calligraphy," in Proc. of the 2012 IEEE/RSJ International Conference on Intelligent Robots and Systems, Oct. 2012, pp. 5165-5166.
[14] H. T. F. Wong and H. H. S. Ip, "Virtual Brush: A Model-Based Synthesis of Chinese Calligraphy," Computers & Graphics, vol. 24, no. 1, pp. 99-113, Feb. 2000.
[15] C. R. Boër, L. Molinari-Tosatti, and K. S. Smith, "Parallel Kinematic Machines: Theoretical Aspects and Industrial Requirements," Springer Verlag, Sept. 1999.
[16] L.-W. Tsai, "Robot analysis: the mechanics of serial and parallel manipulators," Wiley-Interscience, Feb. 1999.
[17] C.-Y. Tzou, M.-J. Hsu, J.-Z. Jian, Y.-H. Chien, W.-Y. Wang, and C.-C. Hsu, "Mathematical analysis and practical applications of a serial-parallel robot with delta-like architecture," International Journal of Engineering Research & Science, vol. 2, no. 5, pp. 80-91, May 2016.
[18] Wikipedia, Chinese character classification, Available: https://en.wikipedia.org/wiki/Chinese_character_classification
[19] Wikipedia, Eight Principles of Yong, Available: https://en.wikipedia.org/wiki/Eight_Principles_of_Yong.

Yi-Hsing Chien was born in Taipei, Taiwan, in 1978. He received the M.S. degree in electrical engineering from Fu-Jen Catholic University, Taipei, Taiwan, in 2007, and Ph.D. degree in electrical engineering from the National Taipei University of Technology, Taipei, in 2012. He is currently a Postdoctoral Researcher with the Department of Electrical Engineering, National Taiwan Normal University, Taipei. His current research interests and publications are in the areas of fuzzy logic control, robust adaptive control, machine learning, and neural networks.

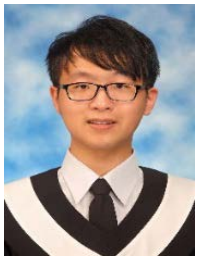

Min-Jie Hsu was born in Taipei, Taiwan, in 1993. He received the B.S. degree in electrical engineering from National Taiwan Normal University, Taipei, Taiwan, in 2015. He is currently pursuing his Ph.D. degree in the department of electrical engineering, National Taiwan Normal University, Taipei, Taiwan. His research interests include artificial intelligence, fuzzy logic system, neural network, and reinforcement learning.

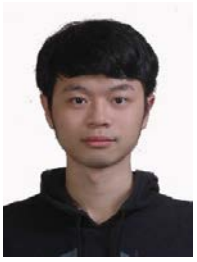

Li-An Yu received his B.S. and M.S. degrees in electrical engineering from National Taiwan Normal University, Taipei, Taiwan, in 2015 and 2017, respectively. His expertise includes neural networks and computer vision. He is currently a postgraduate research assistant in the Computational Intelligence Lab at National Taiwan Normal University in Taiwan, where he is involved in Artificial Intelligence design.

Wei-Yen Wang received the Diploma in electrical engineering from National Taipei Institute of Technology, the M.S. and Ph.D. degrees in electrical engineering from National Taiwan University of Science and Technology, Taipei, Taiwan, in 1984, 1990 and 1994, respectively.

From 1990 to 2006, he worked concurrently as a patent screening member of the National Intellectual Property Office, Ministry of Economic Affairs, Taiwan. Since 2003, he has been certified as a patent attorney in Taiwan. In 1994, he was appointed as Associate Professor in the Department of Electronic Engineering, St. John's and St. Mary's Institute of Technology, Taiwan. From 1998 to 2000, he worked in the Department of Business Mathematics, Soochow University, Taiwan. From 2000 to 2004, he was with the Department of Electronic Engineering, Fu-Jen Catholic University, Taiwan. In 2004, he became a Full Professor of the Department of Electronic Engineering, Fu-Jen Catholic University. In 2006, he was a Professor and Director of the Computer Center, National Taipei University of Technology, Taiwan. From 2007 to 2014, he was a Professor with the Department of Applied Electronics Technology, National Taiwan Normal University, Taiwan. From 2011 to 2013, he was the Director of the Information Technology Center, National Taiwan Normal University, Taiwan. Currently, he is a Professor with the Department of Electrical Engineering, National Taiwan Normal University, Taiwan. His current research interests and publications are in the areas of fuzzy logic control, robust adaptive control, neural networks, computer-aided design, digital control, and CCD camera based sensors. He has authored or coauthored over 200 refereed conference and journal papers in the above areas.

Dr. Wang is currently serving as an Associate Editor of the IEEE Transactions on Cybernetics, an Associate Editor of the International Journal of Fuzzy Systems. He is an IEEE Fellow, IET Fellow, and a recipient of Best Associate Editor Award of IEEE Transactions on Cybernetics.

Chen-Chien Hsu was born in Hsinchu, Taiwan. He received the B.S. degree in electronic engineering from National Taiwan University of Science and Technology, Taipei, Taiwan, the M.S. degree in control engineering from National Chiao-Tung University, Hsinchu, and the Ph.D. degree from the School of Microelectronic Engineering, Griffith University, Brisbane, Australia, in 1987, 1989, and 1997, respectively.

He was a Systems Engineer with IBM Corporation, Taipei, for three years, where he was responsible for information systems planning and application development, before commencing his Ph.D. studies. He joined the Department of Electronic Engineering, St. Johns University, Taipei, as an Assistant Professor, in 1997, and was appointed as an Associate Professor in 2004. From 2006 to 2009, he was with the Department of Electrical Engineering, Tamkang University, Taipei. He is currently a Professor with the Department of Electrical Engineering, National Taiwan Normal University, Taipei. He is an IET fellow and the author or co-author of more than 180 refereed journal and conference papers. His current research interests include digital control systems, evolutionary computation, vision-based measuring systems, sensor applications, and mobile robot navigation.

Performance Comparisons of Visual Servoing Structures for Industrial Robot Manipulators

Ting-Yu Chang, Wei-Che Chang, Ming-Yang Cheng and Shih-Sian Yang

***Abstract*—Visual servoing systems can be found in many real world applications. Classical visual servoing structures can be categorized into two types – Position-Based Visual Servoing (PBVS) and Image-Based Visual Servoing (IBVS). However, image noise and inaccurate camera calibration can all affect the performance of visual servoing systems. In addition, the sampling rate of the outer visual loop is much lower than the sampling rate of the inner servo control loop in a visual servoing system. All the above factors make the design of PBVS and IBVS structures a challenging task. In order to alleviate the aforementioned issue, many approaches have been proposed, with most of them focused on obtaining a better interaction matrix through different feature selection methods or improving control performance through trajectory planning. Among these existing approaches, the 6D visual servoing (6DVS) structure claims to have better control performance than the classical IBVS structure. In this paper, a 6-DOF industrial robot manipulator is used as a test platform to compare the performance of 6DVS and classical IBVS. Experimental results indicate that the 6DVS structure indeed exhibits better control performance than the classical IBVS structure.**

***Index Terms*—Image-Based Visual Servoing, 6D Visual Servoing, camera calibration, industrial robot manipulator**

I. Introduction

As the CPU's computing power keeps increasing, the applications of control systems equipped with computer vision have attracted much attention and enjoyed tremendous success recently. In particular, a robotic system equipped with computer vision can be found in a variety of applications such as industrial manufacturing, medical robots, mobile robots, etc. In the automation industry, one of the most common applications of control systems equipped with computer vision is the pick-and-place task of stationary objects or the guiding of a robot arm to a specified location. In these applications, the Look-then-Move approach [1] is sufficient. However, in many application scenarios such as picking something up on a moving belt with a varying speed or on a rocking crane, and contour following control using vision feedback, the Look-then-Move approach is insufficient. In these cases, visual servoing – a scheme that uses real-time vision feedback to implement a closed loop control system – is essential. Although visual servoing systems have many attractive features, their performance have been affected by factors such as image noise, camera calibration error, hand-eye calibration error, etc. In addition, generally, the sampling rate for the outer visual loop is much lower than that for the inner servo control loop in a visual servoing system. That is, the performance of a visual servoing system is limited. As a result, the issue of improving control performance, robustness and system response of a visual servoing system is a crucial research topic and deserves more study. Many existing researches focus on obtaining a better interaction matrix through proper feature selection or performing trajectory/motion planning to attain better control performance, while several studies take system dynamics into consideration for their visual servoing structure design.

The idea of visual servoing was proposed by Hill et. al [1]. Hutchinson et. al conducted an in-depth investigation on two classical visual servoing structures –IBVS (Image Based Visual Servoing) and PBVS (Position Based Visual Servoing) in their renowned tutorial paper in 1996 [2]. Since then, visual servoing has enjoyed huge success in various fields of applications. Later on, Chaumette et al. studied several visual servoing structures other than IBVS and PBVS [3,4], while stability analysis of IBVS and PBVS was provided in [5,6]. In addition to IBVS and PBVS, visual servoing structures such as hybrid visual servoing [7~9], partition visual servoing [10], and switching visual servoing [10,11], have been proposed as well. Futhermore, researchers also study the issue of feature selection on the performance improvement of visual servoing. For instance, Tahri et al. used the image moment as the image feature [12]; Xu et al. used point, line and surface as the image features [13]; and Cai et al. used self-defined orthogonal image features [14]. In [15], the acceleration command directly obtained from image features was used. In order to ameliorate the poor dynamic response due to the low sampling rate of visual serrvoing applications, some researchers exploited the acceleration command which is computed directly from the image information [16].

When implementing the IBVS scheme, the depth value of the feature point is essential in calculating the image Jacobian. One of the simplest methods for estimating depth value is to use a binocular camera and the concept of disparity. However, its drawback is not being computationally efficient. In order to cope with this difficulty, a method that exploits information such as position/velocity of a feature point and camera velocity to estimate depth value was proposed in [17]. A nonlinear observer was adopted in [18] to estimate the depth values of

T.-Y. Chang was with the Department of Electrical Engineering, National Cheng Kung University, Tainan 701, Taiwan (e-mail: tom0917952503@gmail.com).

W.-C. Chang is with t the Department of Electrical Engineering, National Cheng Kung University, Tainan 701, Taiwan (e-mail: wythe.c.77@gmail.com).

M.-Y. Cheng is with the Department of Electrical Engineering, National Cheng Kung University, Tainan 701, Taiwan (e-mail: mycheng@mail.ncku.edu.tw).

S.-S. Yang is with the Department of Electrical Engineering, National Cheng Kung University, Tainan 701, Taiwan (e-mail: austin9109@gmail.com)

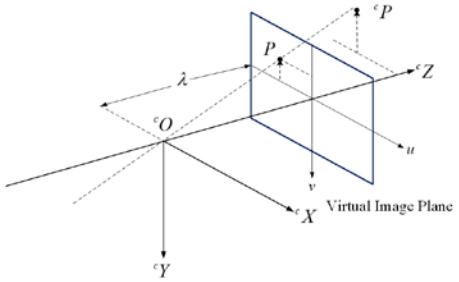

Figure 1. Virtual image plane in perspective projection.

feature points. In order to deal with the collision avoidance problem and the physical constraints on the rotation angle in the joint space, trajectory planning and optimization was performed in [19,20].

In addition to the aforementioned issues concerning visual servoing structures, several studies have focused on the control design of visual servoing systems [21-34]. For instance, Corke et al. [21] investigated the dynamics issue of a visual servoing system, in which the idea of feedforward control is exploited to cope with the vision latency problem; fuzzy logic is exploited to design visual servoing control laws [22-24]; iterative learning control was incorporated into the control design of visual servoing systems [25,26]; Other methods such as Q-learning [27-29], sliding mode control [30,31] and Kalman filter [32-34] are also adopted in the control design of visual servoing systems.

Among the existing approaches concerning the design of visual servoing structures, the 6DVS structure has been reported to exhibit satisfactory performance. In order to facilitate the use of the visual servoing structure, a 6-DOF industrial robot manipulator is used as a test platform to compare the performance of 6DVS and classical IBVS in this paper. Experimental results indicate that the 6DVS structure indeed exhibits better control performance than the classical IBVS structure.

The remainder of the paper is organized as follows. Section Ⅱ briefly reviews the camera model and hand-eye calibration. Section Ⅲ provides an introduction to the classical IBVS structure, while the 6DVS structure is elaborated in Section Ⅳ. Experimental results and conclusions are given in Section Ⅴ and Section Ⅵ, respectively.

II. Brief Review on Camera Model and Hand-Eye Calibration

A. Camera Model

Perspective projection (i.e. pin-hole model) [35,36] is adopted in this paper. In order not to have an inverted image, a virtual image plane which is located between the optical center and the object point is used. The corresponding image point is denoted as $p(u,v)$, as shown in Fig. 1.

1) Intrinsic Camera Parameters

Intrinsic camera parameters describe the relationship between the coordinate of the object point ${}^{c}P = [{}^{c}X,\ {}^{c}Y,\ {}^{c}Z]^{T}$ in the camera frame and the coordinate of the corresponding image point $p(u,v)$ on the image plane. Based on perspective projection (i.e. Fig.1), one will have

$$\begin{bmatrix} u \\ v \\ 1 \end{bmatrix} = \frac{1}{{}^{C}Z}\begin{bmatrix} \lambda & 0 & 0 \\ 0 & \lambda & 0 \\ 0 & 0 & 1 \end{bmatrix}\begin{bmatrix} {}^{C}X \\ {}^{C}Y \\ {}^{C}Z \end{bmatrix} \tag{1}$$

where λ is the focus length.

However, in practice, the width and height of a pixel may not be the same. It is reasonable to assume that the focus length for the horizontal axis (u axis) and the focus length for the vertical axis (v axis) are different. In addition, due to imperfections in the manufacturing process, the angle between the horizontal axis and the vertical axis may not be 90°. In general, a skew factor is used to describe this phenomenon. Based on the above discussions, Eq. (1) can be rewritten as

$$\begin{bmatrix} u \\ v \\ 1 \end{bmatrix} = \frac{1}{{}^{C}Z}\begin{bmatrix} \lambda_x & \delta & 0 \\ 0 & \lambda_y & 0 \\ 0 & 0 & 1 \end{bmatrix}\begin{bmatrix} {}^{C}X \\ {}^{C}Y \\ {}^{C}Z \end{bmatrix} \tag{2}$$

where λ_x is the focus length for the horizontal direction; λ_y is the focus length for the vertical direction; and δ is the skew factor. Moreover, in order not to have negative pixel coordinates, the origin of the image plane will be moved to the upper left corner instead of the center position. As a result, Eq. (2) can be further rewritten as

$$\begin{bmatrix} u \\ v \\ 1 \end{bmatrix} = \frac{1}{{}^{C}Z}\begin{bmatrix} \lambda_x & \delta & u_0 \\ 0 & \lambda_y & v_0 \\ 0 & 0 & 1 \end{bmatrix}\begin{bmatrix} {}^{C}X \\ {}^{C}Y \\ {}^{C}Z \end{bmatrix} \tag{3}$$

The values of intrinsic camera parameters can be obtained by performing camera calibration [37,38].

2) Extrinsic Camera Parameter

Extrinsic camera parameters [35] describe the coordinate transformation between the camera frame C and the world frame W, in which

$${}^{C}P = {}^{C}R_{W}\,{}^{W}P + {}^{C}t_{W} \tag{4}$$

where ${}^{C}t_{W} \in \Re^{3\times 1}$ is the translation vector between the origin ${}^{C}O$ of the camera frame and the origin ${}^{W}O$ of the world frame; ${}^{C}R_{W} \in \Re^{3\times 3}$ is the rotation matrix between the world frame and the camera frame. Rewriting Eq. (4) into the matrix form, one will have

$$\begin{bmatrix} {}^{C}P \\ 1 \end{bmatrix} = {}^{C}T_{W}\begin{bmatrix} {}^{W}P \\ 1 \end{bmatrix} = \begin{bmatrix} {}^{C}R_{W} & {}^{C}t_{W} \\ 0 & 1 \end{bmatrix}_{4\times 4}\begin{bmatrix} {}^{W}P \\ 1 \end{bmatrix} \tag{5}$$

By taking the intrinsic camera parameters and extrinsic camera parameters into account simultaneously, one can obtain the relationship between the coordinate of an object point in the world frame and the coordinate of its corresponding image point on the image plane, which is

$$p=\begin{bmatrix}u\\v\\1\end{bmatrix}=\frac{1}{{}^{C}Z}\begin{bmatrix}\lambda_x & \delta & u_0 & 0\\ 0 & \lambda_y & v_0 & 0\\ 0 & 0 & 1 & 0\end{bmatrix}\begin{bmatrix}{}^{C}R_W & {}^{C}t_W\\ 0 & 1\end{bmatrix}_{4\times4}\begin{bmatrix}{}^{W}X\\ {}^{W}Y\\ {}^{W}Z\\ 1\end{bmatrix} \quad (6)$$

B. Hand-eye Calibration

The online calibration method proposed in [39] is used to perform hand-eye calibration in this paper, in which a stereo camera is used to retrieve the 3D coordinates of a scene point in the camera frame. Its calibration process is elaborated in the following.

Consider a set of 3-D data points that contains *n* data points, in which these *n* 3-D data points have different coordinates in frame A and frame B. Suppose that Dataset *A* consists of the coordinates of these *n* 3-D data points in frame *A* and Dataset *B* consists of the coordinates of these *n* 3-D data points in frame *B*. Note that in this paper, frame *A* is the camera frame, while frame *B* is the robot base frame. Hand-eye calibration (i.e. coordinate transformation) that describes the relationship between Dataset *A* and Dataset *B* is performed to find the rotation matrix *R* and the translation vector *t* in Eq. (7). There are several existing approaches that can be used to calculate the rotation matrix *R* in Eq. (7). In this paper, the singular value decomposition method [40] is adopted.

$$P_B^i = RP_A^i + t \quad , \quad i=1,2,...,n, \ (n\geq 3) \quad (7)$$

Firstly, Eq. (8) and Eq. (9) are used to find the centers of Dataset *A* and Dataset *B*, respectively.

$$C_A=\frac{1}{n}\sum_{i=1}^{n}P_A^i \quad (8)$$

$$C_B=\frac{1}{n}\sum_{i=1}^{n}P_B^i \quad (9)$$

Define the matrix *M* as

$$M=\sum_{i=1}^{n}(P_A^i-C_A)(P_B^i-C_B)^T \quad (10)$$

Denote *svd*(*M*)=(*U*,*S*,*V*) as the results of performing singular value decomposition of the matrix *M*. The rotation matrix *R* can then be found using Eq. (11).

$$R=Udiag(1,1,\det(UV^T))V^T \quad (11)$$

Once the rotation matrix *R* is found, the translation vector *t* can be calculated using Eq. (12).

$$t=P_B-RP_A \quad (12)$$

III. Classical Visual Servoing Structures

Fig. 2 shows the control block diagram of a typical visual servoing system. In Fig. 2, f is the feature vector of appropriate dimensions, f_d is the desired feature vector, and $e=f-f_d$ is the feature error vector. In addition, L_e is the interaction matrix, and L_e^+ is the pseudo inverse matrix of L_e; ${}^{C}V$ is the velocity screw of the end-effector in the camera frame; ${}^{B}V$ is the velocity screw of the end-effector in the robot frame; and $\dot{q}_d$ is the velocity command in the joint space.

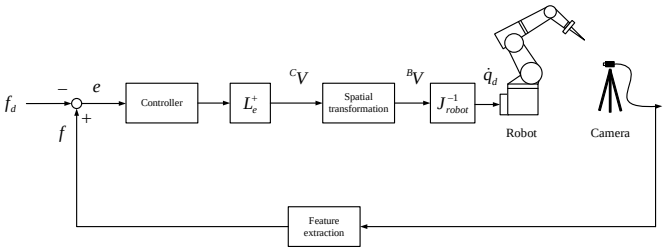

Figure 2. Control block diagram of a typical visual servoing system.

The eye-to-hand camera configuration is adopted in this paper [1]. Based on the type of feature, classical visual servoing structures can be divided into two categories –PBVS and IBVS. If a 3D point feature or a 6D pose is used, the visual servoing structure is PBVS. In general, PBVS usually yields a good 3D tracking performance. However, the drawback of PBVS is that its performance is sensitive to calibration error and modeling uncertainty. In contrast, if a 2D image feature is used, the visual servoing structure is IBVS. In general, IBVS results in satisfactory image tracking performance and is more robust to calibration error and modeling uncertainty than PBVS. However, the 3D tracking performance of IBVS could be far from satisfactory. Moreover, the convergence of image feature error does not guarantee the convergence of 3D tracking error.

A. Classical Image-based Visual Servoing

Suppose the IBVS structure is adopted and we define image feature point $f=[u,v]^T$, desired image feature point $f_d=[u_d,\ v_d]^T$, and feature error $e=f-f_d$. The relationship between the time derivative of the image feature point and the velocity screw of the end-effector in the camera frame is described by

$$\dot{f}=L_e\,{}^{C}V \quad (13)$$

where L_e is the so-called image Jacobian matrix; ${}^{C}V$ is the velocity screw of the end-effector in the camera frame.

If the goal is to exponentially converge the image feature error, then a proportional type controller can be used, namely

$$\dot{e}=-ke \quad , \quad k>0 \quad (14)$$

Suppose that the desired image feature is constant, that is $\dot{f}_d=0$. From Eq. (13), one will have

$$\dot{e}=\dot{f}-\dot{f}_d=\dot{f}=L_e\,{}^{C}V \quad (15)$$

By combining Eq. (14) and Eq. (15), the velocity screw of the end-effector in the camera frame can be calculated using

$${}^{C}V=-kL_e^+e \quad (16)$$

B. Image Jacobian Matrix

The derivation of the image Jacobian matrix will be detailed in this subsection. Given a 3D feature point ${}^{c}P=[{}^{c}X,\ {}^{c}Y,\ {}^{c}Z]^T$ in the camera frame and its corresponding image feature point $f=[u,v]^T$ in the image plane; in addition

to assuming that the camera has zero skew, i.e. δ=0, as a result, Eq. (3) can be rewritten as

$$f=\begin{bmatrix}u\\v\end{bmatrix}=\begin{bmatrix}\lambda_x\dfrac{{}^{C}X}{{}^{C}Z}+u_0\\ \lambda_y\dfrac{{}^{C}Y}{{}^{C}Z}+v_0\end{bmatrix} \tag{17}$$

Differentiating Eq. (17) with respect to time will yield

$$\dot{f}=\begin{bmatrix}\dot{u}\\\dot{v}\end{bmatrix}=\begin{bmatrix}\lambda_x\dfrac{{}^{C}Z\,{}^{C}\dot{X}-{}^{C}X\,{}^{C}\dot{Z}}{{}^{C}Z^2}\\ \lambda_y\dfrac{{}^{C}Z\,{}^{C}\dot{Y}-{}^{C}Y\,{}^{C}\dot{Z}}{{}^{C}Z^2}\end{bmatrix} \tag{18}$$

Suppose that this 3D point undergoes a rigid body motion. We will have

$${}^{C}\dot{P}={}^{C}\upsilon+{}^{C}\omega\times{}^{C}P \tag{19}$$

where ${}^{c}\upsilon=\begin{bmatrix}{}^{C}\upsilon_x & {}^{C}\upsilon_y & {}^{C}\upsilon_z\end{bmatrix}^T$ and ${}^{c}\omega=\begin{bmatrix}{}^{C}\omega_x & {}^{C}\omega_y & {}^{C}\omega_z\end{bmatrix}^T$.

Developing Eq. (19) will yield

$$\begin{bmatrix}{}^{C}\dot{X}\\{}^{C}\dot{Y}\\{}^{C}\dot{Z}\end{bmatrix}=\begin{bmatrix}{}^{C}\upsilon_x-{}^{C}Y\,{}^{C}\omega_z+{}^{C}Z\,{}^{C}\omega_y\\ {}^{C}\upsilon_y-{}^{C}Z\,{}^{C}\omega_x+{}^{C}X\,{}^{C}\omega_z\\ {}^{C}\upsilon_z-{}^{C}X\,{}^{C}\omega_y+{}^{C}Y\,{}^{C}\omega_x\end{bmatrix} \tag{20}$$

Substituting Eq. (20) into Eq. (18) and rearranging the terms will result in

$$\begin{bmatrix}\dot{u}\\\dot{v}\end{bmatrix}=\begin{bmatrix}\dfrac{\lambda_x}{{}^{C}Z} & 0\\ 0 & \dfrac{\lambda_y}{{}^{C}Z}\\ -\dfrac{(u-u_0)}{{}^{C}Z} & -\dfrac{(v-v_0)}{{}^{C}Z}\\ -\dfrac{(u-u_0)(v-v_0)}{\lambda_y} & -\dfrac{\lambda_y{}^2+(v-v_0)^2}{\lambda_y}\\ \dfrac{\lambda_x{}^2+(u-u_0)^2}{\lambda_x} & \dfrac{(u-u_0)(v-v_0)}{\lambda_x}\\ -\dfrac{\lambda_x(v-v_0)}{\lambda_y} & \dfrac{\lambda_y(u-u_0)}{\lambda_x}\end{bmatrix}^T\begin{bmatrix}{}^{C}\upsilon_x\\{}^{C}\upsilon_y\\{}^{C}\upsilon_z\\{}^{C}\omega_x\\{}^{C}\omega_y\\{}^{C}\omega_z\end{bmatrix} \tag{21}$$

Eq. (21) can be further expressed as

$$\dot{f}=L_e\,{}^{C}V \tag{22}$$

where L_e is the so-called image Jacobian matrix; ${}^{C}V$ is the velocity screw of the end-effector in the camera frame, which is a 6×1 vector consisting of translation velocity ${}^{C}\upsilon$ and rotational velocity ${}^{C}\omega$.

IV. 6-Dimensional Visual Servoing

Similar to the 2 1/2D visual servoing structure [7], the 6D visual servoing structure [14] employed in this paper also tries to balance the advantages and drawbacks of the IBVS structure and the PBVS structure. In fact, experimental results provided in [14] suggest that the 6D visual servoing structure performs better than the 2 1/2D visual servoing structure. Moreover, the 6D visual servoing (6DVS) structure overcomes two notorious drawbacks of the IBVS structure. The 6DVS structure is elaborated as follows.

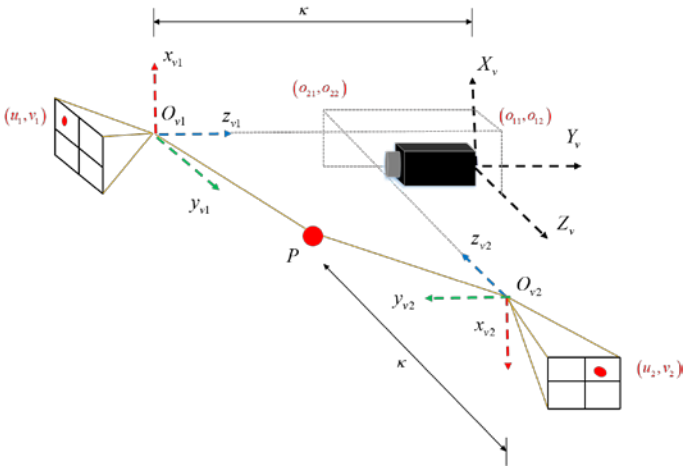

Figure 3. Orthogonal image feature.

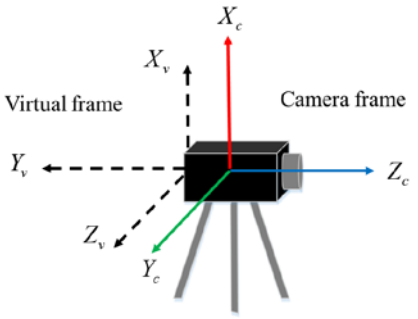

Figure 4. Relationship between the virtual frame *V* and the camera frame *C*.

In order to obtain an interaction matrix with superior characteristics and convergence trajectory, the 6DVS structure selects features as below [14]:

$$W_s=\begin{bmatrix}X_s & \theta_s\end{bmatrix}=\begin{bmatrix}x_s & y_s & z_s & \alpha & \beta & \gamma\end{bmatrix}\in\Re^{6\times1} \tag{23}$$

where x_s, y_s, and z_s shown in Fig. 3 are the orthogonal image features defined in a virtual frame used to control the linear speed; α,β and γ are the rotation angles expressed in the form of Euler angle [41].

The six features x_s, y_s, z_s, α, β and γ are designed as follows. First, we introduce the feature design method for controlling linear speed. We define two virtual image planes and project a point in space onto these two planes as shown in Fig. 3. In Fig. 3, the virtual frame *V* is a user-defined coordinate system. As indicated in Fig. 4, the virtual frame *V* and the camera frame *C* have the same origin, but with different axis directions as described by Eq. (24).

$$\begin{bmatrix}x_v\\y_v\\z_v\end{bmatrix}={}^{V}R_C\begin{bmatrix}x_c\\y_c\\z_c\end{bmatrix}=\begin{bmatrix}1&0&0\\0&0&-1\\0&1&0\end{bmatrix}\begin{bmatrix}x_c\\y_c\\z_c\end{bmatrix} \tag{24}$$

Suppose that there are two virtual cameras denoted as V_{c1} and V_{c2}. Let the optical axes for the frames affixed to these two cameras be perpendicular to each other as shown in Fig. 3. Suppose that both the distance between the O_{v1} point to the x_v axis and the distance between the point O_{v2} to the z_{v1} axis are κ. Consider a 3-D feature point P. Based on perspective projection, one can obtain the corresponding image point (u_1,v_1) on the virtual image plane of V_{c1} as described by Eq. (25) and the corresponding image point (u_2,v_2) on the virtual image plane of V_{c2} as described by Eq. (26).

$$\begin{bmatrix} u_1 \\ v_1 \end{bmatrix} = \frac{1}{-y_v + \kappa} \begin{bmatrix} f_\beta & 0 \\ 0 & f_\beta \end{bmatrix} R(\phi) \begin{bmatrix} x_v - o_{11} \\ z_v - o_{12} \end{bmatrix} + \begin{bmatrix} c_x \\ c_y \end{bmatrix} \tag{25}$$

$$\begin{bmatrix} u_2 \\ v_2 \end{bmatrix} = \frac{1}{x_v + \kappa} \begin{bmatrix} f_\beta & 0 \\ 0 & f_\beta \end{bmatrix} R(\phi) \begin{bmatrix} y_v - o_{21} \\ z_v - o_{22} \end{bmatrix} + \begin{bmatrix} c_x \\ c_y \end{bmatrix} \tag{26}$$

where f_β , ϕ, C_x and C_y are virtual intrinsic camera parameters defined by users.

The three features used to control the linear velocity are defined as u_1, u_2 and v_2. Now select u_1, u_2 and v_2 described by Eqs. (25)-(26) as the virtual image feature X_s. In addition, from Fig. 3, one can find that u_1, u_2 and v_2 constitute 3-D image coordinates and they are perpendicular to each other. The projection relationship can be expressed as Eq. (27).

$$X_s = \begin{bmatrix} u_1 \\ u_2 \\ v_2 \end{bmatrix} = \overbrace{\begin{bmatrix} \frac{f_\beta}{\cos\phi} & 0 & 0 \\ 0 & f_\beta \cos\phi & -f_\beta \sin\phi \\ 0 & f_\beta \sin\phi & f_\beta \cos\phi \end{bmatrix}}^{R_\alpha} \begin{bmatrix} \frac{x_v - o_{11}}{-y_v + \kappa} \\ \frac{y_v - o_{21}}{x_v + \kappa} \\ \frac{z_v - o_{22}}{x_v + \kappa} \end{bmatrix} + \begin{bmatrix} c_x + c_y \tan\phi - v_1 \tan\phi \\ c_x \\ c_y \end{bmatrix} \tag{27}$$

Differentiating X_s described by Eq. (27) with respect to time will yield

$$\dot{X}_s = R_\alpha J_o {}^V\dot{X} = J_\alpha {}^V\dot{X} \tag{28}$$

where

$$J_o = \begin{bmatrix} \frac{1}{-y_v + \kappa} & -\frac{x_v - o_{11}}{(-y_v + \kappa)^2} & 0 \\ -\frac{y_v - o_{21}}{(x_v + \kappa)^2} & \frac{1}{x_v + \kappa} & 0 \\ -\frac{z_v - o_{22}}{(x_v + \kappa)^2} & 0 & \frac{1}{x_v + \kappa} \end{bmatrix} \tag{29}$$

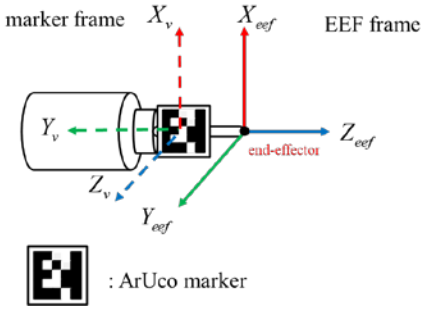

Figure 5. Rigid transformation between the end-effector frame and the marker frame.

The coordination transformation between the virtual frame V and the robot base frame B is described by

$${}^V X = {}^V R_C {}^C X = {}^V R_C ({}^C R_B {}^B X + {}^B t_C) \tag{30}$$

Substituting the time derivative of ${}^V X$ into Eq. (28) will yield

$$\dot{X}_s = J_\alpha ({}^V R_C {}^C R_B) {}^B\dot{X} = J_v {}^B\dot{X} = J_v {}^B v \tag{31}$$

Eq. (31) describes the relationship between $\dot{X}_s$ and the linear velocity of the robot base frame.

Denote ${}^B R_{EEF}$ as the pose of the end-effector in the robot base frame. The three features used to control the angular velocity are defined as $\theta = [\alpha, \beta, \gamma]$ (expressed in the form of Euler angle). In this paper, ${}^B R_{EEF}$ can be calculated using

$${}^B R_{EEF} = {}^B R_W {}^W R_{EEF} \tag{32}$$

where ${}^B R_W = {}^B R_C {}^C R_W$; W is the marker frame (in this paper, an ArUco marker is used in the hand-eye calibration process); ${}^B R_C$ represents the hand-eye calibration; ${}^C R_W$ is the rigid transformation (i.e. pose) between the marker frame and the camera frame, which can be estimated; and ${}^W R_{EEF}$ is the rigid transformation (i.e. pose) between the end-effector frame and the marker frame as shown in Fig. 5.

From Fig. 5, it is easy to conclude

$${}^W R_{EEF} = \begin{bmatrix} 1 & 0 & 0 \\ 0 & 0 & -1 \\ 0 & 1 & 0 \end{bmatrix} \tag{33}$$

The relationship between the angular velocity ${}^B\omega$ and $\dot{\theta}$ is described by [41]

$${}^B\omega = T(\theta)\dot{\theta} \tag{34}$$

where

$$T(\theta) = \begin{bmatrix} \cos\gamma\cos\beta & -\sin\gamma & 0 \\ \sin\gamma\cos\beta & \cos\gamma & 0 \\ -\sin\beta & 0 & 1 \end{bmatrix} \tag{35}$$

Therefore

$$\dot{\theta} = T^{-1}(\theta) {}^B\omega = J_\omega \cdot {}^B\omega \tag{36}$$

By combining Eq. (31) and Eq. (36), the complete interaction matrix (i.e. image Jacobian matrix) that describes the relationship between the optical flow and the spatial end-effector velocity (an ArUco marker is attached to the end-effector of the 6-DOF industrial robot manipulator) in the robot base frame can be obtained.

$$\dot{W}_s = \begin{bmatrix} \dot{X}_s \\ \dot{\theta} \end{bmatrix} = \begin{bmatrix} J_v & 0 \\ 0 & J_\omega \end{bmatrix} \begin{bmatrix} {}^B v \\ {}^B \omega \end{bmatrix} = J_{img} \cdot {}^B V \tag{37}$$

where J_{img} is the interaction matrix (i.e. image Jacobian matrix) and ${}^B V$ is the spatial end-effector velocity in the robot base frame.

Eq. (37) indicates that, by choosing x_s, y_s, z_s, α, β and γ as features, the control of translational motion and the control of rotational motion are decoupled. This is an attractive feature that IBVS does not have.

In the IBVS structure, the image Jacobian matrix may encounter the singular point problem. Since $J_{img} = \begin{bmatrix} J_v & 0 \\ 0 & J_\omega \end{bmatrix}$ in Eq. (37), one will have $\det(J_{img}) = \det(J_v)\det(J_\omega)$. Whether J_{img} is invertible or not depends on J_v and J_ω. If the robot pose can avoid the singular point (i.e. $\det(T(\theta)) \neq 0$), then J_ω is invertible.

As for the case of J_v, from Eq. (31), one will have

$$J_v^{-1} = {}^C R_B^{-1} {}^V R_C^{-1} J_o^{-1} R_\alpha^{-1} \tag{38}$$

Since ${}^C R_B$, ${}^V R_C \in SO(3)$ and $R_\alpha = diag(f_\beta) \in \Re^{3\times 3}$, they are invertible. Only when $\det(J_o) = 0$, J_v will become singular. In fact, only the following three cases will result in a singular J_v.

Case 1: $o_{11} + \kappa = 0$ and $o_{21} - \kappa = 0$

Case 2: $x_v = -\kappa$ and $y_v = o_{21}$

Case 3: $y_v = \kappa$ and $x_v = o_{11}$

As mentioned previously, the values of o_{11}, o_{21} and κ are chosen by the user. Therefore, by properly selecting the values of o_{11}, o_{21} and κ, one can ensure that the image Jacobian matrix J_{img} is invertible.

V. Experimental Results

A. Experimental Setup

Fig. 6 shows the experimental platform used in this paper to access the performance of the conventional IBVS structure and the 6DVS structure. The experimental platform consists of a 6-DOF industrial robot manipulator (Fig. 6(a)) manufactured by ITRI, a stereo camera (Fig. 6(b)) manufactured by Point Grey (type GS3-U3-23S6C-C) which is equipped with a lens by VS Technology (type SV-0614V), and a PC (Intel Core™ i7-2600, 3.40 GHz CPU; 4.0GB RAM) used as a control kernel which is responsible for executing visual servoing structures. In this paper, when performing hand-eye calibration, an ArUco marker [42] attached to the end-effector as shown in Fig. 6 (a) is adopted as a calibration rig.

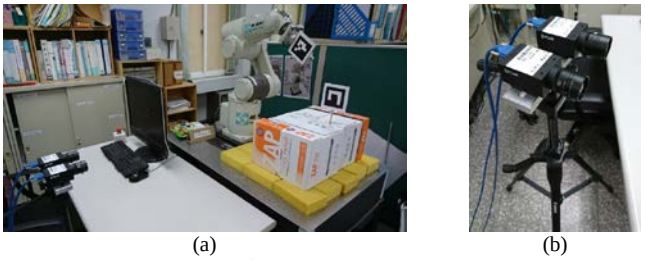

(a) (b)

Figure 6. Experimental platform (a). 6-DOF industrial robot manipulator (b). stereo camera.

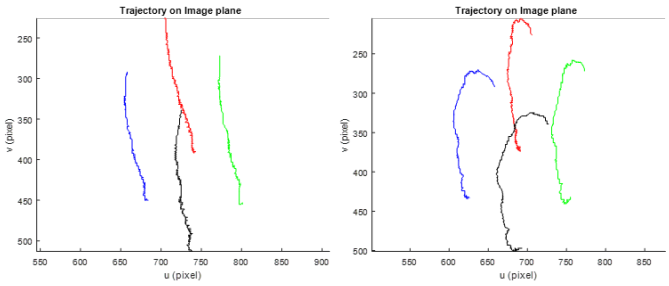

(a) (b)

Figure 7. Convergence trajectory on image plane: (a) 6DVS, (b) classical IBVS.

B. Experimental results

Experimental results are detailed in this subsection. In the experiment, a 6-DOF industrial robot manipulator is controlled to perform a point-to-point motion. Both the classical IBVS structure and the 6DVS structure will be tested in the experiment. Throughout the experiment, the PI-type feedback controller with gravity compensation is selected as the velocity loop controller of the 6-DOF robot manipulator. The initial image feature and the target image feature are the same for both the classical IBVS structure and the 6DVS structure. In the user-defined parameters of the 6DVS structure, for ease of calculation, ϕ, o_{11}, o_{12}, o_{21}, o_{22}, c_x and c_y are all set to zero. The focus length f_β is set to $f_\beta = (f_x + f_y)/2$; the depth κ is set to 1500 mm.

According to the experimental results shown in Fig.7, it is easy to find that the convergence trajectory for the 6DVS structure in both the Cartesian space and the image plane is close to a straight line, which is ideal and efficient compared to the convergence trajectory of the classical IBVS structure. In addition, in the convergence of the feature error, since the 6DVS structure decouples the translation feature and the rotation feature, the translational motion and the rotational motion do not affect each other and can directly converge. In contrast, the classical IBVS structure may affect the translational motion when the robot manipulator changes its pose, causing the feature error to rise and then fall. Moreover, as shown in Fig. 8(c), if the difference between the initial feature and the target feature is too large, the visual servoing system that employs the classical IBVS structure may diverge directly. In contrast, the visual servoing system that employs the 6DVS structure may still converge (Fig. 8(a) and Fig. 8(b)).

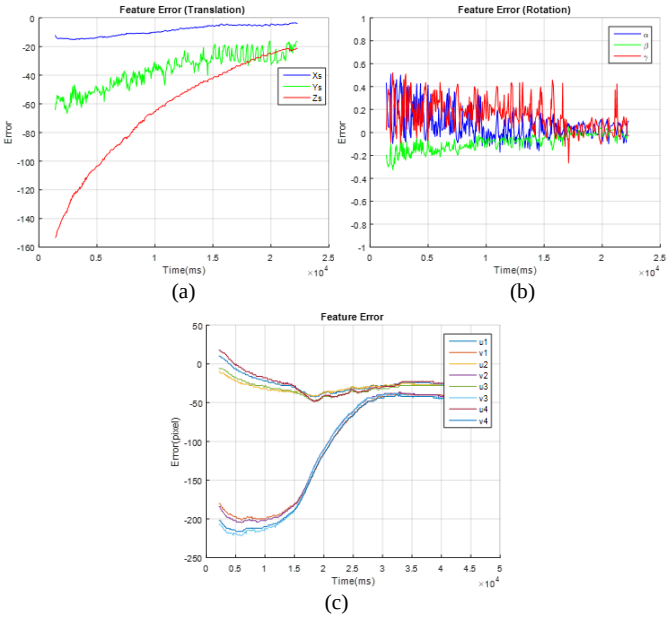

Figure 8. Feature error convergence: (a) feature error on translation axis for 6DVS (b) feature error on rotation axis for 6DVS (c) feature error for classical IBVS.

VI. Conclusion

Among the many approaches proposed to alleviate the drawbacks of the classical IBVS structure, the 6DVS structure has been reported to exhibit satisfactory performance. In this paper, a detailed description about the crucial processes needed in implementing the 6DVS structure including camera calibration, hand-eye calibration and derivation of the interaction matrix, is provided. A 6-DOF industrial robot manipulator is used as a test platform to compare the performance of 6DVS and classical IBVS. Experimental results indicate that the 6DVS structure indeed exhibits better convergence performance than the classical IBVS structure.

VII. Acknowledgments

The authors would like to thank the Ministry of Science and Technology, Taiwan, for support of this research under Grant No. MOST 105-2221-E-006-105-MY3.

References

[1] J. Hill and W. T. Park, "Real time control of a robot with a mobile camera," in *Proc. 9th ISIR*, Washington, U.S.A., Mar. 1979, pp. 233 -246.

[2] S. Hutchinson, G. D. Hager, and P. I. Corke, "A tutorial on visual servo control," *IEEE Trans. on Robotics and Automation*, vol. 12, pp. 651-670, Oct. 1996.

[3] A. C. Sanderson and L. E. Weiss. *Adaptive visual servo control of robots*. In A. Pugh, editor, Robot Vision, pp. 107-116. IFS, 1983.

[4] W. J. Wilson, C. C. Williams Hulls, and G. S. Bell, "Relative end-effector control using Cartesian position based visual servoing," *IEEE Trans. on Robotics and Automation*, vol.12, pp.684-696, Oct. 1996.

[5] E.-C. Tseng, M.-Y. Cheng, and M.-C. Tsai, "Design of a PI-type torque observer for detecting abnormal load," in *Proc. 1998 International Conf. Mechatronics Technology*, 1998, pp. 147–152.

[6] F. Chaumette and S. Hutchinson, "Visual servo control part I: basic approaches," *IEEE Robotics & Automation Magazine*, vol.13, Dec. 2006.

[7] E. Malis, F. Chaumette, and S. Boudet, "2½D visual servoing," *IEEE Trans. on Robotics and Automation*, vol. 15, pp. 238-250, Apr. 1999.

[8] E. Malis and F. Chaumette, "2 1/2 D visual servoing with respect to unknown objects through a new estimation scheme of camera displacement," *International Journal of Computer Vision*, vol. 37, pp.79-97, Jun 2000.

[9] P. I. Croke and S. A. Hutchinson, "A new hybrid image-based visual servo control scheme," in *Proc. IEEE Conf. Decision and Control*, Sydney, NSW, pp.2521-2526. Dec. 2000.

[10] N. Gans and S. Hutchinson, "An asymptotically stable switched system visual controller for eye in hand robots," in *Proc. IEEE/RSJ Int. Conf. Intelligent Robots Systems*, Las Vegas, NV, pp. 735–742. Oct. 2003.

[11] F. Chaumette and S. Hutchinson, "Visual Servo Control, Part II：Advanced Approaches," *IEEE Robotics and Automation Magazine*, vol.14, pp.109-118, Mar 2007.

[12] O. Tahri and F. Chaumette, "Point-based and region-based image moments for visual servoing of planar objects," *IEEE Trans. on Robotics*, vol.21, pp.1116-1127. Dec. 2005.

[13] D. Xu, J. Lu, P. Wang, Z. Zhang and Z. Liang, "Partially decoupled image-based visual servoing using different sensitive features," *IEEE Trans. on Systems, Man, and Cybernetics：Systems*, vol.47, pp.2233-2243. Jan. 2017.

[14] C. Cai, N. Somani, and A. Knoll, "Orthogonal image features for visual servoing of a 6-DOF manipulator with uncalibrated stereo cameras," *IEEE Trans. on Robotics*, vol. 32, pp.452-461, Apr. 2016.

[15] R. Dahmouche, N. Andreff, Y. Mezouar, O. Ait-Aider and P. Martinet, "Dynamic visual servoing from sequential regions of interest acquisition," *The International Journal of Robotics Research*, vol.31, pp.520-537. Feb. 2012.

[16] M. Keshmiri, W. F. Xie and A. Mohebbi, "Augmented image-based visual servoing of a manipulator using acceleration command," *IEEE Trans. on Industrial Electronics*, vol.61, pp.5444-5452. Oct. 2014.

[17] F. Chaumette, S. Boukir, P. Bouthemy and D. Juvin, "Structure from controlled motion," *IEEE Trans. on Pattern Analysis and Machine Intelligence*, vol. 18, no. 5, pp. 492–504, 1996.

[18] A. De Luca, G. Oriolo, and P. R. Giordano, "Feature depth observation for image-based visual servoing：Theory and experiments," *Int. J. Robot. Res.*, vol. 27, no. 10, pp. 1093–1116, 2008.

[19] G. Chesi and Y. S. Hung, "Global path-planning for constrained and optimal visual servoing," *IEEE Trans. on Robotics*, vol.23, pp.1050-1060. Oct. 2007.

[20] M. Keshmiri and W. F. Xie, "Image-based visual servoing using an optimized trajectory planning technique," *IEEE/ASME Trans. on Mechatronics*, vol.22, pp.359-370. Aug. 2016.

[21] P. I. Corke and M. C. Good, "Dynamic effects in visual closed-loop systems," *IEEE Trans. on Robotics and Automation*, vol. 12, pp.671-683. Oct. 1996.

[22] P. J. Sequeira Goncalves, L. F. Mendonca, J. M. C. Sousa and J. R. Caldas Pinto, "Uncalibrated eye-to-hand visual servoing using inverse fuzzy models," *IEEE Trans. on Fuzzy Systems*, vol.16, pp.341-353. Apr. 2008.

[23] I. Siradjuddin, L. Behera, T. Martin McGinnity and S. Coleman, "Image-based visual servoing of a 7-DOF robot manipulator using an adaptive distributed fuzzy PD controller," *IEEE/ASME Trans. on Mechatronics*, vol.19, pp.512-523. Apr. 2014.

[24] T. Yüksel, "Intelligent visual servoing with extreme learning machine and fuzzy logic," *Expert Systems With Applications*, vol.72, pp.344-356. Apr. 2017.

[25] P. Jiang, Leon C. A. Bamforth, Z. Feng, John E. F. Baruch and Y. Q. Chen, "Indirect iterative learning control for a discrete visual servo without a camera-robot model," *IEEE Trans. on Systems, Man, and Cybernetics, Part B (Cybernetics)*, vol.37, pp.863-876. Aug. 2007.

[26] P. Jiang and R. Unbehauen, "Robot visual servoing with iterative learning control," *IEEE Trans. on Systems, Man, and Cybernetics - Part A：Systems and Humans*, vol.32, pp.281-287. Mar. 2002.

[27] Y. Wang, H. Lang and C. W. de Silva, "A hybrid visual servo controller for robust grasping by wheeled mobile robots," *IEEE/ASME Trans. on Mechatronics*, vol.15, pp.757-769. Oct. 2010.

[28] H. Shi, X. Li, K. S. Hwang, W. Pan and G. Xu, "Decoupled visual servoing with fuzzy Q-learning," *IEEE Trans. on Industrial Informatics*, vol.14, pp.241-252. Jan. 2018.

[29] Yen-Jyun Lai, Ming-Yang Cheng, "Q-learning based IBVS for a Mobile Robot Equipped with a 5-axis Manipulator" in *Proc. of the ARIS2018*.

[30] T. Yuksel, "IBVS with fuzzy sliding mode for robot manipulators," in *Proc. Int. Workshop Recent Advances in Sliding Modes*, Istanbul, pp.1-6. 2015.

[31] Che-Liang Li, Ming-Yang Cheng, Wei-Che Chang, "Dynamic Performance Improvement of Direct Image Based Visual Servoing in Contour Following," *International Journal of Advanced Robotic Systems*, January-February 2018: 1–12.

[32] Janabi-Sharifi, Farrokh, and Mohammed Marey. "A Kalman-filter-based method for pose estimation in visual servoing," *IEEE Trans. on Robotics*, vol.26, pp.939-947, Oct. 2010.
[33] C. Wang, C. Y. Lin, and M. Tomizuka. "Statistical learning algorithms to compensate slow visual feedback for industrial robots," *Journal of Dynamic Systems, Measurement, and Control*, vol.137 Mar. 2015.
[34] M. Marshall and H. Lipkin, "Adaptive Kalman filter control law for visual servoing," in *Proc. International Conf. Collaboration Technologies and Systems (CTS)*, Orlando, FL, USA, 2016.
[35] D. A. Forsyth and J. Ponce, *Computer Vision, A Modern Approach*, Prentice Hall, New Jersey, 2003.
[36] R. Hartley and A. Zisserman, *Multiple View Geometry in Computer Vision, 2nd ed.*, New York, NY：Cambridge Univ. Press, 2004.
[37] R. Tsai, "A versatile camera calibration technique for high-accuracy 3D machine vision metrology using off-the-shelf TV cameras and lenses," *IEEE Journal on Robotics and Automation*, vol.3, pp.323-344, Aug. 1987.
[38] Z. Zhang, "A flexible new technique for camera calibration," *IEEE Trans. on pattern analysis and machine intelligence*, vol.22, pp.1330-1334, Nov. 2000.
[39] C. Cai, N. Somani, S. Nair, D. Mendoza, and A. Knoll, "Uncalibrated stereo visual servoing for manipulators using virtual impedance control," in *Proc. 13th International Conf. Control Automation Robotics & Vision*, Singapore, Dec. 2014, pp. 1888-1893.
[40] D. G. Lay, *Linear Algebra and Its Applications*, 2nd edition, 1996, Addison-Wesley.
[41] M. W. Spong, S. Hutchinson, and M. Vidyasagar, *Robot Dynamics and Control*, 2nd ed. New York, USA: John Wiley & Sons, 2004.
[42] Open Source Computer Vision. Detection of ArUco Markers. Retrieved Aug. 20, 2018, from https：//docs.opencv.org/3.1.0/d5/dae/tutorial_aruco_detection.html

Ting-Yu Chang was born in Taiwan, 1994. In 2015, he received his B.S. in Electrical Engineering from the National Cheng Kung University, Taiwan. In 2017, he received his M.S. in Electrical Engineering from the National Cheng Kung University, Taiwan. His research interests include robot control and computer vision.

Wei-Che Chang was born in Taiwan, 1988. He received the B.S. degree in Systems and Mechatronic Engineering from the National Cheng Kung University, Taiwan, in 2011. He received the M.S. degree in Electrical Engineering from the National Cheng Kung University, Taiwan, in 2013. He is currently woring toward the Ph.D. degree in Electrical Engineering at National Cheng Kung University, Taiwan. His research interests include robot control and visual servoing.

Ming-Yang Cheng received the B.S. degree in Control Engineering from National Chiao Tung University, Hsinchu, Taiwan, in 1986, and M.S. and Ph.D. degrees in Electrical Engineering from the University of Missouri, Columbia, in 1991 and 1996, respectively. From 1997 to 2002, he held several teaching positions at Kao Yuan Institute of Technology, Kaohsiung, Taiwan; Dayeh University, Changhua, Taiwan; and National Kaohsiung First University of Science and Technology, Kaohsiung, Taiwan. Since 2002, he has been with the Department of Electrical Engineering, National Cheng Kung University, Tainan, Taiwan, where he is currently a Professor. His research interests include motion control, motor drives, visual servoing, and robot control.

Shih-Sian Yang was born in Taiwan, 1995. He received the B.S. degree in Electrical Engineering from the National Cheng Kung University, Taiwan, in 2018. He is currently working toward the M.S. degree in Electrical Engineering at National Cheng Kung University, Taiwan. His research interests include robot control and computer vision.

Goods Recognition Using Improved Tiny YOLOv3 for an Autonomous Quadrotor in an Indoor Warehouse Environment

Hsiu-Chen Tsai and Ching-Chih Tsai, *Fellow, RST*

***Abstract*—This paper aims to present an autonomous quadrotor system with an improved tiny YOLOv3 neural network for goods recognition in the indoor warehouse environment. The used autonomous quadrotor is equipped with a powerful computing module, NVIDIA Jetson TX2 board, one LiDAR (light detection and ranging), one ultrasonic ranging sensor, and two cameras. Such a quadrotor is exploited to fly in front of goods stored in their corresponding shelves and acquire their images. The Jetson TX2 computing module is used to deal with computational tasks including flight trajectory planning, goods recognition and wireless communication with an inventory management system. An improved tiny YOLOv3 neural network is proposed to process inventory goods images acquired from the quadrotor and recognize these goods from these images, in order to check and manage the goods status in the warehouse environment. Experimental results are conducted to show the effectiveness and merits of the improved tiny YOLOv3 neural network mounted on the autonomous quadrotor.**

***Index Terms*—Goods recognition, quadrotor, you look only once (YOLO), YOLOv3, warehouse management.**

I. Introduction

NOWADAYS, in order to attain cost reduction and automation requirement, material handling systems using mobile robots in inventory environments have become increasingly popular and important. With the rapid evolution and growth of deep learning, robot systems using deep learning have achieved a great success in the field of object and pattern recognition. Therefore, there have been many related investigations and public competitions using deep learning techniques; for example, Amazon's robotic competition was held for recognize many objects coming from their own warehouses. Besides, there are many studies presenting various methods to investigate the use of mobile robots in inventory, warehouse or supermarket environments. Zhang et al. [1] proposed a mobile robot, which was able to deal with one inventory task, in the indoor environment; their proposed system had an ability to build a costmap, which was an occupancy gird map, by using ultrasound, Lidar and RGB camera to sense and model the environment such that the used mobile robot was shown able to scan RFID tags for the inventory environment. However, this kind of robot was manually controlled without any navigation algorithm and automatic robot movement. Yabushita et al. [2] presented a new framework for recognizing three-dimensional (3D) objects that need few reference images, and dealt with a key issue of 3D object recognition by considering the trade-off between the number of reference images and recognition accuracy. Nevertheless, this method had poor resolutions for those objects with similar images, although their shapes are different.

Deep learning neural networks have been widely applied to recognize various objects with huge amount of images. For instance, Li at el. [3] applied the convolution neural network (CNN) on identification of supermarket goods. Different from the QR code identification of supermarket goods, they applied the CNN which used the collected images of commodity as the input. In particular, deep convolution neural networks (DCNNs) have been extensively used for image recognition and object understanding effectively and efficiently. Among DCNNs, YOLO, standing for You Only Look Once, in [4] has been shown as faster and more efficient neural networks, and has also been implemented into a mobile embedded system for real-time imaging applications. Being an object detector, YOLO uses features learned by a deep convolutional neural network to detect an object. YOLOv2 neural networks are an improved version of YOLO and their functions are more accurate than those of their original version [5]. However, YOLOv2 has been known difficult to identify for smaller objects and overlapping objects. YOLOv3 neural networks with the ResNet have been shown better performance and improvement in [6], but they need more training and execution time than YOLOv2 does. This motivates us to think how to modify YOLOv3 so as to obtain acceptable accuracy and speed of goods recognition in an embedded computing system installed on the autonomous quadrotor.

The objectives of the paper are to investigate how to modify the tiny YOLOv3 for goods recognition, and to use the autonomous quadrotor with the improved tiny YOLOv3 to recognize the commodity in an indoor warehouse. The presented techniques would provide useful references for professionals working for the use and control of UAVs.

The rest of the paper is organized as follows. Section II briefly describes the hardware and software system structure of the proposed goods recognition systems using the autonomous quadrotor, and Section III calibrates the indoor goods images acquired from the circular fisheye camera. In Section IV, the detection and recognition of the stored commodity in the warehouse are done by using an improved tiny YOLOv3 deep neural network. Section V presents and discusses the experimental results to show the effectiveness and applicability of the proposed method. Section VI concludes the paper.

Hsiu-Chen Tsai was with the Department of Electrical Engineering, National Chung Hsing University, Taichung 40227, Taiwan R.O.C. (e-mail: v1251774721@gmail.com).

Ching-Chih Tsai is with the Department of Electrical Engineering, National Chung Hsing University, Taichung 40227, Taiwan R.O.C. (corresponding author, e-mail: cctsai@nchu.edu.tw)

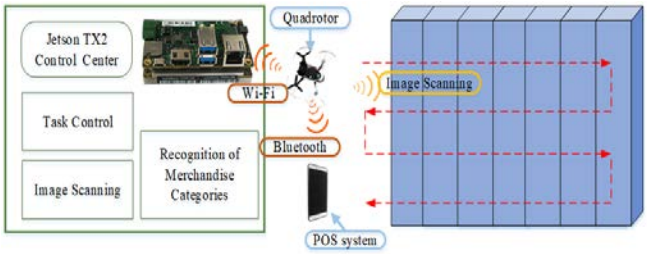

Figure 1. Illustration of the goods recognition system using the autonomous quadrotor with the Nvidia Jetson TX2 computing module.

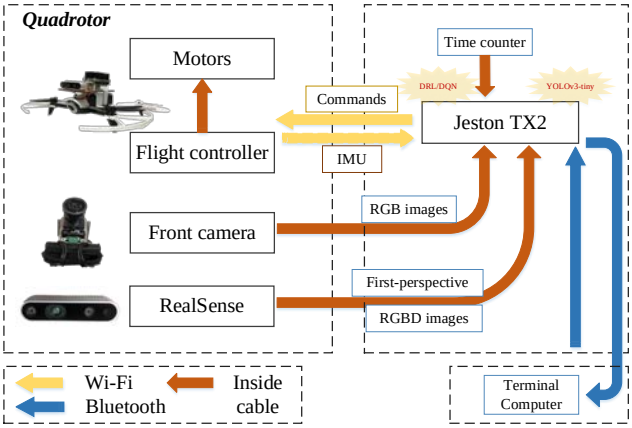

Figure 2. Control system structure of the autonomous quadrotor.

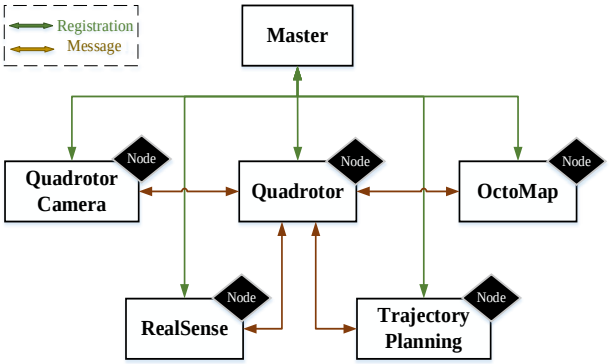

Figure 3. Overall software structure using ROS 1.0.

Figure 4. Control system structure of the autonomous quadrotor.

II. System Structure and Description

This section is aimed to describe the system structure of the proposed system by including the system configuration of the indoor quadrotor under the ROS environment. The ROS will be used as a software framework for the system, where each sensor or module will be registered as a node and communicate with each other via the master of the ROS. The autonomous driving of the quadrotor will be implemented in the ROS environment.

A. System Structure

Figs. 1 and 2 show the overview of the autonomous quadrotor system and the system structure in the indoor inventory. Such a quadrotor is responsible for capturing images in front of the shelf. Meanwhile, the quadrotor carries a powerful computing module, NVIDIA Jetson TX2, which is dedicated to execute all the computations, including flight trajectory calculation and specific goods recognition. Once the quadrotor has reached its destination, the quadrotor will use the tiny YOLOv3 neural network to detect the goods. After goods recognition, the TX2 computing module will send the results to the computer considered as the point of sale (POS) system by Bluetooth. Fig. 3 presents the overall system structure in the ROS environment. In Fig. 3, the quadrotor will be considered as a node, and it will publish its navigation data, the images of front and bottom cameras to other nodes of ROS. The LiDAR will be registered as another node, which will transmit the Lidar data to other nodes of ROS. Master manages that the nodes communication with each other. Once the camera images and LiDAR Data have been published to the Master of ROS successfully, the ORB-SLAM2 algorithm in [7] as a node will be able to subscribe these data and process the computations of the algorithm. Meanwhile, the trajectory planning module will also be registered as a node in order to command the quadrotor to the proper position by publishing control commands. Fig. 4 shows the goods recognition robot system, where the on-board Jetson TX2 and LiDAR which respectively have adequate perceptual and computing abilities are able to assist the quadrotor in indoor warehouse environments to proceed with the goods image scanning and identify task.

III. Acquisition and Calibration of Goods Images

This section presents how to handle with both acquisition and calibration tasks of goods images scanned by quadrotor by using fish-eye lens calibration technique and. In order to perform a proper indoor quadrotor flight, ORB-SLAM is deployed to localize and automatically build the environment of the quadrotor. Furthermore, to ensure the safety of the quadrotor while it flies close to the shelf, the LiDAR sensor will provide relevant distance information to the quadrotor. The SLAM technique guarantees the quadrotor to navigate itself safely in the warehouse environment, and ensures enough accuracy of the quadrotor to process the scanning task in the way of closing to the shelf. Once the quadrotor has flown in front of the shelf, the images of the goods will be captured simultaneously. Moreover, these images will be calibrated into accurate images in order to identify. Therefore, the modified tiny YOLOv3 neural network will be employed to recognize the goods.

A. Image Scanning via the Quadrotor

Due to the convenience of the fish-eye lenses used in such applications where a very wide angle of view is needed, the

Bebop2 quadrotor adopt the fish-eye lens as the lens of its front camera. However, the use of this type of lens for measurement purposes has been limited owing to lacking of an accurate, generic, and easy-to-use calibration procedure. This results in that the modified tiny YOLOv3 cannot identify the commodity via its acquired images or its recognition rate may be extremely low because of distorted images.

In order to solve the problem, we hence apply a simple method to allow the quadrotor catches the commodity images without blurring. During the quadrotor flying in front of the shelf, the image of the goods will be captured and these images will be calibrated into an restored image. Once these images are calibrated into accurate images, and the goods will be identified using modified tiny YOLOv3. Furthermore, the caught images about the shelf is also able to provide the inventory information to the inventory manager in order to proceed with process inventory management. The scanning task is designed in the following three steps:

Step 1: Navigate the quadrotor safely
The computing module TX2 which processes ORB-SLAM2 algorithm navigates the quadrotor to the shelf.

Step 2: Scan the goods' images via the flight sequence
The quadrotor will fly horizontally from one side of the shelf to another side. Afterwards, it will fly to the next flight height and repeat to fly from one side to another. During the flight sequence, the locations of scanned images can be recorded as well.

Step 3: Complete the image scanning task
Once the quadrotor has completed the scanning task, it will transmit the information to the computing module TX2 and recognize the goods.

B. Fish-Eye Lenses Calibration for Goods Detection

Due to significant images distortion, it would be hard to identify the goods through the images accurately. Therefore, it is necessary to calibrate the canned good images in order to identify and recognize the commodity. There are two major kinds of distortions: radial distortion and tangential distortion. Radial distortion causes straight lines to become curved, and causes the farther points from the center of the image to become larger. The effect of the radial distortion is described as follows:

$$x_{distorted} = x(1 + k_1 r^2 + k_2 r^4 + k_3 r^6) \quad (1)$$

$$y_{distorted} = y(1 + k_1 r^2 + k_2 r^4 + k_3 r^6) \quad (2)$$

Similarly, tangential distortion occurs because the lens of taken image is not aligned perfectly parallel to the imaging plane. The tangential distortion can be shown as below:

$$x_{distorted} = x + [2 p_1 xy + p_2 (r^2 + 2x^2)] \quad (3)$$

$$y_{distorted} = y + [p_1 (r^2 + 2y^2) + 2 p_2 xy] \quad (4)$$

To sum up, we need to accomplish the image calibration by finding the five parameters, known as distortion coefficients given by:

$$Distortion\ coefficients = (k_1\ k_2\ p_1\ p_2\ k_3) \quad (5)$$

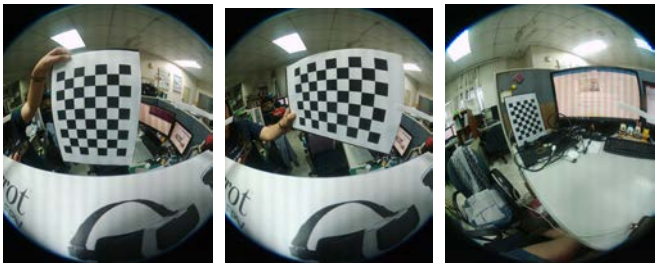

Figure 5. Some of raw fish-eye lens databases for calibration.

Aside from that, we need to some other information, like the intrinsic and extrinsic parameters of the camera. Intrinsic parameters are specific to a camera, and they include information like focal length (f_x, f_y) and optical centers (c_x, c_y). The focal length and optical centers can be used to create a camera matrix, which can be used to remove distortion due to the lenses of a specific camera. The camera matrix is unique to a specific camera, so once it has been calculated, it can be reused on other images taken by the same camera. The camera matrix is expressed by the following 3×3 matrix:

$$camera\ matrix = \begin{bmatrix} f_x & 0 & c_x \\ 0 & f_y & c_y \\ 0 & 0 & 1 \end{bmatrix} \quad (6)$$

Extrinsic parameters correspond to rotation and translation vectors which translates a coordinates of a 3D point to a coordinate system. Fig. 5 displays the three images from our "fish-eye lens" calibration process.

IV. Goods Recognition Using Modified Tiny YOLOv3 Neural Network

This section will investigate how to modify the YOLOv3 network architecture in order to recognize the goods in our own inventory environments more quickly, how to use the modified tiny YOLOv3 neural network for goods detection and recognition efficiently, and how to recognize the goods in a laboratory-built inventory environment more accurately through fine-tuning the pre-trained YOLOv3 weights. Owing to the small and complex images of the goods, traditional object detection may not recognize these goods successfully. To circumvent the difficulty, the YOLO (You Only Look Once) deep neural network, which is benefited from its robust, powerful and deep neural network, can be exploited to solve this problem. This modified YOLO neural network with the light-weight and real-time properties is particularly suitable to be implemented in this proposed embedded system to achieve good recognition. Hence, the tiny YOLOv3, which is the light-weight version of YOLO, will be implemented in the NVIDIA Jetson TX2 to achieve the real-time detection capability. Furthermore, the pre-trained weights of YOLOv3 will be fine-tuned with our own datasets in order to detect and classify the specific goods in the inventory environment.

A. Describing the YOLOv3 NN

The regular YOLOv3 makes use of only convolutional layers, making it a fully convolutional network (FCN). Being a FCN, YOLO is invariant to the size of the input image. It has 75 convolutional layers, with skip connections and upsampling layers. No form of pooling is used, and a convolutional layer with stride 2 is employed to downsample the feature maps. This

helps in preventing loss of low-level features often attributed to pooling. Typically, the features of the case for all object detectors learned by the convolutional layers are passed onto a classifier or regressor, which makes the detection prediction, such as coordinates of the bounding boxes (Bbox), the class label and etc. In the tiny YOLOv3, the prediction is done by using a convolutional layer, which uses convolutions.

The output of the network is a feature map, and the size of the prediction map is exactly the size of the feature map before it, due to the used of 1×1 convolutions. The prediction map is that each neuron can predict a fixed number of bounding boxes. The principle of the YOLO neural network is to divide the input image into a $S \times S$ gird, and have $(B \times (5+C))$ entries in the feature map. B represents the number of bounding boxes each neuron can predict. Each of these B bounding boxes may specialize in detecting a certain kind of object. Each of the bounding boxes have $5+C$ attributes, which describe the center coordinates, the dimensions, the objectiveness score and C class confidences for each bounding box. YOLO v3 predicts 3 bounding boxes for every neuron. If the center of the object falls in the receptive field of that neuron, each neuron of the feature map predicts an object through one of its Bboxes.

Once the box confidence box and conditional class probability have been estimated, the class confidence score for each predicted box will be computed as:

$$P_r(class_i) \cdot IoU = P_r(object) \cdot IoU \times P_r(class_i | object)$$

$$class\ confidence\ score \equiv P_r(class_i) \cdot IoU$$

$$box\ confidence\ score \equiv P_r(object) \cdot IoU$$

$$confitional\ class\ probabillity = P_r(class_i | object)$$

where $P_r(object)$ is the probability that the box contains an object, $P_r(class_i|object)$ is the probability that the object belongs to $class_i$ given an object is presence, IoU is the IoU (intersection over union) between the predicted box and the ground truth, and $P_r(class_i)$ is the probability that the object belongs to $class_i$. For more details, each Bbox contains 5 elements: offsets to the corresponding cell x and y; width w, height h of the image, and a box confidence score (x, y, w, h).

B. Architecture Modification

In order to achieve the real-time detection capability using the NVIDIA Jetson TX2, a computing board, we modify the tiny YOLOv3 neural network to recognize the goods on the shelf. In this subsection, we only implemented a faster, light-weight version tiny YOLOv3 network, which only used 11 convolutional layers with shallower feature maps, as can be seen in Fig. 6 and 7. Table 1 shows the structure of the modified tiny YOLOv3 neural network. The basis for the revision is that the amount of computation required for convolution is large, and the categories is large, and the categories we use are less complex, so the number of convolution layers is reduced and the number of filters is reduced. After the experiment, the speed has met our needs, and the accuracy has not dropped too much because of the small category.

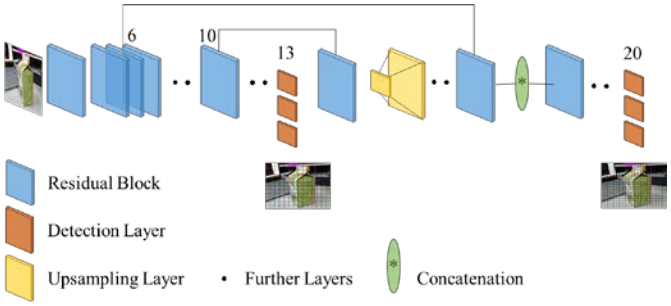

Figure 6. Architecture of the modified tiny YOLOv3 NN.

TABLE I
STRUCTURE OF THE PROPOSED TINY YOLOV3 NEURAL NETWORK.

Layer	Filters	Size/Stride	Input	Output
0 conv	16	3*3/1	416*416*3	416* 416*16
1 max		2*2/2	416*416*16	208*208*16
2 conv	32	3*3/1	208*208*16	208*208*32
3 max		2*2/2	208*208*32	104*104*32
4 conv	64	3*3/1	104*104*32	104*104*64
5 max		2*2/2	104*104*64	52*52*64
6 conv	128	3*3/1	52*52*64	52*52*128
7 max		2*2/2	52*52*128	26*26*128
8 conv	256	3*3/1	26*26*128	26*26*256
9 max		2*2/1	26*26*256	26*26*256
10 conv	64	1*1/1	26*26*256	26*26*64
11 conv	32	3*3/1	26*26*64	26*26*32
12 conv	24	1*1/1	26*26*32	26*26*24
yolo				
route	10 layer			
15 conv	32	1*1/1	26*26*64	26*26*32
upsample		2x	26*26*32	52*52*32
route	16 / 6 layer			
18 conv	128	3*3/1	52*52*160	52*52*128
19 conv	24	1*1/1	52*52*128	52*52*24
yolo				

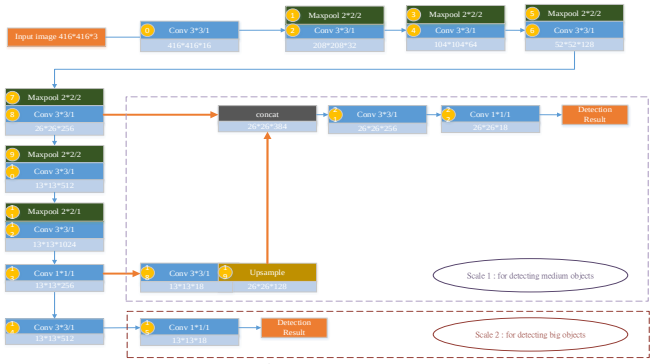

Figure 7. Modified tiny YOLOv3 Flowchart.

C. Fine-Tuning of the Pre-Trained Tiny YOLOv3 NN

To detect the customized object and increase the accuracy of the pre-trained tiny YOLOv3, we do fine-tuning of the network by our own datasets. First of all, the "various goods" dataset was created by using our own images from different scenes including outdoor, indoor and warehouse scenes with different lights and tonal. After taking pictures, we labeled each of them by hands. To date, about 2000 images have been constructed with labelled data in our dataset. Fig. 8 displays the five images from our "Goods" dataset. After creation of our own dataset, the YOLOv3 will be fine-tuned with its weights by using NVIDIA Jetson TX2 GPU board.

Figure 8. Various goods of our own datasets: (a) soymilk; (b) low sugur soymilk (LSsoymilk); (c) juice; (d) black tea (blackt); (e) green tea (greent); (f) ost soymilk (ost); (g) coke; (h) malz; (i) cookie.

V. Experimental Results and Discussion

This section presents the experimental results of the proposed autonomous quadrotor system in a demonstrative warehouse environment. The three experiments aim to show that the autonomous quadrotor system will complete the goods recognition task in the warehouse environment successfully. More importantly, the quadrotor will be shown able to fly in front of the shelf, scan the images of the shelf and carry high-performance computer board to recognize various goods by using the fish-eye calibration technique and modified tiny YOLOv3 neural network.

A. Fish-eye Lenses Calibration

The first experiment is conducted to show that the image calibration module is verified that it has ability to calibrate the images with fish-eye lens and chessboard into an accuracy image by using the proposed calibration algorithm. Fig. 9 displays the original images of the chessboard and the results of the calibrated images. Fig. 10 illustrates the calibration result of one original image. As can be seen in Fig. 9 and 10, the fish-eye images were calibrated successfully despite of the image zoom in due to calibration.

B. Modify and Fine-tuning of the Tiny YOLOv3 Network

The second experiment aims to examine whether the tiny YOLOv3 is successfully find-tuned with our own dataset. Fig. 11 shows the training curve, loss function and the mean average precision (mAP) of the network. The loss function continuously decayed and mAP was kept rising until the critical value was reached, during our training process. The result in Fig. 11 and Table 2 indicates that the tiny YOLOv3 has been successfully find-tuned with our own dataset.

C. Goods Recognition via Modified Tiny YOLOv3 Network

The third experiment is devoted to investigating if the fine-tuned modified tiny YOLOv3 network has the ability to identify various goods in the image. Fig. 12 depicts the recognition results of tiny YOLOv3 network, thereby showing that the network is capable of detecting and localizing the goods in different view angles and scenes. Furthermore, Fig. 13 shows that this network is able to detect various goods.

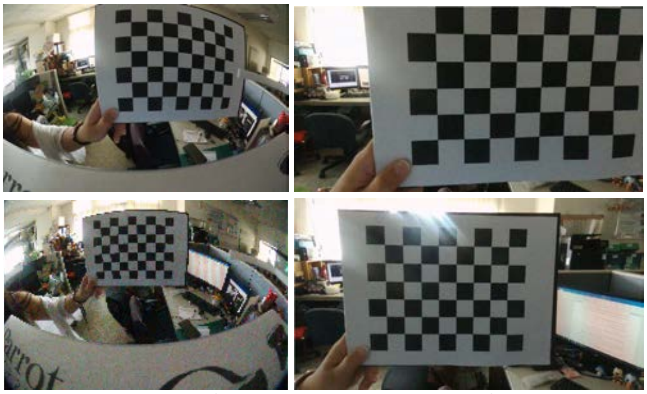

Figure 9. Comparison of original and calibrated images for the calibration chessboard.

Figure 10. Original image and its calibrated one.

TABLE II
COMPARISON OF MAP AND RECALL USING YOLOV3-TINY AND YOLOV3-LIGHT

	mAP (mean average precision)	recall	time (s)
YOLOv3-tiny	98%	90~95%	0.056
YOLOv3-Light	96%	88~93%	0.028

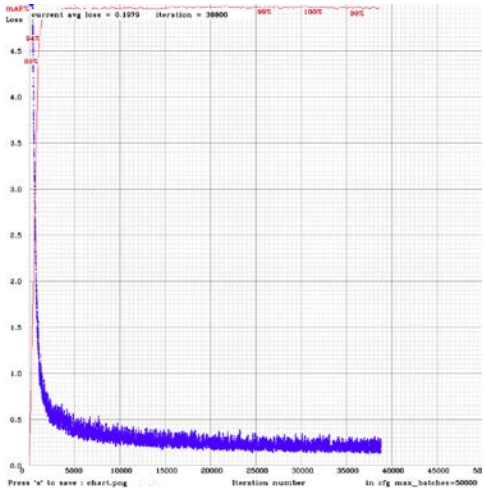

Figure 11. The mAP and loss function of the training process.

Figure 12. Recognition for incomplete goods with different angles.

Figure 13. Various and partially occluded drinks Recognition.

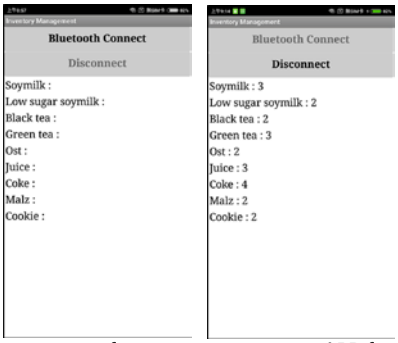

Figure 14. The experiment of inventory management APP for Android mobile phones.

D. Inventory Management System

Once the goods have been recognized using the modified tiny YOLOv3, the goods information will be transferred to the inventory system via Bluetooth. Since the autonomous quadrotor system is regarded as a transmitter, this system is used to transfer these goods information. The receiver of inventory system is an APP in an Android mobile phone, in order to have the advantages of convenience, flexibility and portability. Fig. 14 shows the Android APP working for the scenario in Fig. 13.

VI. Conclusion and Future Work

This paper has presented an autonomous quadrotor system with an improved tiny YOLOv3 neural network in indoor warehouse, in order to allow the system to scan goods, process the fish-eye calibration algorithm, execute the modified tiny YOLOv3 object detection, and ORB-SLAM2 algorithms. The autonomous quadrotor system has been implemented in the ROS environment. The quadrotor with an onboard camera has been exploited for scanning the images of the shelf and sending back these images to the computing module, NVIDIA Jetson TX2. The high-performance computing module has been shown to work well to process the fish-eye calibration algorithm and modified tiny YOLOv3 neural network. Through experimental results, the system has shown its effectiveness in recognizing the commodity in an indoor warehouse. An interesting topic for future work would be to integrate scanning trajectory method and a point of sales system into a more complete system.

Acknowledgments

The authors deeply acknowledge financial support from National Science Council, Taiwan, ROC, under contract NSC 107-2221-E-005-073-MY2.

References

[1] J. Zhang, Y. Lyu, T. Roppel, J. Patton, and C. P. Senthilkumar, “Mobile robot for retail inventory using RFID,” in *Proc.of 2016 IEEE Intern. Conf. on Industrial Technology (ICIT)*, Taipei, Taiwan, 2016.

[2] H. Yabushita, J. Shimamura, and M. Morimoto, "A framework of three-dimensional object recognition which needs only a few reference images," in *Proc. of the 21st International Conference on Pattern Recognition (ICPR2012)*, Tsukuba, 2012, pp. 1375-1378.

[3] J. Li, X. Wang, and H. Su, "Supermarket commodity identification using convolutional neural networks," in *Proc. of 2016 2nd International Conference on Cloud Computing and Internet of Things (CCIOT)*, Dalian, 2016, pp. 115-119.

[4] J. Redmon, S. Divvala, R. Girshick, and A. Farhadi, "You only look once: Unified, real-time object detection." In *Proc. of the IEEE Intern. Conf. on Computer Vision and Pattern Recognition*, 2016, pp.779-788.

[5] J. Redmon and A. Farhadi, "YOLO9000: Better, Faster, Stronger," in *Proc. of 2017 IEEE Intern. Conf. on Computer Vision and Pattern Recognition (CVPR)*, Honolulu, Hawaii, USA, 2017, pp. 6517-6525.

[6] J. Redmon and A. Farhadi, “YOLOv3: An Incremental Improvement,” *Computer Vision and Pattern Recognition (CVPR)*, arXiv:1804.02767v1, 8 Apr 2018.

[1] X. C. Lin and C. C. Tsai, “Cooperative SLAM of an indoor quadrotor flying together with a differential-driving automatic guided vehicle”, in *Proc. of* 2018 *Intern. Conf. on Advanced Robotics and Intelligent Systems*, Taipei, Taiwan, 28-31 August, 2018.

Hsiu-Chen Tsai received her bachelor and MS degrees from the Department of Electrical Engineering, National Chung Hsing University, Taichung, Taiwan, in 2015 and 2019, respectively. She is currently with Evergreen International Corporation, serving as an assistant engineer. Her current interests include deep learning, unmanned vehicles, image processing and big-data analysis.

Ching-Chih Tsai received the Diplomat in Electrical Engineering from National Taipei Institute of Technology, Taipei, Taiwan, ROC, the MS degree in Control Engineering from National Chiao Tung University, Hsinchu, Taiwan, ROC, and the Ph.D degree in Electrical Engineering from Northwestern University, Evanston, IL, USA, in 1981, 1986 and 1991, respectively. Currently, he is currently a life distinguished professor in the Department of Electrical Engineering, National Chung-Hsing University, Taichung, Taiwan, where he served the Chairman in the Department of Electrical Engineering from 2012 to 2014. He is a Fellow of IEEE, IET, CACS and RST (Robotics Society of Taiwan).

Dr. Tsai served as the Chair, Taipei Chapter, IEEE Control Systems Society, from 2000 to 2003, and the Chair, Taipei Chapter, IEEE Robotics and Automation Society from 2005 to 2006. In 2007, he was the program chair of 2007 CACS international automatic conference sponsored by Taipei chapter, IEEE control systems society. In 2010, he served as the program co-chair of SICE 2010 annual conference in Taiwan, which was technically sponsored by IEEE CSS; in 2011, he served as the General Chair, 2011 International conference on service and interactive robotics; in 2012, he has served as the General Chair, 2012 International conference on Fuzzy Theory and Its Applications, the General Chair, 2012-2015 CACS International Automatic Control Conferences, and the General Chair, 2016-2017 International Conference on Advanced Robotics and Intelligent Systems. Dr. Tsai served the two-term President, Chinese Institute of Engineers in Central Taiwan, Taiwan from 2007 to 2011, and two-term President of Chinese Automatic Control Society from 2012 to 2015. Since 2008, he has been the Executive Directors in

Boards of Government of thee professional associations, including Robotic Society of Taiwan, Taiwan Fuzzy Systems Association, and Taiwan Systems Association. He has served as the Chair, Taichung Chapter, IEEE Systems, Man, and Cybernetics Society since 2009, the Chair of IEEE SMC Technical Committee on intelligent learning in control systems since 2009, the two-term President of Robotics Society of Taiwan since 2016, the steering committee of Asian Control Association since 2014, a BOG member of IEEE Nanotechnology council since 2012, the President-Elect of International Fuzzy Systems Association since 2019, and a BOG member of the IEEE SMCS since 2017.

Dr. Tsai has published more than 500 technical papers, and seven atents in the fields of control theory, systems technology and applications. Dr. Tsai is respectively the recipients of the Third Society Prize Paper Award from IEEE Industry Application Society in 1998, the Outstanding Automatic Control Engineering Award in 2008 from Chinese Automatic Control Society (CACS), and the Outstanding Engineering Professor Award in 2009 from the Chinese Institute of Engineers in 2009, the IEEE Most Active SMC Technical Committee (TC) Award in 2012 from IEEE SMC Society, the Outstanding Electrical Engineering Professor Award from the Chinese Institute of Electrical Engineering in 2014, Outstanding Industry Contribution Award from Taiwan Systems Association in 2016, the best paper award in the International Journal of Fuzzy Systems in 2017, and many best paper awards from many international conferences technically supported by IEEE. He is the advisor, IEEE SMC student branch chapter at National Chung Hsing University; this chapter was the recipient of certificate of appreciation from IEEE SMCS in 2009. He has served as the associate editors of International Journal of Fuzzy Systems, and IEEE Transactions on Systems, Man and Cybernetics: Systems, IEEE Transactions on Industry Informatics, and International Journal of Electrical Engineering. Recently, he has served as the Editor-in-Chief of a new international robotics journal called “iRobotics”. His current interests include advanced nonlinear control methods, deep model predictive control, fuzzy control, neural-network control, advanced mobile robotics, intelligent service robotics, intelligent mechatronics, intelligent learning control methods with their applications to industrial processes and intelligent machinery.

Flip-and-Leap in a Hexapod Robot

Shou-Li Hsu, Kuan-Wei Liu, Chia-Ho Hsiung, Syuan-Yu Chen, Ting-Hao Wang, and Pei-Chun Lin

***Abstract*—This article introduces the behavior development of a flip-and-leap gait in an RHex-style hexapod robot. Owing to the dynamic characteristics of the behavior, as well as the limited actuation freedom of the RHex-style robot, the development relies on understanding the dynamics of the robot through its reduced-order representation. The model consists of a planar rigid body and three spring-loaded compliant rolling legs. The parameters and initial motion conditions were varied to evaluate the dynamic response of the model, providing the control hint to initiate such behaviors. The proposed strategy was experimentally validated, and the results confirm that the RHex-style robot can perform a flip-and-leap behavior, which could be useful for negotiating harsh terrain.**

***Index Terms*—hexapod robot, model, flipping, leaping, gait**

I. Introduction

BIONICS [1-8], getting inspiration from nature to solve technological problems, has not been out of fashion in science research since it was proposed in the 1960s. The application of bionics is extremely broad. For instance, the design and construction of interior space in a hospital were inspired by the anti-microorganism skin of sharks, and the environmentally friendly structure without an air-conditioning system was inspired by a climate control behavior performed by termites.

The hexapod robot, or RHex [9], is a classic application of robotics in bionics, as shown in Fig. 1(a). Developed from observing and intimating the motion of cockroaches, though RHex only has one rotational degree-of-freedom per leg, it is good at negotiating challenging terrains. With powerful motors, a high-capacity battery, and diverse sensors, the robot can complete behaviors. It can also carry out advanced missions such as going up and down stairs, climbing over an obstacle, and self-righting as it falls over [10]. Some researchers have replaced the legs with other shapes or materials for special purposes. For example, AQUA could swim underwater with fins [11], and the Wheel-RHex moves smoothly and efficiently on a flat floor using changeable wheels. Moreover, there are robots developed for military use with waterproof, anti-dust aluminum cases, larger battery capacity and more powerful motors, such as Rugged RHex.

In addition to a variety of novel mechanism designs, the gait design enables the robots to have greater agility for negotiating the environment. Some dynamic behaviors have been conducted with RHex, such as running [12], stair ascent [13, 14], stair descent [15], bounding [16], pronking [17], self-righting [10], and leaping [18], by finding an appropriate state sequence. In this research, we focused on the flipping and leaping gait for the advantages of its outstanding ability to negotiate obstacles. For a hexapod robot, flipping provides great vertical displacement for the body centroid and allows the robot to perform more complicated actions. However, as terrain becomes rougher, leaping becomes more appropriate because it requires little ground contact to overcome the terrains. Therefore, the development and combination of a flipping and leaping gait improves the traversing ability of RHex.

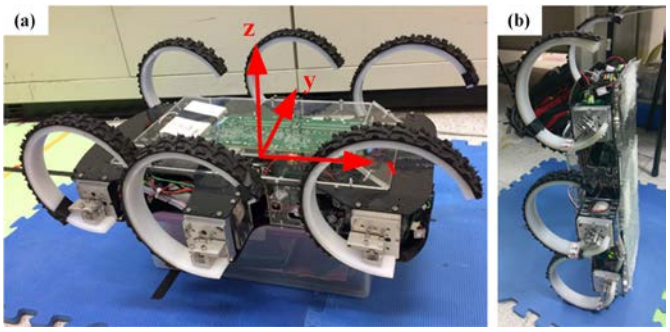

Figure 1. The RHex-style robot: (a) in resting posture and (b) in erect posture.

Based on our previous model-based strategy for initiating a robot's dynamic behavior, we aimed to understand the flipping/leaping mechanism. More specifically, a planar rigid-body model with three compliant C-shaped legs was constructed so that the force and moment, as well as the resultant motion to the body, could be investigated. The model had spring-loaded compliant legs with rolling contact, and the configuration was similar to the two-rolling-leg model as previously reported [19]. Compared with a previous study of running [12] and running-to-leaping maneuvers [18] in a hexapod robot, this study explored a wider parameter domain and focused on the key factors that determined the initiation of either leaping or flipping behaviors from a resting and running posture. The contributions of the study include 1) analysis of the parameters that affect the model's leaping or flipping behaviors; and 2) a model-based approach so that the empirical robot can perform the desired behavior without exhaustive searching or testing.

The remainder of this paper is organized as follows: Section II introduces the flipping gait algorithm; Section III describes the simulation settings and the consequences of the model with varying parameters; Section IV reports the experimental results using an RHex robot; and Section V concludes the work.

This work is supported by Ministry of Science and Technology (MoST), Taiwan, under contract: MOST 107-2634-F-002-004-, MOST 108-2634-F-002-002-, and MOST 109-2634-F-002-039-.

Authors are in the department of Mechanical Engineering, National Taiwan University (NTU), No.1 Roosevelt Rd. Sec.4, Taipei 106, Taiwan. (Corresponding email: peichunlin@ntu.edu.tw).

II. Flipping and Flipping-Related Gaits Algorithm

A. Introduction of Flipping and Flipping-Related Gaits

The flipping model was symmetric with respect to the x-axis along the long side of the body, as defined in Fig. 1(a), whereas the rotational axis was parallel to the y-axis. During the flipping process, the robot first lies down with the end of the legs touching the ground, as shown in Fig. 2(a). Next, the robot tilts the body with one end on the ground by giving the rear legs a torque command, as shown in Fig. 2(b). After a delay of several hundred milliseconds, the robot gives the middle and fore legs torque commands to increase the body pitch, denoted as θ_y, until flipping upside down, as shown in Fig. 2(c). After that, the six legs are set in the same phase, or what is called a standing posture, to prepare for landing, as shown in Fig. 2(d) and (e).

Continuous flipping combines the flipping and the reverse flipping, which uses the reverse of the execution sequence of each leg with opposite phase already mentioned, which enables the robot to flip back and forth to overcome obstacles such as a high step or a ditch. Alternatively, the flip-to-erect gait, as shown in Fig. 3, was used to stop the procedure while the body was maintained vertical by the fore legs, and it could be utilized to initiate further dynamic gaits.

B. The Flip-and-Leap Gait

The flipping gait, however, cannot make the robot move forward since the reacting forces from the ground are vertical, so the robot could only move up and down. Therefore, we further developed the flip-and-leap gait for the robot to leap forward and even leap up a step. The flip-and-leap gait is completed through a process of chained gaits, including tripod, flipping, and leaping. The detailed procedure, as shown in Fig. 4, could be separated into the following four steps:

1) RHex walks by tripod gait to the setting location where the robot is going to flip.

2) The robot makes a small leap, thrust by the set of all legs striking the ground (the first section of the leaping gait). The purpose of this small leap is to synchronize the phases of the six legs for the upcoming flip. Additionally, the increment of the body pitch during the small leap is also the key variable for the flipping afterward.

3) While the rear legs hit the ground, the robot executes the flipping gait by triggering the rear, middle, and fore legs chronologically. As the body lifts off the ground, the phases of the fore legs are set to the initial position for leaping.

4) Following the perception at the best pitch angle after the robot flips 90 degrees, the front legs step on the ground and push the robot forward and upward, which allows the robot up the step without leaning.

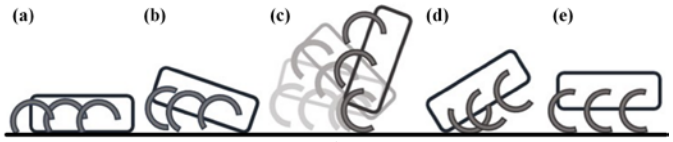

Figure 2. Flipping procedure initiated from (a) the resting posture; (b) and (c) the body was tilted through the sequence impulse driven by the rear legs, middle legs, and fore legs. Afterward, (d) the phases of the legs were synchronized to perform (e) the standing gait for landing.

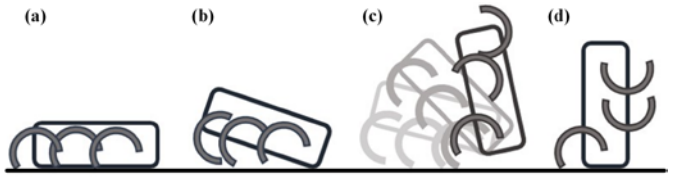

Figure 3. Flip-to-erect procedure initiated from (a) the resting posture. Next, (b) and (c) are the chronological impulses from the rear legs, mid legs, and fore legs that tilted the body. Finally, (d) the body was vertically maintained using the fore legs.

III. Simulation of the Flip-and-Leap Gait

A. Simulation Using the R-SLIP Model

To optimize the variables for triggering the complex flip-and-leap gait, we disassembled the complete flip-and-leap procedure into different sections and utilized the planar model with different initial conditions to evaluate the performance outcome. Among several template-style models, such as SLIP [20, 21], SLIP-T [22], and SLIP-R [23], we found that the successor of the R-SLIP [12], the TDR-SLIP [24] which configures a linear torsional spring and damper on an approximately half-circular, massless, and compliant rolling leg is resemble to the RHex leg, so it was adopted in the simulation. The simulation was implemented on MATLAB Simulink with separated subsystems, which simplified the process of deriving equations of motion under the complex combination of different gaits.

The planar model could move freely in the space and had a six degree-of-freedom (DOF) joint connected to the world frame, which provided geometric constraints and contact forces. We connected the solid body and legs of the robot to the sphere to plane force block introduced in the Contact Forces Library, and it was able to translate and rotate between the world frame

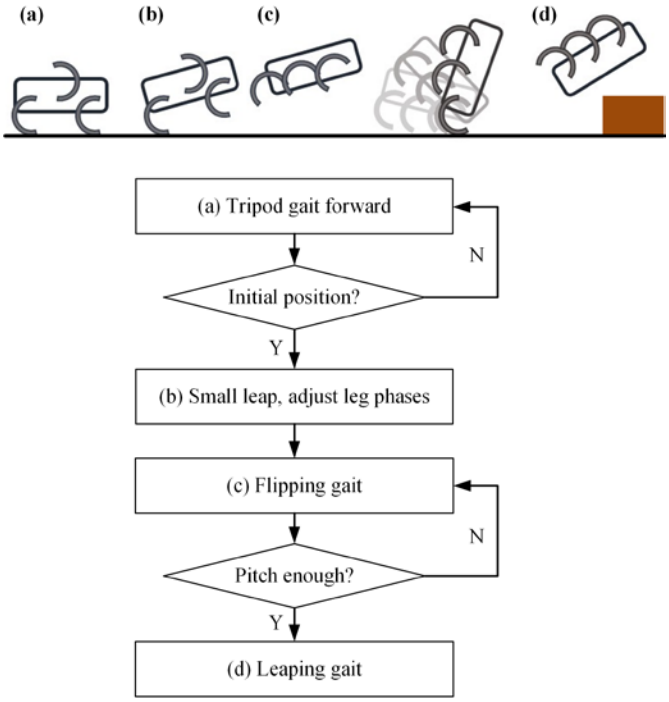

Figure 4. The sequential motion and a flow chart of the flip-and-leap behavior: (a) tripod walking/running, (b) small leaping, (c) flipping, and (d) leaping.

and the body frame. The knee joints were actuated by input torque profiles to implement the flipping and leaping gait, and the data, including the pitch angle θ_y, pitch angular velocity $\dot{\theta}_y$, and position and velocity of center of mass (CoM), were recorded for analysis. Here, we will focus on the leaping gait specifically since it is more complicated than others.

B. *Analysis of the Flipping Gait*

We explored the optimized body movement in the flipping gait with different parameters. The flipping gait involves three phases: the actuation of the rear legs, the middle legs, and the fore legs. The motion of each leg was commanded through torque control, and each motor performed maximum output with the same trajectory. The command latency for a separated set of legs, denoted as T_{rear}, T_{middle}, and T_{fore}, was the key for successful flipping. Without a proper delay time, the robot might leap height without flipping or could not overcome the gravitational force to flip upside down.

We started the analysis by assuming that T_{middle} and T_{fore} are independent and then plotted the variation of pitch angle θ_y under the different T_{middle} and T_{fore}, as shown in Fig. 5(a) and (b). We thus obtained a set of command latency with which the robot can achieve the maximum pitch angle θ_y.

To substantiate the assumption that T_{middle} and T_{fore} are independent, a trial simultaneously considered both variables, as shown in Fig. 6. The color plot represents the value of maximum pitch angle θ_y found among the time-sequence data. The variation trend of either T_{middle} or T_{fore} was roughly similar as the other parameter varied, and hence, we assumed the variables to be independent for simplification. Note that we did not always apply the best result from the simulation because the circumstances might require a specific initial condition during practical cases.

C. *Analysis of Leaping Gait*

In this section, we further discuss the dynamic effect of the leaping gait with different changes, including initial pitch angle, initial angle and stiffness of torsional springs on the leg, and the influences on the assistance of the fore and middle legs.

1) *Initial Pitch Angle* θ_{y,t_0}

Because the leaping gait came after the flipping gait, we assumed that the robot had fallen from the upright position. In consequence, it had a higher initial pitch angular velocity $\dot{\theta}_{y,t_0}$ with smaller initial pitch angle θ_{y,t_0}. When the θ_{y,t_0} went smaller, the friction was not enough to turn θ_y back because of the high $\dot{\theta}_y$, and the robot fell to the ground shortly after the start. In contrast, as the θ_{y,t_0} became larger, the duration of contact between the legs and the ground became longer and caused the robot to fall backward. Thus θ_{y,t_0} should be carefully selected so that the robot can leap as high as possible. Fig. 7(a) shows the CoM_g and θ_y with different θ_{y,t_0}. Thus, the proper θ_{y,t_0} was chosen to be about 40 to 45 degrees.

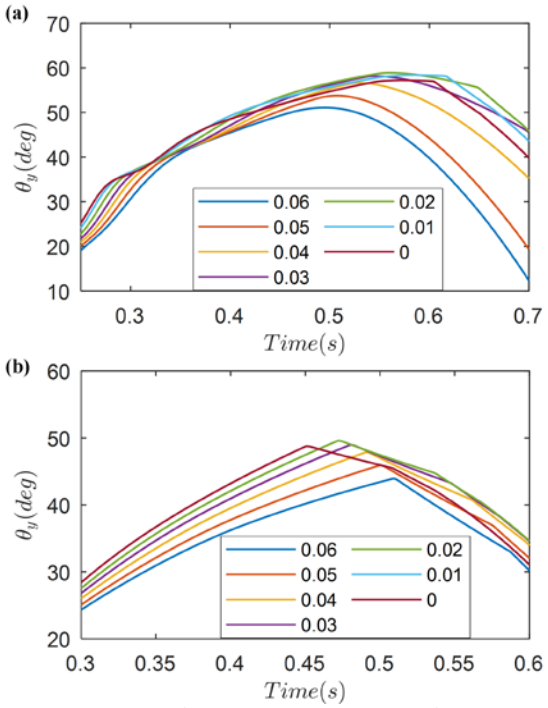

Figure 5. The pitch angle of the model under variations of (a) T_{middle} and (b) T_{fore}.

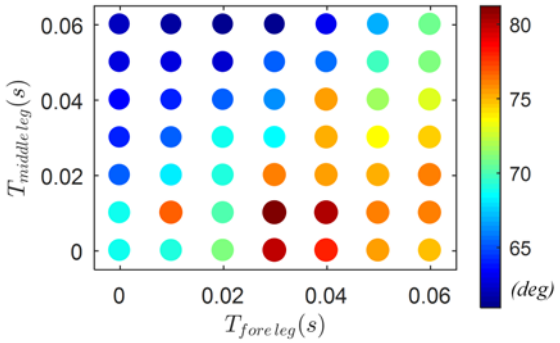

Figure 6. The maximum θ_y of the model with different T_{middle} and T_{fore}.

2) *Initial Angle of Torsional Springs on the Legs*

The initial angle of torsional springs on the legs affected the normal force from the ground and the contact time between the legs and the ground, which contributed to the θ_y and CoM_z as mentioned in 1). Fig. 7(b) shows the relationship of CoM_z and θ_y with different initial angles of the torsional springs. The trend of the data matched the above prediction.

3) *With Actuation of Fore and Middle Legs*

When performing a standing long leap, we swung the arms to increase the forward inertia using the remaining four legs. We utilized a step function to trigger the knee angle for simplicity, and the only variable was the final knee angle position, as shown in Fig. 7(c). As the final knee angle approached 270 degrees, the $\dot{CoM}_x$ went higher with the rise of CoM_z.

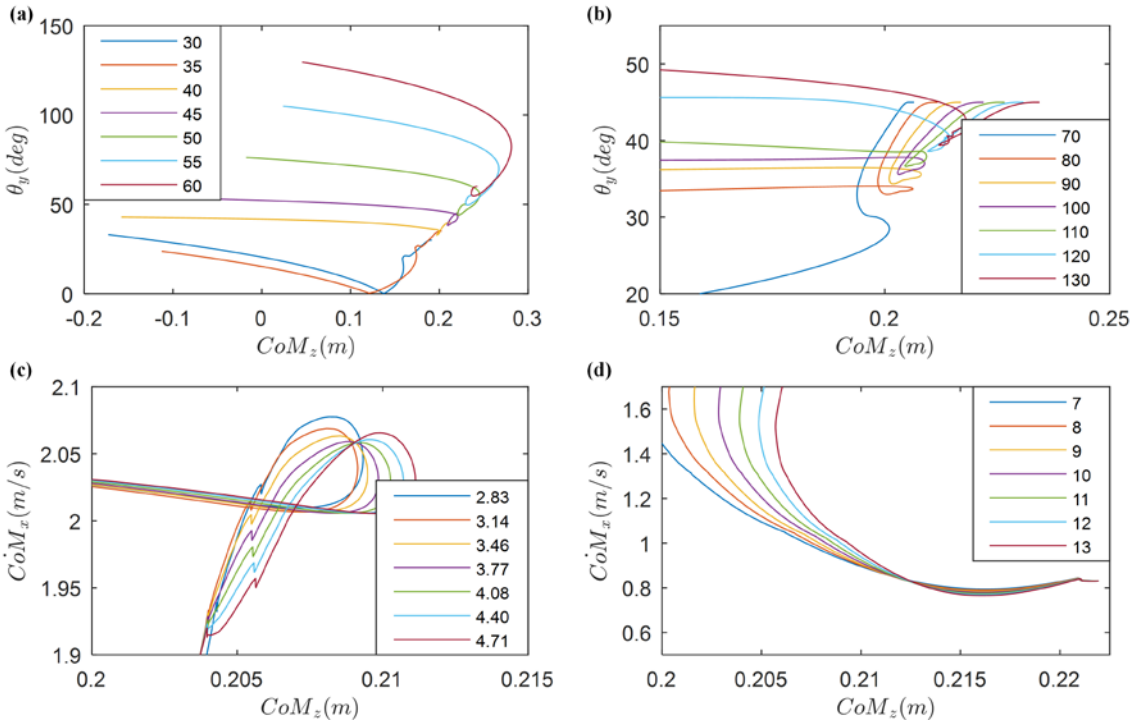

Figure 7. Relations of CoM_z-θ_y and CoM_z - $\dot{CoM}_x$ of the model under parameter variations: (a) initial pitch angle θ_{y,t_0}; (b) initial angle of torsional springs; (c) actuation of fore and middle legs; and (d) the stiffness of the torsional spring.

4) The Stiffness of the Torsional Springs on the Legs

The characteristics of the legs may affect the dynamics of the robot, and the selection of different stiffnesses of the torsional spring joint of the legs influenced the energy consumption and the normal force from the ground. Fig. 7(d) shows the plot of CoM_z to $\dot{CoM}_x$ under varied stiffnesses of the torsional springs. The robot had a larger $\dot{CoM}_x$ and higher CoM_z as the stiffness was increased because the springs had a dampening effect and absorbed more energy with less stiffness.

IV. Experiment

The RHex-style robot shown in Fig. 1(a) was used to evaluate the performance of the flip-and-leap gait developed and simulated as previously discussed. A six-axis inertial measurement unit (IMU) was installed in the robot, which allowed the feedback of the pitch angle θ_y.

In this case, the time delay between each pair of legs in the flipping section was selected from the optimization discussed in the Section III. The T_{middle} and T_{fore} were selected to be 40 and 45 ms. The experiments showed that the robot successfully flipped while consuming less energy. Similarly, the leaping pitch angle θ_y was also given by the successful simulation data, which in this case was 130 deg. The final stages of the flipping gait were the main factors that determined whether the flip-and-leap gait was successful. Therefore, the parameters for controlling the flipping gait were tuned precisely to ensure that the flip-and-leap gait would not fail. Fig. 8(a) is a sequence of snapshots taken during the flipping experiment, and Fig. 8(b) is the corresponding simulation in Simulink. Most of the characteristics of the flipping gait in the experiment and the simulation were similar. Due to the energy loss of the slipping condition between the feet and the ground, the maximum height of flipping in the experiment was slightly lower than in the simulation.

The RHex robot needed to process the IMU data in order to determine the timing of leaping. A trivial approach was to directly multiply the $\ddot{CoM}_z$ by the $\cos\theta_y$. When the robot was horizontal, $\ddot{CoM}_z$ should equal the gravity acceleration constant. In our case, the pitch angle of 130 degrees at the beginning of the leaping gait was required, so the leaping gait should be triggered when $\ddot{CoM}_z = -6.3057$ (m/s^2). The IMU data of the flipping gait are shown in Fig. 10, where the unit of $\ddot{CoM}$ was the gravity acceleration constant. The outcome showed that the IMU data were followed by a lot of signal noise.

Further filtering techniques for a more precise triggering point led to latency problem. Therefore, we chose to integrate $\dot{\theta}_y$ for a more accurate estimation of θ_y, and the robot triggered the leaping gait with precise timing. Fig. 9(a) shows the sequence of snapshots during the flip-and-leap experiment, and Fig.9 (b) shows the sequence of the leaping simulation. When the elastic potential energy of the fore pair of legs reached a maximum, the legs underwent a tremendous deformation, which caused the distortion of the R-SLIP model. Therefore, the robot in the simulation could not leap as high as in the experiment.

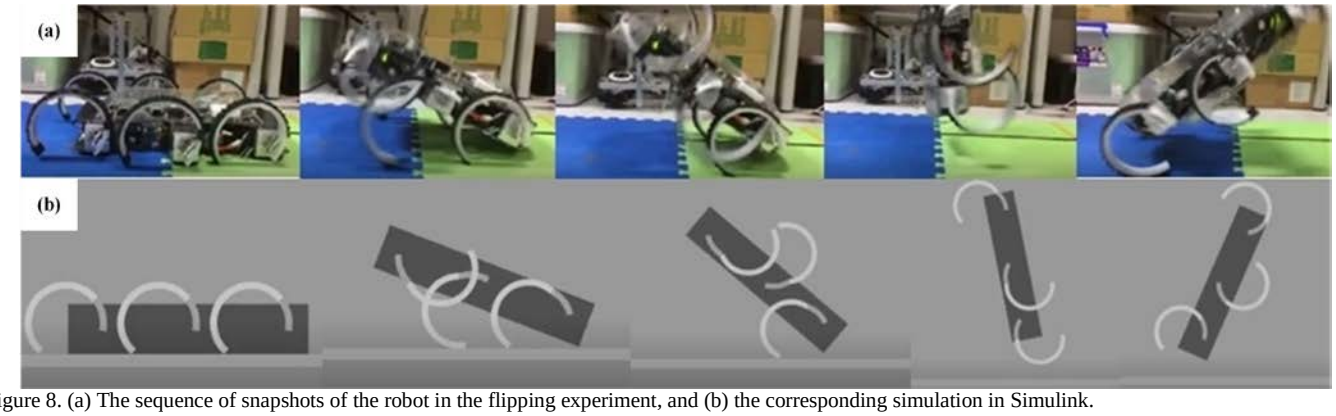

Figure 8. (a) The sequence of snapshots of the robot in the flipping experiment, and (b) the corresponding simulation in Simulink.

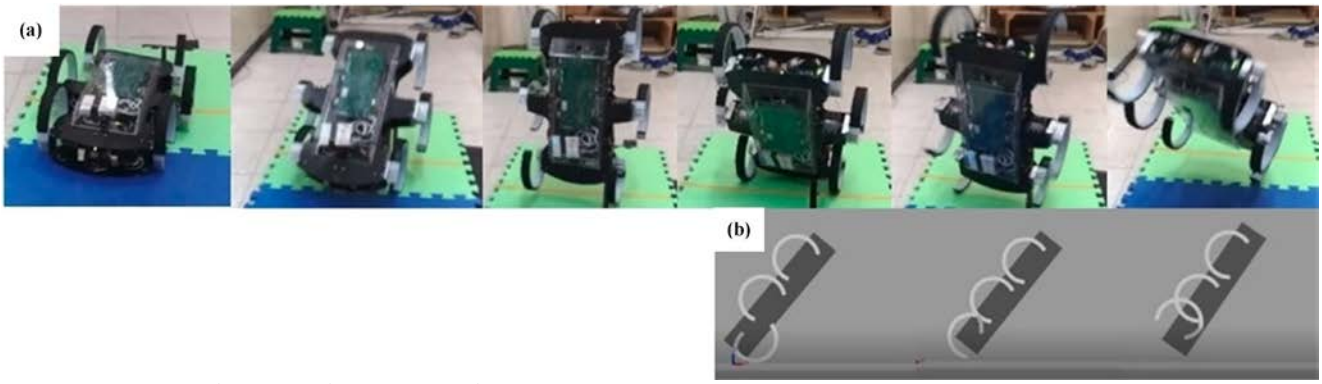

Figure 9. (a) The sequence of snapshots of the robot in the flip-and-leap experiment, and (b) the corresponding simulation in Simulink.

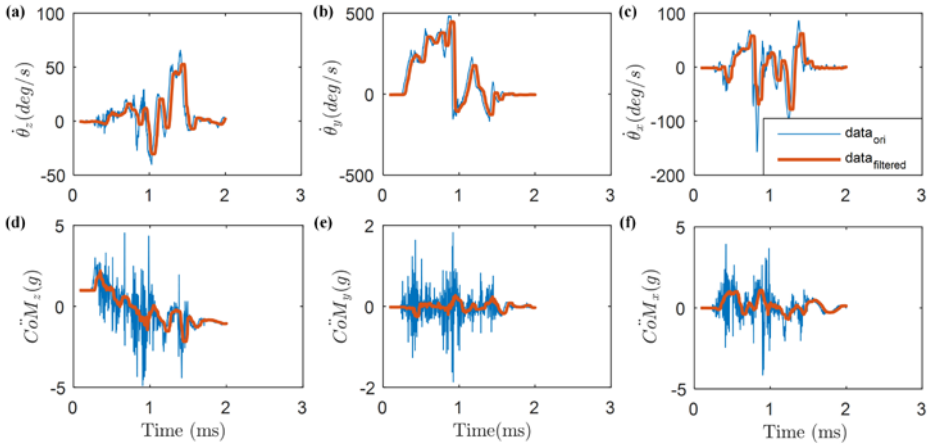

Figure 10. The IMU data of the robot in flipping. The blue and red curves represent raw data and filtered data, respectively.

V. Conclusion

In this paper, we introduced applications based on the flipping gait. Also, we reported on the methodology to optimize the parameters to trigger the flipping and leaping gaits using the R-SLIP model on Simulink, and further realized the gaits on RHex.

To minimize the distortion of the R-SLIP model, we placed the torsional spring position at 50 degrees with respect to the motor shaft and the center of the leg. The parameters, including T_{middle}, T_{fore}, θ_{y,t_0}, angle of torsional spring, actuations of middle legs and rear legs, and stiffness of the torsional springs, were tuned and compared in the simulation. Using the optimization process mentioned in Section III, our robot successfully accomplished the flip-and-leap motion.

Note that although the optimized θ_{y,t_0} was about 40 to 45 degrees, the result was based on the need of highest leaping height. In fact, the robot could adjust the parameters of the leaping gait according to the shape of the stairs to adapt to the terrain and thus increase the efficiency.

A further process of introducing better sensory feedback would allow the robot to know the distance from the target step and allow it to trigger the flip-and-leap gait automatically, providing more versatile usage in the future.

Multimedia

A video of the flipping and leaping with RHex is available at https://youtu.be/1DFbDnFpfCs.

REFERENCES

[1] Y. Fukuoka, H. Kimura, and A. H. Cohen, "Adaptive dynamic walking of a quadruped robot on irregular terrain based on biological concepts," (in English), *The International Journal of Robotics Research*, Article; Proceedings Paper vol. 22, no. 3-4, pp. 187-202, Mar-Apr 2003, doi: 10.1177/0278364903022003004.

[2] H. Kimura, Y. Fukuoka, and A. H. Cohen, "Adaptive dynamic walking of a quadruped robot on natural ground based on biological concepts," *The International Journal of Robotics Research*, vol. 26, no. 5, pp. 475-490, May 2007. [Online]. Available: <Go to ISI>://000246338400003.

[3] D. J. Hyun, S. Seok, J. Lee, and S. Kim, "High speed trot-running: Implementation of a hierarchical controller using proprioceptive impedance control on the MIT Cheetah," *The International Journal of Robotics Research*, vol. 33, no. 11, pp. 1417-1445, 2014, doi: 10.1177/0278364914532150.

[4] H. W. Park, P. M. Wensing, and S. Kim, "High-speed bounding with the MIT Cheetah 2: Control design and experiments," *The International Journal of Robotics Research*, Article vol. 36, no. 2, pp. 167-192, Feb 2017, doi: 10.1177/0278364917694244.

[5] A. De and D. E. Koditschek, "Vertical hopper compositions for preflexive and feedback-stabilized quadrupedal bounding, pacing, pronking, and trotting," *The International Journal of Robotics Research*, vol. 37, no. 7, pp. 743-778, 2018, doi: 10.1177/0278364918779874.

[6] J. G. Cham, S. A. Bailey, J. E. Clark, R. J. Full, and M. R. Cutkosky, "Fast and robust: Hexapedal robots via shape deposition manufacturing," *International Journal of Robotics Research*, vol. 21, no. 10-11, pp. 869-882, Oct-Nov 2002. [Online]. Available: <Go to ISI>://000181344700005.

[7] J. G. Cham, J. K. Karpick, and M. R. Cutkosky, "Stride period adaptation of a biomimetic running hexapod," *International Journal of Robotics Research*, vol. 23, no. 2, pp. 141-153, Feb 2004. [Online]. Available: <Go to ISI>://000188890700005.

[8] S. Kim, J. E. Clark, and M. R. Cutkosky, "iSprawl: Design and tuning for high-speed autonomous open-loop running," *International Journal of Robotics Research*, vol. 25, no. 9, pp. 903-912, Sep 2006. [Online]. Available: <Go to ISI>://000240939900007.

[9] U. Saranli, M. Buehler, and D. E. Koditschek, "RHex: A simple and highly mobile hexapod robot," *The International Journal of Robotics Research*, vol. 20, no. 7, pp. 616-631, 2001.

[10] U. Saranli, A. A. Rizzi, and D. E. Koditschek, "Model-Based Dynamic Self-Righting Maneuvers for a Hexapedal Robot," *International Journal of Robotics Research*, vol. 23, no. 9, pp. 903-918, 2004, doi: 10.1177/0278364904045594.

[11] G. Dudek *et al.*, "AQUA: an amphibious autonomous robot," *Computer*, vol. 40, no. 1, pp. 46-53, 2007, doi: 10.1109/MC.2007.6.

[12] K. J. Huang, C. K. Huang, and P. C. Lin, "A Simple Running Model with Rolling Contact and Its Role as a Template for Dynamic Locomotion on a Hexapod Robot," *Bioinspiration & Biomimetics*, vol. 9, p. 046004 (20pp), 2014.

[13] E. Z. Moore and M. Buehler, "Stable Stair Climbing in a Simple Hexapod Robot," presented at the International Conference on Climbing and Walking Robots (CLAWAR), 2001.

[14] E. Z. Moore, D. Campbell, F. Grimminger, and M. Buehler, "Reliable Stair Climbing in the Simple Hexapod RHex," in *IEEE International Conference on Robotics and Automation (ICRA)*, 2002, pp. 2222-2227.

[15] D. Campbell and M. Buehler, "Stair Descent in the Simple Hexapod RHex," in *IEEE International Conference on Robotics and Automation (ICRA)*, 2003, pp. 1380-1385.

[16] D. Campbell and M. Buehler, "Preliminary bounding experiments in a dynamic hexapod," *Experimental Robotics VIII*, pp. 612-621, 2003.

[17] D. McMordle and M. Buehler, "Towards pronking with a hexapod robot," Mcgill Research Centre for Intelligemt Machines Montreal (QUEBEC), 2001.

[18] Y. C. Chou, K. J. Huang, W. S. Yu, and P. C. Lin, "Model-Based Development of Leaping in a Hexapod Robot," *IEEE Transactions on Robotics*, vol. 31, no. 1, pp. 40-54, 2015, doi: 10.1109/TRO.2014.2376141.

[19] C. K. Huang, C. L. Chen, C. J. Hu, and P. C. Lin, "Model-based bounding on a quadruped robot," in *IEEE International Conference on Robotics and Automation (ICRA)*, 16-21 May 2016 2016, pp. 3576-3581, doi: 10.1109/ICRA.2016.7487540.

[20] R. M. Alexander, *Elastic mechanisms in animal movement* Cambridge University Press 1988.

[21] T. A. McMahon and G. C. Cheng, "The mechanics of running: How does stiffness couple with speed?," *Journal of Biomechanics*, vol. 23, pp. 65-78, 1990, doi: http://dx.doi.org/10.1016/0021-9290(90)90042-2.

[22] M. M. Ankaralı and U. Saranlı, "Control of underactuated planar pronking through an embedded spring-mass Hopper template," *Autonomous Robots*, vol. 30, no. 2, pp. 217-231, 2011, doi: 10.1007/s10514-010-9216-x.

[23] J. Y. Jun and J. E. Clark, "Effect of rolling on running performance," in *IEEE International Conference on Robotics and Automation (ICRA)*, 2011, pp. 2009-2014, doi: 10.1109/ICRA.2011.5980433.

[24] C. J. Hu, T. K. H. Wang, C. K., and P. C. Lin, "A torque-actuated dissipative spring loaded inverted pendulum model with rolling contact and its application to hexapod running," *Bioinspiration and Biomimetics*, vol. 14, 2019, Art no. 026005.

Shou-Li Hsu received the double degree of B.S. in mechanical engineering and electrical engineering from National Taiwan University (NTU), Taipei, Taiwan, in 2019. His primary research area pertained to bio-inspired robots, digital integrated circuits, and monolithic mmWave integrated circuits.

Kuan-Wei Liu received the B.S. degree in mechanical engineering from National Taiwan University (NTU), Taipei, Taiwan, in 2019. He is currently studying at Texas A&M University M.S. degree in mechanical engineering at Texas, USA. His current interests include robotic perceptions and motion planning.

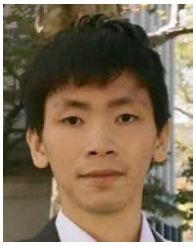

Chia-Ho Hsiung received the bachelor's degree in mechanical engineering from National Taiwan University (NTU), Taipei, Taiwan, in 2019. Currently, He is pursuing his master's degree in mechanical engineering with concentration in robotics and control at Columbia University in the City of New York. He is interested in motion planning and robot learning.

Hsuan-Yu Chen received the B.S. degree in mechanical engineering in 2018 from National Taiwan University (NTU), Taipei, Taiwan, where she is working toward the M.S. degree in mechanical engineering. Her current research interests include mechanism design, robot dynamics and control, and bio-inspired robotics.

Ting-Hao Wang received the B.S. and M.S. degrees in mechanical engineering from National Taiwan University (NTU), Taipei, Taiwan, R.O.C., in 2016 and 2018, respectively. His research interests include mechanism design, dynamics and control, and motion planning.

Pei-Chun Lin received the B.S. and M.S. degrees in mechanical engineering from National Taiwan University (NTU), Taipei, Taiwan, R.O.C., in 1996 and 1998, respectively, and the M.S. degree in electrical engineering and computer science and the Ph.D. degree in mechanical engineering from University of Michigan, Ann Arbor, MI, USA, in 2005.

He was a Postdoctoral Research Fellow in the Department of Materials Science and Engineering, University of Pennsylvania, Philadelphia, PA, USA, from 2005 to 2007. Currently, he is a Professor in the Department of Mechanical Engineering, NTU. His research interests include bio-inspired robotics, mechanical design, sensor design/fusion, control, dynamic locomotion, and compliant composites.

RGB-D SLAM of an Indoor Omnidirectional Mobile Robot with an Improved RRT

Po-An Wei, Ching-Chih Tsai, *Fellow, RST,* and Feng-Chun Tai

***Abstract*—This paper presents techniques and methodologies to address the three-dimensional (3D) SLAM problem by using an indoor Mecanum-wheeled omnidirectional robot (MWOR) and the Robot Operating System (ROS) middleware. The experimental mobile robot is equipped with one Linux-based TX2 computing board, one RealSense RGB-D camera, one LiDAR and an open-CR control board and ROS software, where the LiDAR is used to achieve obstacle avoidance. This mobile robot uses an improved complete-coverage exploration algorithm, an improved RRT algorithm, and an existing RGB-D SLAM algorithm to builds its 3D environment map, which will be transmitted to a host computer through topic in ROS via a wireless network. The effectiveness and usefulness of the proposed 3D SLAM method together with the improved RRT algorithm are exemplified by conducting several experiments on the experimental MWOR.**

***Index Terms*—Exploration, Mecanum-wheeled omnidirectional robot (MWOR), ROS (Robot Operating System), RGB-D SLAM (Simultaneous Localization and Mapping).**

I. Introduction

In recent years, ROS (Robot Operating System) [1-3], developed by Stanford Artificial intelligence lab, has received increasing popularity in robotics community. ROS has made extraordinary contributions to provide several solutions for robotics, such as motion control, SLAM, navigation, and exploration. ROS is one of the widely used middleware to develop robotics applications and represents an important milestone in the development of modular software for robots. It now has gained wide currency for the creation of working robotic systems, initially in the laboratory but now also in industry. In ROS, a node is defined as an application, and different nodes are able to communicate with each other through topic, service, and action in ROS. ROS contains many open source packages including OROCOS, OpenRave, Player, OpenCV, OMPL, and Gazebo, which are able to accelerate advanced research on robotics. To date, ROS has been applied in many research areas and industrial applications [4-6]; in particular, SLAM in ROS has received much attention over past and present decades due to its really successful applications such as cleaning robot, unmanned aerial vehicle (UAV), drone, automatic ground vehicle (AGV), and so on.

SLAM technique is indeed a chicken-or-egg problem which a robot acquires a map of its environment and simultaneously localizes itself relative to the map. The SLAM problem has been widely addressed by many approaches proposed by researchers. Generally speaking, these methods can be classified into four paradigms: Kalman-filter-based, particle-filter-based, graph-based and visual SLAMs [7-9]. Furthermore, visual SLAMs can also be divided into three types; sparse, semi-dense and dense SLAM. For example, RGBD SLAM, one of the dense visual SLAM methods, can be done by using camera and odometry information generated from the mobile robot [10].

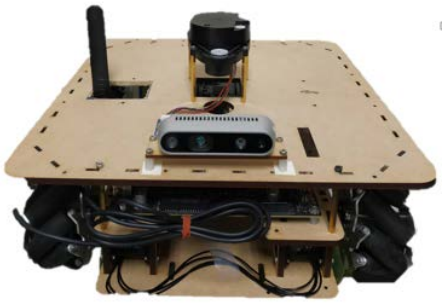

Figure 1. Mecanum-Wheeled Omnidirectional Mobile Robot.

The papers in [11-14] show the most important task of autonomous exploration for a mobile robot is to determine a desired motion position of the robot in the next step such that such a robot can obtain the most unknown and correct environmental information with the shortest collision-free path in the global scope.

Obviously, a successful SLAM technique is often accompanied with an exploration algorithm in [15-20]. Accordingly, the mapping of an unknown environment heavily relies on an efficient and effective exploration algorithm to build its environment map.

The definition of the feature is that no matter how you rotate the image or change the distance to the image, the features will still remain unchanged and these are called rotation invariance and scale invariance. There are various kinds of rotation-invariance and scale-invariance feature detection algorithms such as SIFT, SURF, ORB, HOG, LBP, and Harr. In this paper, SURF is selected as our feature detection algorithm to identify matched features on different maps.

The motivation of this paper is that the mobile robot in the unknown environment is unable to autonomous movement in the environment. Therefore, we need to three dimensional SLAM techniques and exploration algorithm in order to build a map of the unknown environment. Hence, the objectives of this paper is to develop an integrated mobile exploration system that has capability to autonomously explore unknown environment and build the 3D map via existing RGB-D SLAM technique, thus enabling a mobile robot to have autonomous navigation in any indoor environment.

Po-An Wei, Ching-Chih Tsai and Feng-Chun Tai are with the Department of Electrical Engineering, National Chung Hsing University, Taichung 40227, Taiwan. (Corresponding author Ching-Chih Tsai, email: cctsai@nchu.edu.tw) (email: g106064501@mail.nchu.edu.tw, fctai@nchu.edu.tw)

The authors gratefully acknowledge financial support from the Ministry of Science and Technology, Taiwan, the R.O.C., under contract MOST 107-2221-E-005 -073-MY2.

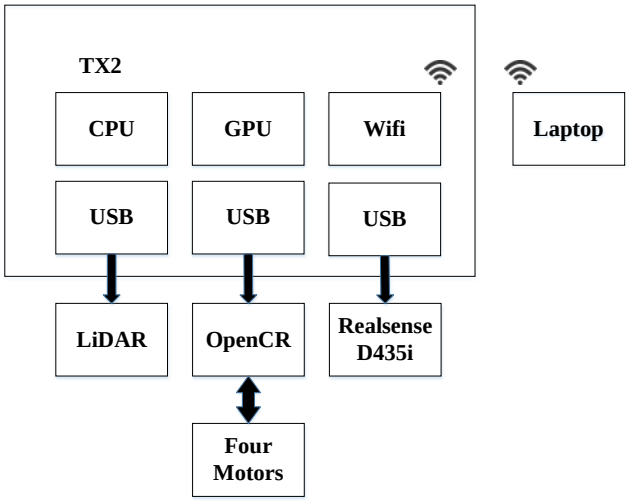

Figure 2. Major components and signal flow of the experimental MWOR.

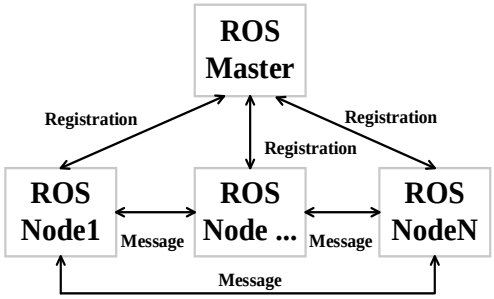

Figure 3. ROS framework.

The rest of the paper is organized as follows. Section II describes the proposed system architecture equipped with appropriate hardware and software. Section III provides the detailed descriptions of the used RGB-D SLAM. In Section IV, a complete coverage exploration algorithm is proposed to achieve exploration goal. In Section V, simulation show the effectiveness of the proposed method with the RGB-D SLAM. Experiment results are conducted in Section VI. Finally, Section VII concludes this paper.

II. System Architecture

This section aims to introduce the system architecture of the experimental robot in the following three subsections. One is the illustration of the used robot, the other is the description of the established software system composed of the ROS framework, and another is the workflow of our robots' exploration. Below are the detailed descriptions of the three main ideas.

A. Hardware Devices

As shown in Fig. 1, the used MWOR works as main experimental platform for testing the proposed exploration and SLAM method. The experimental MWOR is equipped with Linux (Ubuntu 16.04) carried out by the onboard TX2. This MWOR based on the ROS (Robot Operating System), middleware enables to be equipped with one RealSense D435i for sensing landmarks in the environment. The information of landmarks is then transferred to the laptop computer through WiFi. OpenCR1.0 control board is employed to calculate kinematics and odometry for the used MWOR. The TX2 computing module is employed to obtain odometry information of the robot through USB connect and pass it to the laptop. Exploration algorithm will also be delivered to the robot from the laptop through TX2. The overview structure of our hardware devices is shown in Fig.2. The system configuration of the MWOR as shown in Fig.4.

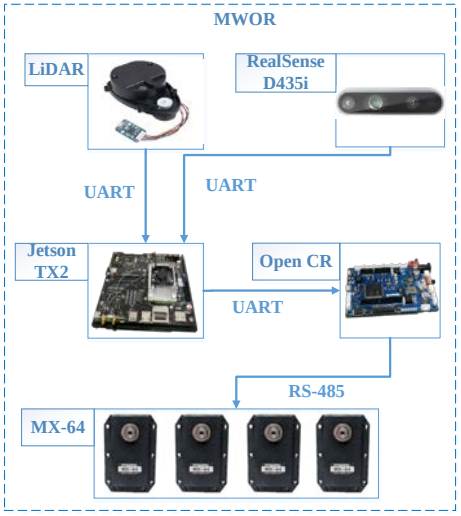

Figure 4. System configuration of MWOR.

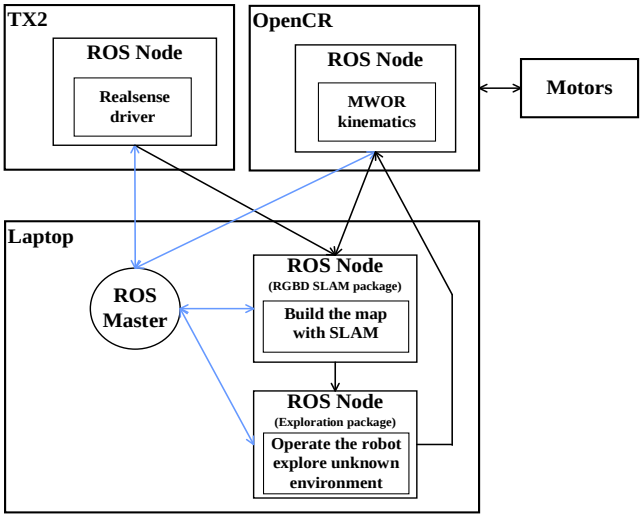

Figure 5. Connection of the overall robotic software using ROS.

B. Software Structure

The basic structure of our robot control system is based on ROS. ROS starts with the ROS Master. After all other ROS pieces of software (Nodes) registers under the ROS master, all ROS nodes are able to find and talk to each other via ROS message type including Topic, Service, and Actionlib, as shown in Fig 3. The laptop is used to run the ROS Master to monitor condition of the WMOR. After the robot acquires the information from the environment, it will be sent to the laptop to make further processing and utilization.

Fig. 5 depicts the connection of the overall robotic software using the ROS. ROS is mainly based on Ubuntu operating system. The ROS Master is opened in the laptop. All the required ROS Nodes will be registered under the ROS Master. Messages between ROS Nodes are transmitted through ROS Topic. After the host computer gets the LiDAR scanning data and odometry from TX2, it will start to execute RGB-D SLAM algorithm to build the map of the environment, and the exploration algorithm for the robot to explore unknown environment.

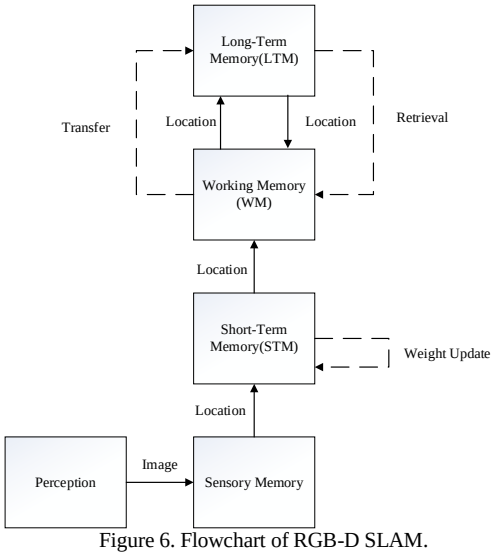

Figure 6. Flowchart of RGB-D SLAM.

III. RGB-D SLAM

This section is devoted to analysis and implementation of the proposed RGB-D SLAM. The flowchart of RGB-D SLAM is shown in Fig.6. The first part will illustrate RGB-D SLAM algorithm. The second part elucidates the exploration algorithm.

A. SLAM

SLAM is a technique of estimating robot trajectory $s^t=s_1,\ldots,s_t$, and the map $\Theta=\theta_1,\ldots,\theta_N$ given the observation z^t, motion u^t and data association variables, $n_t=n_1,\ldots,n_t$, which specifies the identity of the landmark observed at time *t*.

B. Location Creation

Using OpenCV, speeded-up robust features (SURF) are extracted from the images to derive visual words. Each visual word of the vocabulary refers to a single SURF feature's descriptor. Every SURF feature has a strength referred to as feature response. The feature response is used to choose the most prominent features in the image.

C. Weight Updating

To update the weight of the acquired location, is compared with the last one in STM, and similarity degree is evaluated by using

$$s(z_t, z_c) = \begin{cases} N_{pair} / N_{Z_t}, & if\ N_{Z_t} \geq N_{Z_c} \\ N_{pair} / N_{Z_C}, & if\ N_{z_t} < N_{Z_c} \end{cases} \quad (1)$$

where N_{pair} is the number of matched word pairs between the compared location signatures, and N_{Z_t} and N_{Z_c} are the total number of words of signature Z_t and the compared signature Z_c, respectively.

D. Bayesian Filter Updating

The role of the discrete Bayesian filter is to keep track of loop-closure hypotheses by estimating the probability that the current location matches one of an already visited location stored in the working memory (WM).The time index that is associated with the newest location in working memory (WM), expressed as follows

TABLE I
THE PSEUDO CODE OF LOCATION CREATION PROCEDURE.

1. **Algorithm create location L with image I**
2. **Procedure** LOCATIONCREATION(I)
3. $f \leftarrow$ detect a maximum of $T_{\max\ Features}$ SURF features from image I with SURF features response over $T_{response}$.
4. $d \leftarrow$ extract SURF descriptors from I with features f.
5. Prepare nearest-neighbor index.
6. $z \leftarrow$ quantize descriptors d to vocabulary
7. $L \leftarrow$ create location with signature z and weight 0
8. **return** L
9. end procedure

TABLE II
THE PSEUDO CODE OF RETRIEVAL

1. **Retrieve neighbors of L from LTM to WM**
2. **Procedure** RETRIEVAL(L)
3. $L_r \leftarrow$ load a maximum of two neighbor of L from LTM.
4. Add reference to L_r for words in z_r still in vocabulary.
5. Match old words of z_r to current ones in vocabulary.
6. Not matched old world of z_r are added to vocabulary.
7. Insert L_r into WM
8. end procedure

$$p(S_t \mid L^t) = \eta\, p(\mathrm{Lt} \mid \mathrm{S}_t) \sum_{i=-1}^{t_n} p(S_t \mid S_{t-1} = i)\, p(S_{t-1} = i \mid L^{t-1}) \quad (2)$$

E. Loop-Closure Hypothesis Selection

When $p(S_t|L^t)$ has been updated and normalized, the highest loop-closure hypothesis $S_t=i$ of $p(S_t|L^t)$ is accepted if the new location hypothesis $p(S_t=-1|L^t)$ is lower than the loop-closure threshold T_{loop} (set between 0 and 1).When a loop-closure hypothesis is accepted, L_t is linked with the old location L_t: the weight of L_t is increased by the one of L_t, the weight of L_t is reset to 0, and a loop-closure link is added between L_t and L_t. The loop-closure link is used to get neighbors of the old location during retrieval and to set up the transition model of the Bayes filter.

F. Retrieval

After loop-closure detection, neighbors not in WM of the location with the highest loop-closure hypothesis are transferred back from long-term memory (LTM) to WM. In this paper, LTM is implemented as a SQLite3 database in Table 2. In Table 2, the link type tells if it is a neighbor link or a loop-closure link.

When locations are retrieved from LTM, the visual vocabulary is updated with the words that are associated with the corresponding retrieved signatures. Common words from the retrieved signatures still exist in the vocabulary; therefore, a reference is added between these words and the corresponding signatures.

TABLE III
THE PSEUDO CODE OF RRT

```
Algorithm BuildRRT
 Input: Initial configuration qinit, number of vertices in RRT K,
    incremental distance Δq)
 Output: RRT graph G
 G.init(qinit)
 for k = 1 to K
  qrand ← RAND_CONF()
  qnear ← NEAREST_VERTEX(qrand, G)
  qnew ← NEW_CONF(qnear, qrand, Δq)
  G.add_vertex(qnew)
  G.add_edge(qnear, qnew)
 return G
```

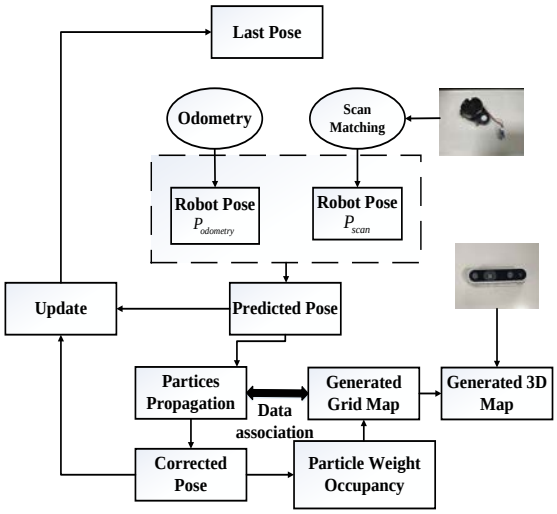

Figure 7. Flowchart of Cooperative 3D SLAM.

G.Transferring

When processing time for an image is greater than, the oldest locations of the lowest weighted ones are transferred from working memory (WM) to long-term memory (LTM). To be able to evaluate appropriately loop-closure hypotheses using the discrete Bayesian filter, neighbors of the highest loop-closure hypothesis are not allowed to be transferred.

IV. COOPERATIVE 3D SLAM

This part will use the Rao-Blackwellized Particle Filters (RBPF) to complete SLAM in an indoor scenery, and merge measured data taken from the LiDAR and Intel RealSense D435i, which are exploited to respectively build 2D and 3D maps. The main flow chart of this work is shown in Figure 3.4. The pose estimation and mapping of the indoor environment involves two steps, which are prediction step and correction step. In the prediction step, the RBPF is utilized to fuse the measurements of the odometry and matching data from the LiDAR and Intel RealSense D435i camera, in order to construct a cooperative 3D map. In the correction step, the particle filters algorithm is then used to relocate the robot pose so as to update the cooperative 3D map. Fig.7 describes flowchart of Cooperative 3D SLAM.

TABLE IV
THE PSEUDO CODE OF IMPROVED RRT

```
Algorithm BuildRRT
 Input: Initial configuration qinit, number of vertices in RRT K,
    incremental distance Δq)
 Output: RRT graph G
D. init(qinit)
qrand, qnear, qnew ← ϕ ;
1.for k = 1 to K
2. qrand ← RAND_CONF()
3.qnear ← NEAREST_VERTEX(qrand, G)
4.qnew ← NEW_CONF(qnear, qrand, Δq)
5. Collision detection for qnew to qnear
6. If there is no collision
5.G.add_vertex(qnew)
6.G.add_edge(qnear, qnew)
7. If qnew=qgoal or qnew and qnear will be surrounded by qgoal
8. path←fillSolutionPath(edges,vertices);
9. endif
10. endfor
11.pathSmooth ←smooth(map , qnear, qnew ,path)
 return G
```

V.IMPROVED EXPLORATION ALGORITHM

In the unknown environment, the mobile robot needs to find a complete-coverage way to exploration environment. Therefore, we use a rapidly exploring random tree (RRT), which is an algorithm designed to efficiently search nonconvex, high-dimensional spaces by randomly building a space-filling tree. The tree is constructed incrementally from samples drawn randomly from the search space and is inherently biased to grow towards explore unknown. The MWOR based on the RRT exploration algorithm to build environment map.

Due of the randomness of RRT sampling, the result of path has many redundant nodes, which increases the length of the path. Therefore, intuitive idea deletes redundant nodes. Calculate the distance between each node, and using the triangle inequality. The replaced path is shorter and the intermediate redundant nodes can be cropped. Using this modified method, it makes the path smoothly and also make the mobile robot reduce time to explore of environment.

VI. SIMULATION AND DISCUSSION

This section aims to verify the proposed improved RRT exploration algorithm by conducting experiments on the experimental MWOR. Fig.8(a) illustrates the unknown environment. Fig.8(b) shows the exploration path obtained from the conenetional RRT algorithm, and Fig.8(c) shows the exploration path found by the improved RRT algorithm. As can be seen in Fig.8(b) and Fig.8(c), it is obvious that the exploration path in Fig.8(c) is more smooth than that in Fig.8(b), thus showing that the improved RRT is capable of find a more mooth path.

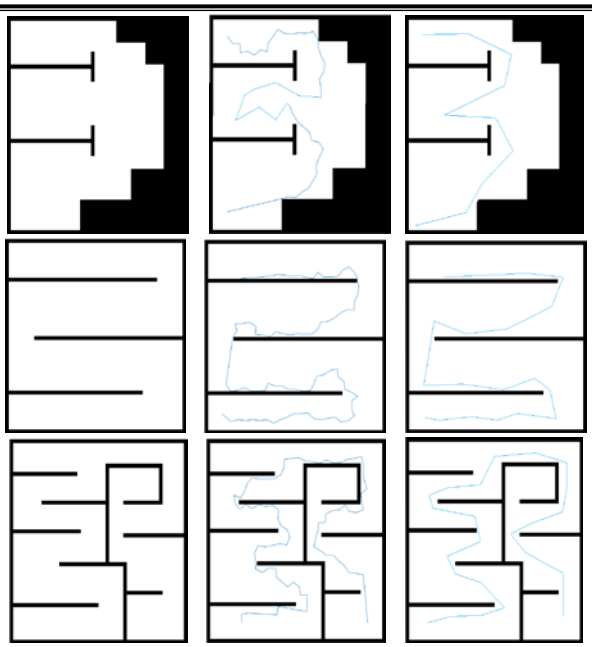

(a) (b) (c)

Figure 8. (a) Unknown environment. (b) Exploration path obtained from the original RRT algorithm. (c) Exploration path obtained from the improved RRT algorithm.

VII. Experiment and Discussion

This section aims to present experimental results of the RGB-D SLAM with the improved RRT exploration algorithm for the MWOR. Fig. 9 shows the experiment process of using improved RRT exploration algorithm. Using improved RRT exploration algorithm can reduce time of exploration. Fig.10. shows the built 3D map of the proposed RGB-D SLAM with the improved RRT algorithm, (a) Top view. (b) Side view. Fig.11. depicts the fusion of 2D and 3D maps by the cooperative 3D SLAM method.

VIII. Conclusions and Future Work

In this paper, an RGB-D SLAM along with an improved RRT exploration method has been proposed to achieve 3D SLAM for a Mecanum-wheeled omnidirectional mobile robot (MWOR). With the ROS system. The MWOR has used the improved RRT exploration algorithm to explore unknown environment, and exploited the well-known RGB-D SLAM algorithm to build the 3D map of the experimental environment at the same time. In the future work, it would be to refine the exploration strategy and use multiple mobile robots to cooperate explore and build unknown environments by their 3D maps.

Figure 9. Experiment process of using improved RRT exploration algorithm.

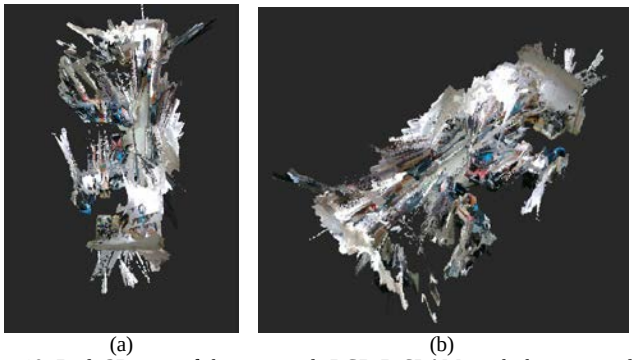

(a) (b)

Figure 10. Built 3D map of the proposed RGB-D SLAM with the improved RRT algorithm, (a) Top view. (b) Side view.

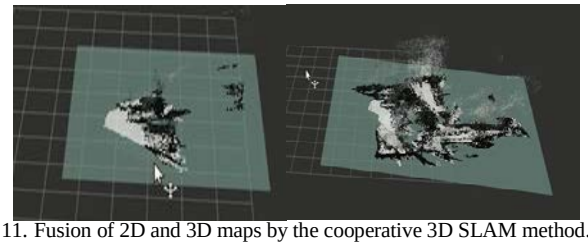

Figure 11. Fusion of 2D and 3D maps by the cooperative 3D SLAM method.

References

[1] ROS, [Online]. Retrieved May 20, 2019, from http://www.ros.org/

[2] ROS 101: Introduction to the robot operating system, [Online]. Retrieved May 20, 2019,from http://robohub.org/ros-101-intro-to-the-robot-operating-system/

[3] ROS navigation stack, [Online]. Retrieved March 10, 2019, from http://wiki.ros.org/ navigation/Tutorials/RobotSetup#Robot_Setup.

[4] F. Hashikawa and K. Morioka, "Mobile robot navigation based on interactive SLAM with an intelligent space," in *Proc. of* 2011 8th International Conference on Ubiquitous Robots and Ambient Intelligence (URAI), Incheon, 2011, pp. 788-789.

[5] X. Wang, Z. Yao, and Z. Yang, "The use of object tracking in visual SLAM," in *Proc. of 2017 International Conference on Applied System Innovation (ICASI)*, Sapporo, 2017, pp. 850-853.

[6] S. Chan, P. Wu, and L. Fu, "Robust 2D indoor localization through Laser SLAM and visual SLAM fusion," in *Proc. of 2018 IEEE International Conference on Systems, Man, and Cybernetics (SMC)*, Miyazaki, Japan, 2018, pp. 1263-1268.

[7] M. Liu and H. Leung, "EM-EKF based visual SLAM for simple robot localization," in *Proc. of 2014 IEEE International Conference on Systems, Man, and Cybernetics (SMC)*, San Diego, CA, 2014, pp. 3121-3125.

[8] A. Kasyanov, F. Engelmann, J. Stückler and B. Leibe, "Keyframe-based visual-inertial online SLAM with relocalization," in *Proc. of* 2017 IEEE/RSJ International Conference on Intelligent Robots and Systems (IROS), Vancouver, BC, 2017, pp. 6662-6669.

[9] L. Yaojun, P. Quan, Z. Chunhui and Y. Feng, "Scene matching based EKF-SLAM visual navigation," in *Proc. of the 31st Chinese Control Conference*, Hefei, 2012, pp. 5094-5099.
[10] A. Eudes, M. Lhuillier, S. Naudet-Collette and M. Dhome, "Fast odometry integration in local bundle adjustment-based visual SLAM," in *Proc. of 2010 20th International Conference on Pattern Recognition*, Istanbul, 2010, pp. 290-293.
[11] W. Fink et al., "Robotic lake lander test bed for autonomous surface and subsurface exploration of Titan lakes," in *Proc. of* 2012 *IEEE Aerospace Conference*, Big Sky, MT, 2012, pp. 1-12.
[12] Z. Li, Y. Xiong and L. Zhou, "ROS-Based indoor autonomous exploration and navigation wheelchair," in *Proc. of* 2017 *10th International Symposium on Computational Intelligence and Design (ISCID)*, Hangzhou, 2017, pp. 132-135.
[13] J. N. Bakambu, "Integrated autonomous system for exploration and navigation in underground mines," in *Proc. of 2006 IEEE/RSJ International Conference on Intelligent Robots and Systems*, Beijing, 2006, pp. 2308-2313.
[14] E. Uslu, F. Çakmak, M. Balcılar, M. F. Amasyalı and S. Yavuz, "Frontier-based autonomous exploration algorithm implementation," in *Proc. of 2015 23nd Signal Processing and Communications Applications Conference (SIU)*, Malatya, 2015, pp. 1313-1316.
[15] S. S. Belavadi, R. Beri and V. Malik, "Frontier exploration technique for 3D autonomous SLAM Using K-Means based divisive clustering," in *Proc. of 2017 Asia Modelling Symposium (AMS)*, Kota Kinabalu, 2017, pp. 95-100.
[16] D. Priyasad et al., "Point cloud based autonomous area exploration algorithm," in *Proc. of 2018 Moratuwa Engineering Research Conference (MERCon)*, Moratuwa, 2018, pp. 318-323.
[17] S. Sinaei and O. Fatemi, "Tree-based algorithm for design space exploration and mapping application onto heterogeneous platforms," in *Proc. of* 2017 *19th International Symposium on Computer Architecture and Digital Systems (CADS)*, Kish Island, 2017, pp. 1-6.
[18] L. Yu and Z. Cai, "Robot Exploration Mission Planning Based on Heterogeneous Interactive Cultural Hybrid Algorithm," in *Proc. of 2009 Fifth International Conference on Natural Computation*, Tianjin, 2009, pp. 583-587.
[19] L. Caballero, C. Benavides and W. Percybrooks, "Machine learning-based system to estimate the performance of exploration algorithms for robots in a bi-dimensional grid," in *Proc. of 2017 IEEE 3rd Colombian Conference on Automatic Control (CCAC)*, Cartagena, 2017, pp. 1-6.
[20] L. Qiyun and T. Qi, "Exploration of regional economic development gap and coordinated development path in inner mongolia area dependent on the extended Dijstra algorithm," in *Proc. of 2019 International Conference on Intelligent Transportation, Big Data & Smart City (ICITBS)*, Changsha, China, 2019, pp. 259-263.

Po-An Wei he is currently pursuing Master's degree in Department of Electrical Engineering from National Chung Hsing University, Taichung, Taiwan, ROC. His current research interests include Mecanum robot, exploration, cooperative 3D SLAM and their applications for the robot autonomous navigation.

Ching-Chih Tsai received the Diplomat in Electrical Engineering from National Taipei Institute of Technology, Taipei, Taiwan, ROC, the MS degree in Control Engineering from National Chiao Tung University, Hsinchu, Taiwan, ROC and the Ph.D degree in Electrical Engineering from Northwestern University, Evanston, IL, USA, in 1981, 1986 and 1991, respectively. Currently, he is currently a Distinguished Professor in the Department of Electrical Engineering, National Chung-Hsing University, Taichung, Taiwan, where he served the Chairman in the Department of Electrical Engineering from 2012 to 2014. He is a Fellow of IEEE, IET and CACS.

Dr. Tsai served as the Chair, Taipei Chapter, IEEE Control Systems Society, from 2000 to 2003, and the Chair, Taipei Chapter, IEEE Robotics and Automation Society from 2005 to 2006. In 2007, he was the program chair of 2007 CACS international automatic conference sponsored by Taipei chapter, IEEE control systems society. In 2010, he served as the program co-chair of SICE 2010 annual conference in Taiwan, which was technically sponsored by IEEE CSS; in 2011, he served as the General Chair, 2011 International conference on service and interactive robotics; in 2012, he has served as the General Chair, 2012 International conference on Fuzzy Theory and Its Applications, the General Chair, 2012-2015 CACS International Automatic Control Conferences, and the General Chair, 2016-2017 International Conference on Advanced Robotics and Intelligent Systems. Dr. Tsai served the two-term President, Chinese Institute of Engineers in Central Taiwan, Taiwan from 2007 to 2011, and two-term President of Chinese Automatic Control Society from 2012 to 2015. Since 2008, he has been the Executive Directors in Boards of Government of thee professional associations, including Robotic Society of Taiwan, Taiwan Fuzzy Systems Association, and Taiwan Systems Association. He has served as the Chair, Taichung Chapter, IEEE Systems, Man, and Cybernetics Society since 2009, the Chair of IEEE SMC Technical Committee on intelligent learning in control systems since 2009, the President of Robotics Society of Taiwan since 2016, the steering committee of Asian Control Association since 2014, a BOG member of IEEE Nanotechnology council since 2012, the Vice President of International Fuzzy Systems Association since 2015, and a BOG member of the IEEE SMCS since 2017.

Dr. Tsai has published more than 500 technical papers, and seven patents in the fields of control theory, systems technology and applications. Web of Science has indexed his paper entitled "Adaptive Neural Network Control of a Self-Balancing Two-Wheeled Scooter" in the category Automation Control Systems, where the paper was ranked 408 out of 37607 articles (published between 2010 to 2014). Dr. Tsai is respectively the recipients of the Third Society Prize Paper Award from IEEE Industry Application Society in 1998, the Outstanding Automatic Control Engineering Award in 2008 from Chinese Automatic Control Society (CACS), and the Outstanding Engineering Professor Award in 2009 from the Chinese Institute of Engineers in 2009, the IEEE Most Active SMC Technical Committee (TC) Award in 2012 from IEEE SMC Society, the Outstanding Electrical Engineering Professor Award from the Chinese Institute of Electrical Engineering in 2014, Outstanding Industry Contribution Award from Taiwan Systems Association in 2016, the best paper award in the International Journal of Fuzzy Systems in 2017, and many best paper awards from many international conferences technically supported by IEEE. He is the advisor, IEEE SMC student branch chapter at National Chung Hsing University; this chapter was the recipient of certificate of appreciation from IEEE SMCS in 2009. He has served as the associate editors of International Journal of Fuzzy Systems, and IEEE Transactions on Systems, Man and Cybernetics: Systems, IEEE Transactions on Industry Informatics, and International Journal of Electrical Engineering. Recently, he has served as the Editor-in-Chief of a new international robotics journal called “iRobotics”. His current interests include advanced nonlinear control methods, deep model predictive control, fuzzy control, neural-network control, advanced mobile robotics, intelligent service robotics, intelligent mechatronics, intelligent learning control methods with their applications to industrial processes and intelligent machinery.

Feng-Chun Tai received the B.S., M.S. and Ph.D. degrees in Department of Electrical Engineering from National Chung Hsing University, Taichung, Taiwan, ROC. in 2007, 2010 and 2018, respectively. His current research interests include mobile robots, intelligent control, navigation system and their applications to industrial processes and machines.

Powered Mobility and Feeding Assistive Robots - a Review

Salman Masroor, Xiang-Min Tu, Bahrudin, and Chyi-Yeu Lin

***Abstract*—During the past few decades, support in the daily activities of disabled and elderly community has become a serious global problem. The rapid growth of people with disabilities in society requires caregivers to facilitate them in their day-to-day activities. Healthcare services especially caregiving, is very costly and includes high risk of injuries. Mobility aids are a key tool for moving the disabled person, which empower the disabled to be moved and decrease the injury risk for both disabled and the caregiver, mainly in the bedroom and bathroom. Accessibility to food is another problem faced by these people at home. Therefore, feeding robots are of significant importance towards assisting these persons. Most assistive systems require a certain level of human assistance, but these devices of fully autonomous operational capability have not been established previously. The paper provides a study of assisted mobility aids used in homes and hospitals and assistive devices.**

***Index Terms*—Powered Mobility Assistive, Transfer Devices, Physically Disabled People, Feed assistive robots.**

I. Introduction

DURING the past few decades, support in the daily activities of the elderly and aging community has become a serious global problem. Statistics show that around 15% of the world's population is dealing with different sort of impairment and disabilities [1]. The American Community Survey classifies disability as related to hearing, vision, cognitive, self-care, independent living or ambulatory (mobility). For the United States, the survey observes that the most dominant type of disability is ambulatory disability, which accounts for about 6.5% of all disabilities. Categorizing ambulatory disability in United States by age, it affects only 5.1% of people aged 18 to 64 years but 22.5% of people aged 65 years or over. Thus, as the population ages, people's mobility decreases [2]. Between 1975 and 2015, the number of Americans aged 65 or older has more than doubled from 22.6 million to 47.8 million, and by 2030, one in five Americans are expected to be 65 or older. [3].

Japan and Taiwan are also facing super-aging issues. Elderly people percentage, in japan for the year 2016, has been recorded as 27.3%, besides in 2050 it is projected to be 37.7% [4]. Comparing the physically disabled community with overall disabled population it is about 5.9% [5], table 1, shows world top ten countries having largest share of people aged 60 years or above [6]. Similarly, for Taiwan, the aged population, is

Salman Masroor, Xiang-Min Tu, Bahrudin, and Chyi-Yeu Lin are with the Department of Electrical Engineering, National Taiwan University of Science and Technology, Taipei City 10607, Taiwan (R.O.C.)
(Corresponding author: Chyi-Yeu Lin, email: jerrylin@mail.ntust.edu.tw)
(email: D10603826@mail.ntust.edu.tw)

The authors gratefully acknowledge financial support from the Ministry of Science and Technology, Taiwan, the R.O.C., under contract MOST 107-2221-E-005 -073-MY2.

TABLE I
WORLD TOP TEN COUNTRIES HAVING LARGEST SHARE OF PEOPLE AGED 60 YEARS OR ABOVE [6]

	1980		2017		2050	
Rank	Country or area	Percentage aged 60 years or over	Country or area	Percentage aged 60 years or over	Country or area	Percentage aged 60 years or over
1	Sweden	22.0	Japan	33.4	Japan	42.4
2	Norway	20.2	Italy	29.4	Spain	41.9
3	Channel Islands	20.1	Germany	28.0	Portugal	41.7
4	United Kingdom	20.0	Portugal	27.9	Greece	41.6
5	Denmark	19.5	Finland	27.8	Republic of Korea	41.6
6	Germany	19.3	Bulgaria	27.7	China, Taiwan Province of China	41.3
7	Austria	19.0	Croatia	26.8	China, Hong Kong SAR	40.6
8	Belgium	18.4	Greece	26.5	Italy	40.3
9	Switzerland	18.2	Slovenia	26.3	Singapore	40.1
10	Luxembourg	17.8	Latvia	26.2	Poland	39.5

documented as 14.7% in 2018 and by 2026 it is projected to be aged society [7] , On the other hand, in 2016, the elderly population was over 0.7 million. [8].

The fast-growing number of disabilities as well as elderly people in the world, demands caregivers ' dedication to assist in conducting daily activities. However, cost of caregiving and injury rates are extremely high. Besides expenses of caregiving, family and close friends also provide informal support, which is an enormous undiscovered expense. For example, this informal care is estimated to be USD 522 billion per year in the United States and is determined by measuring the revenue lost by unpaid caregivers during their time in the care of the elderly [9].The papers in [11-14] show the most important task of autonomous exploration for a mobile robot is to determine a desired motion position of the robot in the next step such that such a robot can obtain the most unknown and correct environmental information with the shortest collision-free path in the global scope.

Rapidly increasing population of elderly and disabled demands an improved level of health care and living assistance compared previously. Global issues of aging and disability have contributed to a decline in operational capacity and autonomy people. Therefore, the current focus of both the scientific community and the industry are the growing demands for healthcare and strategy formulation so that a shift in paradigm in the field of assistive technology could be achieved.

The paper presents a comparative evaluation of reality and ideality in the life of a disabled and aged person (Section 2). Domestically and commercially used Powered mobility assistive devices (see Section 3). Further, The devices to assist them for the purpose of feeding (Section 4).

II. A Daily Life and Limitation: Reality and Ideality

Daily life of a person includes performing activities of daily living (ADLs). Essentially recognized ADLs are the ability of the individual to feed, dress, move or shift independently from one place to another, bathe and toilet. Normal adults can perform ADLs independently, so they can lead a happy and

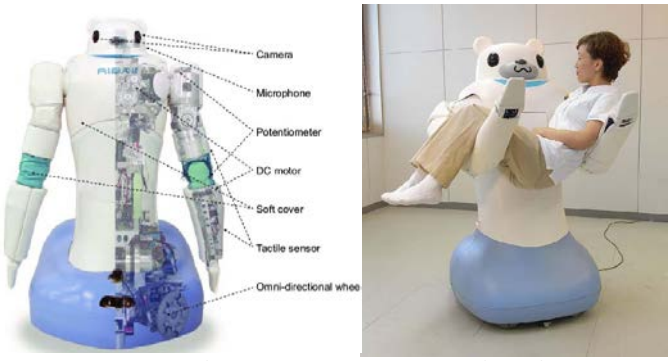

Figure 1. RIBA, Transfer assistant robot showing the lifting of human [15].

successful life without the need of caregiver. However, Inability to accomplish these ADLs results in an unsafe health conditions and deficient quality of life [10,11]. Caregiver (family or professional) give various form of healthcare support to the cared ones. According to some studies, these people needed assistance with at least one or usually four of the following tasks: dressing, bathing, brushing, eating, grooming, toileting and moving inside the home [12-13]. In terms of eating, personal hygiene, dressing, toileting, ambulating and maintaining medical habits, these people will rely entirely on caregivers. On the other hand, caregiving puts a financial, physical, and psychological burden on the person being cared. Research suggests that caregivers can risk their own health and well-being when supporting their loved ones. The practice of caregiving had led to poor health outcomes including poor sleep patterns, anxiety, depression and physical illness [14]. Thus, it can be inferred that the caregivers will ultimately become physically dependent in the future. To overcome this problem, a comprehensive solution is required that can assist a disabled and elderly people in performing activities of daily living.

III. Mobility Assistive Robots

Mobilizing the people, from one place to another having mobility limitation, becomes a tedious task for the caregiver and for the person being cared, because of the person's weight. It takes a great deal of effort and time to move the cared person from bed to wheelchair or wheelchair to bathroom and toilet and vice versa. Extended stay of cared ones in bed generates serious health problems for them, if proper health care and caregiving has not been provided.

Mobility assistive robots are essential equipment for mobilizing those people, who cannot transfer themselves independently. Based on lifting capability for transfer, notable mobility devices are RIBA (robot lifting a human) [15], home lift wheelchair by Position and Rehabilitation (HLPR) Chair [16], Intelligent sweet home concept (ISH) [17, 18]. However, some devices use wheeled and conveyor system capabilities to transfer the person, generally, they have integrated system of wheelchair and transfer modules, they are careful-patient mover(C-Pam) [19], multifunctional Test Bed [20], patient transfer system [21], conceptual design of a mechatronic system [22], robotic chair/ bed system for bedridden aged [23], and Panasonic Resyone [24,25].

A. RIBA (Robot Lifting a Human)

RIKEN-TRI Collaboration Center for Human-Interactive Robot Research developed RIBA (Robot lifting a human) transfer assistant robot [15]. Fig. 1 shows the RIBA robot lifting the human, it uses the human-like robotic arm for handling the disabled person, the robot lifting action is carried out similarly as humans do for transferring the person from bed and to wheelchair. The robotic arms have 7 degrees of freedom with a payload capacity of 63kg. RIBA is equipped with a camera, microphone and vast range of tactile sensors, these accessories assist RIBA to adjust the lifting trajectory and recognize the caregiver instructions so that the transfer process can be carried out safely. The maneuverability of the robot is achieved by an omnidirectional base.

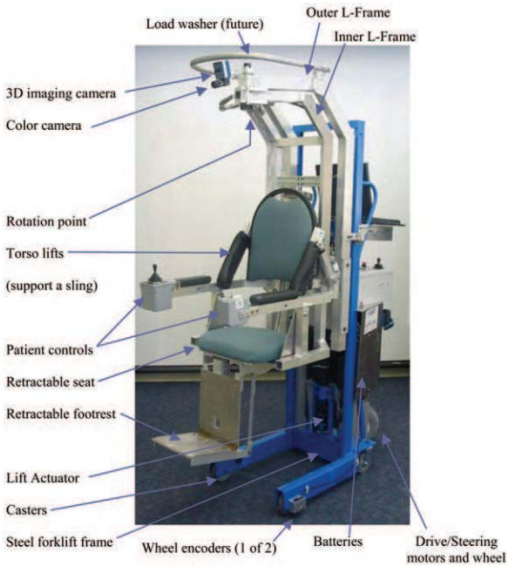

Figure 2. HLPR chair [16].

Although the interface of RIBA is user-friendly, there are some functional limitations. Lifting a disabled one, always involves the risk of slipping, due to which disabled people will not be comfortable while using RIBA. Secondly, it cannot lift the disabled person independently, it always requires assistance while lifting the disabled person. Additionally, it consumes electrical power for its operation, so obviously it is not suitable in the bathroom and toilets as there is the danger of electrical shock.

B. Home lift wheel chair by Position and Rehabilitation (HLPR) Chair

HLPR chair is another technological advancement in the field of assistive technology as it has focused on performing multiple tasks from the system [16]. It is designed in such a way that a single system can solve the issue of mobility, transfer, lift, and rehabilitation. Developed by the National Institute of Standards and Technology (NIST), USA, is shown in Fig. 2.

The design of the HLPR chair is based on a sturdy forklift. There are four main components of the HLPR chair, main and internal L-frame, retractable seat and footrest, height adjustment mechanism and drive module. Main L-frame is mounted on four casters to support the inner L-frame. The inner L-frame supports the retractable seat and footrest. Drive as well as steering module is placed on the backside of outer L-frame, so that caregiver can operate the chair.

The issues of mobilizing, lifting, rehabilitation and transferring were attempted to address through HLPR chair. Nevertheless, it is difficult to maneuver the machine and move

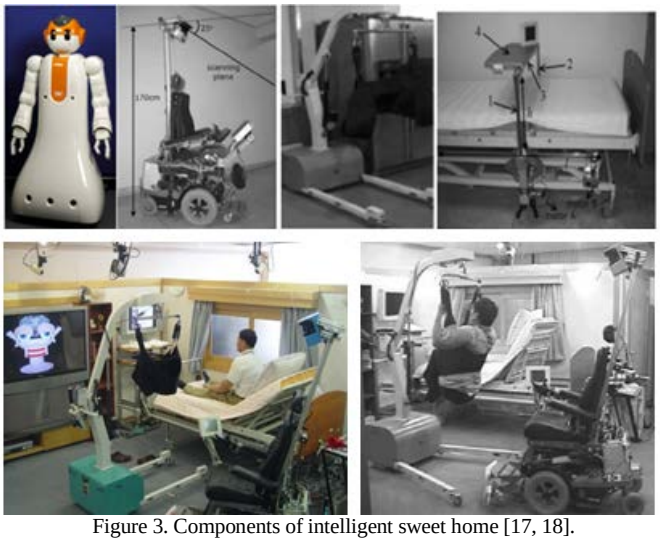

Figure 3. Components of intelligent sweet home [17, 18].

the user in the home environment due to the cumbersome and complicated design of the HLPR chair.

C. Intelligent sweet home concept (ISH)

Fig. 3, Shows the components of smart sweet home proposed to test the concept of disabled people's independent living [17, 18]. It comprises of intelligent bed robot, intelligent wheelchair, a transfer device, human-robot interface based on hand gesture and voice input and continuous health monitoring system.

Intelligent bed robot system has bed mattress with pressure sensor and a support manipulator. Pressure sensor provide the posture of the person whereas, support manipulator assists the person in changing the posture as well as getting off from the bed. In order to have access to different parts of home an autonomous wheelchair is also used. It is equipped with incremental encoders, a laser range finder and proximity sensor. A transfer device which can lift the person from the bed and place the disabled person on the wheelchair. A central control system controls and manages all devices through connectivity modules.

The intelligent robotic bed gets input through voice or hand gesture, when the person wishes to change the posture on the bed or transfer himself from bed to the intelligent wheelchair. The bed transforms according to the received command. The function of the robotic hoist lift is to lift and transfer the person to the wheelchair. So, after transformation hoist lift is brought near to the bed, the caregiver binds it to the person and then the user is lifted. Simultaneously, the automatic docking of the smart wheelchair with the bed takes place and then the lifted person is transferred in the wheelchair.

While the intelligent sweet home is completely integrated and automatic, caregivers' involvement is still needed that can attach the sling over the user's body. Apart from the involvement of caregivers, robotic hoist lifting is highly unsafe and uncomfortable.

D. Careful-patient mover(C-Pam)

Careful-patient mover, designed specifically for patient movement in the hospital [19]. Patients with disabilities can be moved from the bed to the stretcher or vice versa and can alleviate the patient's suffering, stress, and uncomfortable

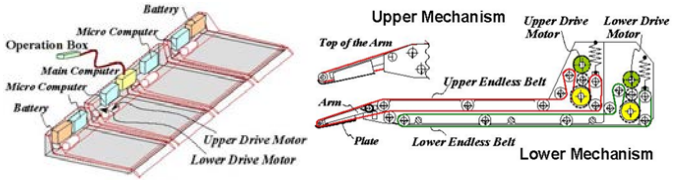

Figure 4. Mechanism of C-Pam [19].

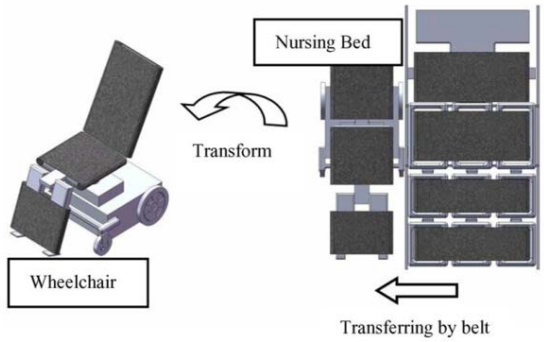

Figure 5. Schematic diagram of the design concept for demonstrating the body transfer [20].

feeling. Fig. 4. Shows the drive mechanism of the C-Pam system.

To transfer the patient from bed to stretcher, C-Pam moves across the bed from the stretcher and gently crawls under the patient, who is staying in bed. This motion is done by using the two motorized, endless conveyor belts. Then the C-Pam raises the patient gently and lowers him or her down to the stretcher.

Even though C-Pam is the novel technique of transferring the person but it is limited to bed to stretcher transfer only. Transfer from bed to wheelchair or toilet is not possible through this kind of device.

E. Multifunctional Test Bed

A novel model with a unique approach is developed to the transfer and posture change of bedridden people [20]. The system is a combination of two beds having different functionalities. A four-piece main bed was designed to change the disabled person's posture. By splitting a bed into four parts, the mattress provides more freedom to move shoulder, hip and waist, shown in Fig. 5.

The test bed is a combination of two robotic beds: a main bed and a nursing bed. The main bed is assigned to alter posture and transfer of person is done by the nursing bed. Both beds also have a belt system to move the body between them. For transfer both beds are operated and controlled by a systematically designed mechatronic device and can be interacted through a specially designed graphical user interface software.

Considering the fact that the concept of transferring the disabled person through this method is very convenient, however the system require a lot of adjustment while transfer because the system does not have the auto-docking capability so the caregiver should place the wheelchair at a very precise location, otherwise there is possibility of injury.

F. Patient transfer system (PTS) by NEXT HEALTH™

Patient Transfer System (PTS), created by Next Health, Inc. (Norwalk, CT), is an innovative transfer system designed to improve patient mobility and reduce the discomfort and injury-related risks faced by both patients and their assistants

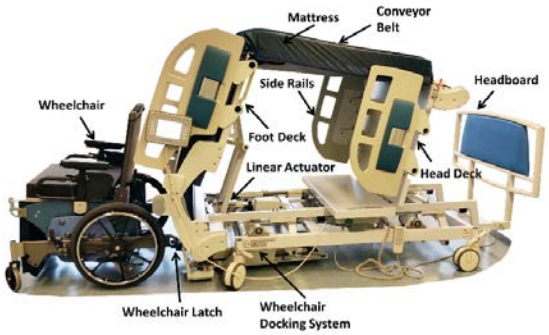

Figure 6. AgileLifeTM Patient Transfer System [21].

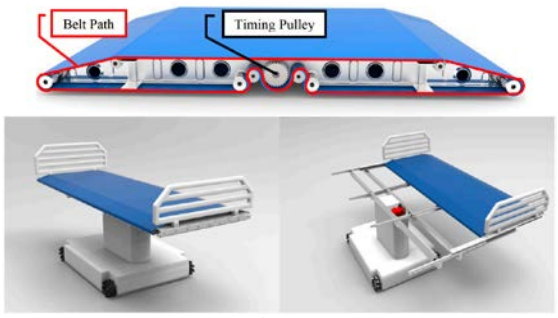

Figure 7. Mechatronic system for Bedridden Elderly Peoples [22].

(Fig. 6) [21]. This system also decreases the labor of caregivers by allowing no-lifting transfer device. care assistant just use a handheld pendent to operate the device. There are two main elements of PTS: a wheelchair and a conveyor system mounted on bed.

The wheelchair has interchangeable seat and a commode slot for direct bed-to-toilet and toilet-to-bed change, as well as tilt-in-space capabilities for redistributing pressure and preventing ulcers of pressure. The bed is designed as a standard hospital bed with controls for a comfortable position for patients.

For transferring the patient from wheelchair to the bed the caregiver brings the person sitting in the PTS wheelchair to a docking platform, placed at the foot of the bed. The wheelchair is reversed and a wheelchair bolt on the bed locks two pins on the back of the chair. The unit is activated once the wheelchair is docked to the floor of the bed. Using a series of linear actuators, gears and other parts, the bed's foot deck rises to meet the wheelchair's backrest. The caregiver drops the back of the seat so the patient's back comes in contact with the mattress. The wheelchair rotates at the same time as the foot deck is lowered, while the patient is slowly conveyed to bed by a conveyor belt.

G.Conceptual design of a mechatronic system

Fig. 7 shows, a mechatronic device inspired by industrial conveyors to assist caregivers while transferring and repositioning Bedridden Elderly Peoples (BEPs) in domestic environment [22]. Because of its low-profile structural properties, the proposed solution is capable of placing itself under the patient and recovering and reallocating the person on it.

Three conveyor modules are included in the proposed solution. Via two motors opposed to each other, each individual module drives a conveyer. The motors will drive two timing belts attached to the conveyor belt. Telescopic rails that are installed both sides of the system support the modules and allows bed-to-bed transition.

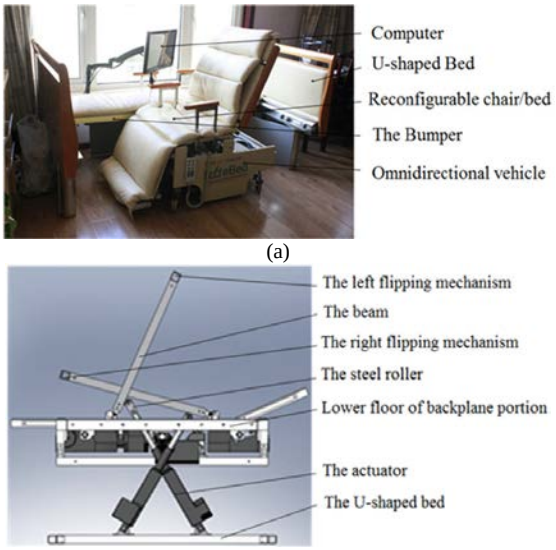

Figure 8. (a) The overview of the robotic chair/bed system (b) The flipping-body mechanism and the actuators [23].

Figure 9. Panasonic-Resyone, transformation from wheelchair to bed [24, 25].

H.Robotic chair/ bed system for bedridden aged

Robotic chair/bed is a combination of an omnidirectional, reconfigurable wheelchair, incorporated with a U-shaped bed as shown in Fig. 8 (a) [23]. It has been designed to facilitate specifically bedridden people. A repositioning device to avoid bedsores, is also fitted with it as shown in Fig. 8 (b). The wheelchair is also able to dock automatically. Linear and lateral movement is achieved by two separate assemblies mounted at the base of wheelchair's frame.

The requirement of additional system for shifting the person from the wheelchair to the bed and vice versa was eliminated by robotic chair / bed. Nonetheless, the system is intended to assist people with lower extremities and there will be a need for a continuous caregiver to transfer the patient from the wheelchair to the bathroom commode. In addition, the lateral movement is accomplished with the aid of a separate assembly, rendering the wheelchair hard to use.

I. Panasonic Resyone

Panasonic-Resyone is a hybrid wheelchair / bed robot combining a simple care bed with a complete reclining wheelchair as shown in Fig. 9 [24, 25]. A part of the bed can easily be turned into a wheelchair and vice versa without tedious tasks. Person can be moved to the wheelchair from bed, effortlessly without adjusting the posture of the disabled one. The physical exertion, done to transfer the person, previously was reduced substantially. Additionally the health and quality of life of caregiver as well as disabled one has been improved.

On the other side, for full reclining, the wheelchair system has a linear actuator, placed beneath the chair. For separating the wheelchair part and bed, caregiver has to do the lateral movement of wheelchair manually.

Figure 10. Hiwin - Healthcare Living [27].

Figure 11. Invacare - Bath lift [28].

IV. Assistive mobility for Bathroom & Toilet

The need for support and assistance is related to the stage of life, the environmental elements, the underlying health conditions, and the individual functioning level. Especially for the disabled and elderly, the important factors defining the necessity for aid are the availability and capability of relevant assistive devices, the presence of family members or assistants to aid, and the degree to which the society facilitates the environment for people with disabilities. When individuals with disabilities can independently get to a bathroom and toilet, they may not require another person to help them or just reduce the burden of an assistant. When they have an assistive device, they may be able to convey their local environment independently [26].

A. Assistive mobility for Bathroom

Fig. 10 [27] is an electrical assistive device designed by Hiwin Health Care. It can transfer a patient with full limb disability directly to the bathtub through a lifting device. The chair structure is entirely separate from the bathtub structure and It has a controller transfer mechanism driven by an electrical actuator. A portable seat is combined with a walk-in bathtub have designed by Invacare as shown in Fig. 11 [28]. Similar to the Hiwin product, the transfer structure is designed separately that enables the seat to go into walk in-tube in a sitting position. The seat is mounted on the mainframe which is standing outside the bathtub. The assistant just needs to push in the seat into the bathtub and adjust the position by a controller.

B. Assistive mobility for Bathroom

OnCare developed a reliable transfer patient device that integrates a commode and a lifter-seat wheelchair. The purpose is to transfer a patient that has leg-muscle limitation going to the toilet as shown in Fig. 12 [29]. The inclination movement is powered by an electrical linear actuator and there is a controller operated by an assistant.

Patient transfer assist has been developed by Takahashi et al. [30], and Toyota [31, 32] to reduce the heavy physical burden

Figure 12. OnCare – Powered lift seat [29].

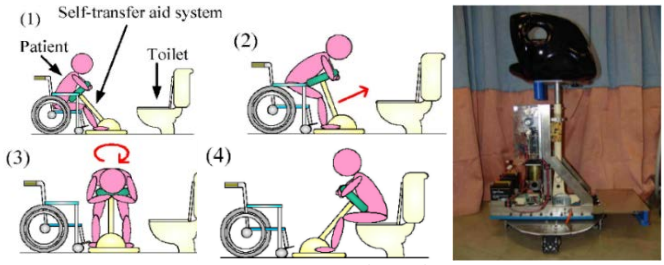

Figure 13. Takahashi - Self-transfer aid [30].

Figure 14. Toyota - Patient Transfer Assist [31, 32].

Figure 15. Melvin - Self-undressing toilet [33, 34].

required for an assistant when transferring patients to the toilet as shown in Fig. 13 and Fig. 14 respectively. Fig. 13 shows the method to transfer a person by lift the body mass weight by the upper structure and the main structure rotates to the toilet then puts down the patient on the commode. Similarly, the Toyota patient transfer assist also has a body support structure on the prone position to sustenance the body mass, as well as a wheeled platform, which will move the person from a bed to a toilet. The upper part has several linear and circular motion mechanisms to grasping the patient in the bed and prop up the chest during the transfer process. For both schemes, there is a possibility of slipping out of the body's chest support and the transfer manner involves the body's chest is congested. An assistant still needs to take care of the overall process during transfer.

Fig. 15 [33] shows the self-undressing toilet for an arm-muscle limitation patient. The mechanism is handled by an electrical grasping mechanism to stretch and pull down the pants. There are two symmetry-mechanism arms that moving in the opposite direction and has a special shape that can hook the pants. The simple joystick controller is used and located on the tip of the armrest and this device doesn't require an assistant. While the complex mechanism operation prevents it from being practical.

Figure 16. Topmedi Co., Ltd - Mover transfer chair [35, 36].

Fig. 16 shows a popular manual assistive device produced by Topmedi Co., Ltd. that easy to pick up a mobility-impaired patient from bed to do toileting even in the toilet or just put a basin on the seat [35, 36]. An open-closed mechanism was used to enable grabbing the person from the bed instantly. There were two safety locking systems in the backside that prevent the seat to open. The assistant can stir the device by the handle on the front of the device.

V. Feeding Assistive Robots

Self-feeding or eating is one of the items in the Activities of Daily Living (ADL) [37]. The percentage of people who cannot eat independently are increasing and ultimately they require assistive feeding system. It is due to global aging problem and an increase in chronic health conditions.

Limb disorder, muscle weakening and aging has made self-feeding difficult due to partial or complete loss of limb motion controllability. Individuals especially with quadriplegia find it difficult or even impossible to self-feed as a result of complete paralysis below their necks. On the other hand, individuals with SCI level C6 [38] or limb disorder may find it difficult to feed themselves independently. due to partial paralysis of hands and arms, for example, food cannot be completely transferred from the food container to user's mouth without dropping out. This situation may very likely ill-affect patient's dignity and self-esteem, cause them to resist or resent eating, thereby resulting in malnutrition and disease progression.

Those individuals who cannot feed themselves usually need external assistance from someone else such as a family member or a professional care provider under medical institutions to facilitate their eating. However, in the fast-emergent aging society, it would be non-realistic to further rely on human assistance to feed patients who cannot help themselves.

Many kinds of self-feeding assistive devices such as specially designed utensils, manually operated eating systems [39] and forearm supports have been proposed to replace manpower and to provide a more efficient eating experience for patient who cannot properly hold on cutlery. However, in order to use manually operated eating systems and forearm supports, the disabled person still needs at least some firm partial control over their upper limbs, which often cause unexpected food-dropping accidents and affects the patient's comfortability. Therefore, electrically powered meal assistance robots with many kinds of human machine interfaces (HMI) and robotic arms or special mechanism have been introduced to overcome these problems.

Automatic feeding robots had been proposed since 1987. As shown in Fig. 17 (a), Handy1 was one of the self-feeding robots presented by Mile Topping in 1987 [40]. It was the first self-feeding robot with a robot arm. It was designed for an 11-year-old boy with cerebral palsy to eat unaided. When the

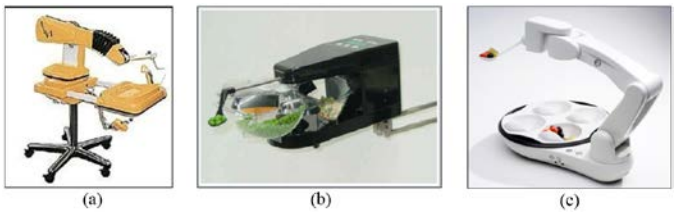

(a) (b) (c)

Figure 17. Assistive feeding robots: (a) Handy1 [40], (b) Mealtime Partner Dining System [41], (c) Obi [42].

(a) (b) (c)

Figure 18. More assistive feeding robots: (a) My Spoon [43], (b) Neater Eater Robot V6 [44], (c) iEAT [45].

moving LED comes close to the side of the food the boy wants to eat, he will need to select it with the joystick. After the selection, the food is transported by the robot arm to a standby point. The advantage was that the patient could have the meal aside the dining table or, in the bed. The main drawbacks include a huge robot arm and inefficient HMI system. As shown in Fig. 17 (b), Mealtime Partner Dining System [41], was presented in 2001. The Mealtime Partner Dining System could be installed on the desk and three rotatable food containers were mounted on holder, which is located in front of the user. Within the holder, there is an extendable spoon and limiting-device to control the amount of food to stay in the spoon before sent to the user. The user selects the food option by pushing the button when the container is under the spoon, the spoon will go down scoop a sizeable amount of food and extend to reach the mouth of the user. The main advantage of the Meal Time Partner Dining System was the food limit device, which will keep the proper amount of food to stay in the spoon and prevent food dropping during delivery motion. Furthermore, only two DOF are used in the mechanism. Drawbacks include and unstable structural system which shakes all the time, and the fast reaching spoon, which may incidentally hit the mouth or face, causing injuries.

As shown in Fig. 17 (c), Obi [42], is newly presented in 2018 by Jon Dekar. This robot is small, easy to fold and could operate it by simply pushing the buttons. The HMI system allows a user to choose the food within a section of a plate, and the edge of the section designed to trim the food while scooping it with a utensil. However, the main drawback was that the movement of the robot arm was pre-programmed and cannot adapt to the situations of the patient.

As shown in Fig. 18 (a), My Spoon is a chin-operated feeding robot with a spoon. The spoon coupled with a fork can grasp the food effectively, and the fork will retract automatically when the mouth of the patient contacts with the spoon [43]. The major disadvantage is the complexity involved in using the chin-operated joystick. As shown in Fig. 18 (b), Neater Eater Robot V6, in which food is stored and selected in a rotating walled-plate, allows the user to control the machine by a smartphone through Bluetooth system [44]. iEAT, as shown in Fig. 18 (c) has a simple mechanism of only three degrees of freedom and one-step food selection setup [45].

Although there were already a number of assistive self-feeding robots, there exist some major drawbacks. Most of the self-feeding robot requires complicated non-intuitive physical interaction from the user, for example, by pushing the buttons or finger/chin controlling the joystick to select the food on the serving container. The demand on these physical operations will prevent many patients from using it. Furthermore, the food-delivery trajectory of the feeding robots needs manual setup to fit to the height and position of the mouth of a given patient in front of the feeding device or the trajectory is even fixed without adjustability. Patients often experience inconvenience when receive food sent from these insensitive feeding devices. Most of these feeding robots cannot serve drinks or soups and many of them mix varied food together, causing an incomplete or inferior meal experience. In order to overcome all the problems, there is a need of an intelligent self-feeding robot, which can sense the mouth location of the patient and thus determine the proper food-delivery trajectory, watch or listen what the next food is selected without patient's physical operations, and can feed the patient with both solid and liquid food.

VI. Discussion

Continuously, rising disabled and elderly populations have become a global issue and assistive technologies are going to be highly beneficial in improving the quality of life for people with limited mobility. The literature suggests that in the past, research has focused on people with lower extremity disability and caregivers are constantly needed to assist these people. These people have to depend on caregivers ' services while using assistive technology systems. However a system capable of handling a completely impaired person has not been developed. Nonetheless, previously developed devices contain some risk factors and restrictions, which implies caregivers and clinicians must be involved with these individuals on an ongoing basis. Hence, the solution for this dilemma is a fully integrated intelligent home for the elderly where they can safely perform daily living activities independently. In that home, there should be a smart bed equipped with wheeled mobility system, smart toilets and intelligent feeding robot that can be used by these people to live a normal life.

Contrary to intelligent sweet home, a secure transfer mechanism in smart toilet would allow people to bathe and do toileting independently. Additionally, the fully autonomous smart bathroom would help reduce the caregivers ' physical burden.

The purpose of a feeding robot is to help limb disabled and aged people improve their accessibility to food and reduce the discomfort they face while dining. On the other hand, it can also be expected to reduce continuous involvement of caregivers.

VII. Conclusion

The paper provides a review of the systems used at home for the elderly and disabled. Assistive technology systems, is an emerging area of research, where engineers working with nurses and physiotherapists are trying to develop tools that can meet the needs of disabled people. Scientists have developed many tools to assist these people at home, but following their limitations, they are unable to meet end-user needs.

The factors that restrict the use of assistive technology are operational complexity, risk of slipping or falling, lack of maneuverability in tight spaces and cost. Although, numerous assistive devices have been invented and developed, they all require some degree of manual operation and assistance. However, systems with fully autonomous operating capability have not been developed. Until then, without a caregiver's intervention, a person with partial to full limb mobility disorder would not be able to perform daily living activities independently.

Therefore, the ultimate goal of future research is to create a human-centered, secure and intelligent support system that can be used to benefit people with physical disabilities at home. Such attributes will reduce the level of anxiety and depression and also improve the quality of life. A smart home is a comprehensive solution to fulfill the above tasks, where you can live with high self-esteem and boost your quality of life.

References

[1] United Nations, Department of Economic and Social Affairs, Population Division. World Population Prospects: The 2017 Revision, Key Findings and Advance Tables. Working Paper No. ESA/P/WP/248, 2017.
[2] Kraus, et al. "2017 Disability Statistics Annual Report," Durham, NH: University of New Hampshire, pp. 11-13, 2018.
[3] National Center for Health Statistics. Health, United States, 2016: With Chartbook on Long-term Trends in Health. Hyattsville, MD., 2017.
[4] Statistical Handbook of Japan, pp. 13, 2017.
[5] Disability in Japan: Overview and Statistics, available at https://www.disabled-world.com/news/asia/japan.php (last visited: 2019-12).
[6] United Nations, Department of Economic and Social Affairs, Population Division. World Population Ageing 2017 - Highlights (ST/ESA/SER.A/397), 2017.
[7] Taiwan Health and welfare report 2017, pp. 12, 2017.
[8] Population Projections for the R.O.C. (Taiwan): 2018~2065, available at https://www.ndc.gov.tw/en/cp.aspx?n=2E5DCB04C64512CC (last visited: 2019-12).
[9] Chari AV, et al., the Opportunity Costs of Informal Elder-Care in the United States New Estimates from the American Time Use Survey. Health Services Research, v50, pp871-882, 2015.
[10] Walter CS, et al., "Declines in motor transfer following upper extremity task-specific training in older adults," Experimental gerontology, vol. 116, pp. 14-19, 2019.
[11] Parmar MC. and Saikia N., "Chronic morbidity and reported disability among older persons from the India Human Development Survey," BMC geriatrics, Vol. 18(1), pp. 299, 2018.
[12] Bass, D.M., et al., "Negative caregiving effects among caregivers of veterans with dementia. American Journal of Geriatric Psychiatry," vol. 20(3), pp. 239–247.
[13] An Antonio, P., et al., "Lessons from the Arkansas Cash and Counseling Program: How the experiences of diverse older consumers and their caregivers address family policy concerns". Journal of Aging & Social Policy, vol. 22(1), pp. 1–17, 2010.
[14] Burton, et al., "Preventive health behaviors among spousal caregivers. Preventive Medicine," vol. 26, pp. 162–169, 1997..
[15] Mukai T, Hirano S, Nakashima H, Kato Y, Sakaida Y, Guo S, Hosoe S., "Development of a nursing-care assistant robot RIBA that can lift a human in its arms. In2010 IEEE/RSJ International Conference on Intelligent Robots and Systems," IEEE, pp. 5996-6001, 2010.
[16] Bostelman R, et al., "A multipurpose robotic wheelchair and rehabilitation device for the home," Proceedings of the IEEE/RSJ international conference on intelligent robots and systems, USA, pp 3348–3353, 2007.
[17] Bien ZZ and Lee SW, "Realization of Ageing-friendly Smart Home System with Computational Intelligence," In Computational Intelligence: Foundations and Applications pp. 3-9, 2010.
[18] Jung JW, Do JH, Kim YM, Suh KS, Kim DJ and Bien ZZ, "Advanced robotic residence for the elderly/the handicapped: Realization and user evaluation," In9th International Conference on Rehabilitation Robotics, ICORR 2005, pp. 492-495.
[19] Wang H and Kasagami F., "Careful-patient mover used for patient transfer in hospital," In International Conference on Complex Medical Engineering 2007, pp. 20-26, 2007.
[20] Peng SW, Lian FL and Fu LC., "Mechanism design and mechatronic control of a multifunctional test bed for bedridden healthcare," IEEE/ASME transactions on mechatronics, vol. 15(2), pp.234-41, 2009.
[21] Andrew Sivaprakasam et al., "Evaluation of the agile life patient transfer and movement system," (2009).
[22] Bruno S, José M, Filomena S, Vítor C, Demétrio M and Karolina B., "The conceptual design of a mechatronic system to handle bedridden elderly individuals," Sensors, vol. 16(5), pp. 725 2016.

[23] Ning M, Ren M, Fan Q and Zhang L. "Mechanism design of a robotic chair/bed system for bedridden aged," Advances in Mechanical Engineering, vol. 9(3) pp. 1-8, 2017.
[24] Kume, Y., Tsukada, S. and Kawakami, H., "Development of safety technology for rise assisting robot "Resyone Plus"," vol. 85, pp. 18-00344, 2018.
[25] Panasonic Resyone, available at https://news.panasonic.com/global/topics/2014/29420.html (last visited: 2019-12).
[26] World Health Organization, World Report on Disability, Malta, 2011.
[27] HIWIN Health Care, available at https://www.hiwin.tw/download/tech_doc/me/Medical_Equipment(E).pdf (last visited: 2019-12).
[28] Invacare, available at http://store.allinonemobility-shop.com/bebasy.html, (last visited: 2019-12)
[29] On Care Medical, available at https://www.oncaremedical.com/product/liftseat-powered-toilet-lift/ (last visited: 2019-12).
[30] Takahashi, Y., et al., "Psychological evaluation of simple self-transfer aid robotic system with horizontal movement system," IEEE International Symposium on Industrial Electronics, pp. 1925-1930, Bari (2010).
[31] Toyota Patient Transfer Assist, available at https://blog.toyota.co.uk/toyota-healthcare-robots-shown-in-japan/patient-transfer-assist (last visited: 2019-12).
[32] Toyota Patient Transfer Assist, available at https://www.cbsnews.com/pictures/rise-of-the-machines/32/ (last visited: 2019-12).
[33] Melvin, available at https://www.youtube.com/watch?v=G9oSZ5bjPWY (last visited: 2019-12).
[34] Melvin, available at https://www.youtube.com/watch?v=9mrq5lqX0vc (last visited: 2019-12).
[35] Mover transfer chair, available at http://www.ritzmedical.com/index.php?ws=showproducts&products_id=2639093&cat=Patient-Hoist-Sling (last visited: 2019-12).
[36] Mover transfer chair, available at http://www.topmedi.com/ (last visited: 2019-12).
[37] Lawton MP. And Brody EM., "Assessment of older people: self-maintaining and instrumental activities of daily living," The gerontologist, vol. 9, pp. 179-86, 1969.
[38] Isira Naotunna, et al., "Meal Assistance Robots: A Review on Current Status, Challenges and Future Directions", IEEE/SICE International Symposium on System Integration (SII), pp. 211-216, 2015.
[39] Neater Solutions Ltd, "Neater", 2015. available at http://www.neater.co.uk/ (last visited: 2019-12).
[40] Topping, M., "An Overview of the Development of Handy 1, a Rehabilitation Robot to Assist the Severely Disabled," Journal of intelligent and robotic systems, vol. 34(3), pp. 253-63 2002.
[41] Mealtime Partners, Inc, "The Mealtime Partner Dining System," available at http://www.mealtimepartners.com/ (last visited: 2019-12).
[42] Obi Ltd, available at https://meetobi.com / (last visited: 2019-12).
[43] SECOM Co., Ltd., "My Spoon," 2000. available at https://www.secom.co.jp/english/myspoon/ (last visited: 2019-12).
[44] Neater Solutions Ltd, "Neater Eater Robotic V6," 2015. available at http://www.neater.co.uk/neater-eater-2-2/ (last visited: 2019-12).
[45] Assistive Innovations Ltd, "iEAT Feeding Robot," 2018. available at https://assistive-innovations.com/en/eatingdevices/ieat-feeding-robot (last visited: 2019-12).

Salman Masroor received the B.Eng. degree in Mechanical engineering from the Mehran University of Engineering and Technology, Jamshoro, Pakistan, in 2012. In 2015, he did MS from N.E.D University of science and technology, Karachi, Pakistan. Since 2016, he joined the Balochistan University of Engineering and Technology, Khuzdar, as a Lecturer, in the department of Mechanical engineering. He is currently working towards a Ph.D. degree in Mechanical Engineering at the National Taiwan University of Science and Technology, Taipei, Taiwan. His research interests include computer vision, mechatronics, mechanism design and analysis, and materials

Xiang-Min Tu was born in Taiwan, 1993. He received his B.S. degree in Mechanical and Electro-Mechanical Engineering from the Tamkang University, Taiwan, in 2015, and the M.S. degree in Mechanical Engineering from the National Taiwan University of Science and Technology, Taiwan, in 2020. His research interests include gaze tracking detect, robot control and computer vision.

Bahrudin was born in Kediri, Indonesia in 1988. He earned the B.Eng. degree in Mechanical engineering from the University of Brawijaya, Malang, Indonesia, in 2012. Since 2014, he joined the Technical Implementation Unit for Instrumentation Development, Indonesian Institute of Sciences (LIPI) as a Researcher. Currently pursuing an M.Sc. degree in Mechanical Engineering at the National Taiwan University of Science and Technology, Taipei, Taiwan. His research interests include machine design, mechatronics, conversion energy, and instruments.

Chyi-Yeu Lin is a distinguished professor in the Department of Mechanical Engineering and the director of the Center for Intelligent Robotics in National Taiwan University of Science and Technology (NTUST). He received his Ph.D. degree from the University of Florida in 1991. From 1991 and 2001, his major research interests were structural optimization and evolutionary methods. After 2001, he switched his interests to intelligent robotics. He and his research team created many intelligent robots including two androids and two dual-wheeled robots that performed in the world's first robot theater involving male and female bipedal humanoid robots in December 27, 2008.

Information for Authors

Aim and Scope

The ***i*Robotics** is an official journal of Robotics Society of Taiwan (RST) and is published quarterly. The ***i*Robotics** will consider high quality papers that deal with the theory, design, and application of intelligent robotic system, intelligent artificial system, and extension theory systems ranging from hardware to software. Survey and expository submissions are also welcome. Submission of a manuscript should indicate that it has been neither published, nor copyrighted, submitted, accepted for publication elsewhere (except that the short version may have been presented at the conferences). Submitted manuscripts must be typewritten in English and as concise as possible.

Process for Submission of a Manuscript

The ***i*Robotics** publishes two types of articles: regular papers and technical notes. All contributions are handled in the same procedure, where each submission is reviewed by an associate editor who makes an initial decision to send the manuscript out for peer review or to reject without external review. Articles can be rejected at this stage for a variety of reasons, such as lack of novelty, topics outside the scope of the Journal, flaws in the scientific validity, or unprofessional presentation. We are therefore not normally able to provide authors with feedback on rejected manuscripts. If the associate editor believes the article may be of interest to our readers, it is then sent out for external peer review by at least two external reviewers. According the recommendation of the associate editor, the Editor-in-Chief makes the final decision. All manuscripts should be submitted electronically in Portable Document Format (PDF) through the manuscript submission system at [http://www.rst.org.tw]. The corresponding author will be responsible for making page proof and signing off for printing on behalf of other co-authors. Upon acceptance of a paper, authors will be requested to supply their biographies (100 to 200 words) and two copies of the final version of their manuscript (in DOC format and in PDF format).

Style for Manuscript

Papers should be arranged in the following order of presentation:

1) First page must contain: a) Title of Paper (without Symbols), b) Author(s) and affiliation(s), c) Abstract (not exceeding 150 words for Papers or 75 words for Technical Note, and without equations, references, or footnotes), d) 4-6 suggested keywords, e) Complete mailing address, email address, and if available, facsimile (fax) number of each author, f) Preferred address for correspondence and return of proofs, and g) Footnotes (if desired).
2) The text: Submitted manuscripts must be typewritten double-spaced. All submitted manuscripts should be as concise as possible. Regular papers are normally limited to 26 double-spaced, typed pages, and technical notes are 12 double-spaced, typed pages. Please see the Page charge for those who want to submit long papers.
3) Acknowledgements of financial or other support (if any).
4) References: References should be numbered and appear in a separate bibliography at the end of the paper. Use numerals in square brackets to cite references, e.g., [15]. References should be complete and in the style as follows.
   [1] C. C. Lee, "Fuzzy logic in control systems: Fuzzy logic controller - Part I," *IEEE Trans. Syst. Man Cybern.*, vol. 20, no. 2, pp. 404-418, 1990.
   [2] C. Golaszewski and P. Ramadge, "Control of discrete event processes with forced events," in *Proc. of 26th IEEE Conf. Decision and Control*, Los Angeles, CA, pp. 247-251, Dec. 1987.
   [3] P. E. Wellstead and M. B. Zarrop, *Self-Tuning Systems*, New York: Wiley, 1991.
   [4] Project Rezero, available at http://rezero.ethz.ch/project_en.html (last visited: 2017-07).
5) Tables
6) Captions of figures (on separate sheet of paper)

Style for Illustrations

1) It is in the author's interest to submit professional quality illustrations. Drafting or art service cannot be provided by the Publisher.
2) Original drawings should be in black ink on white background. Maximum size is restricted to 17.4 by 24.7 cm. Glossy prints of illustrations are also acceptable.
3) All lettering should be large enough to permit legible reduction of the figure to column width, sometimes as small as one quarter of the original size. Typed lettering is usually not acceptable on figures.
4) Provide a separate sheet listing all figure captions, in proper style for the typesetter, e.g., "Fig. 5. The error for the proposed controller."
5) Illustrations should not be sent until requested, but authors should be ready to submit these immediately upon acceptance for publication.

Page Charges

After a manuscript has been accepted for publication, the author's company or institution will be approached with a request to pay a page charge to cover part of the cost of publication. The charges include:

1) NT$ 5000 for the 10 printed pages of a full paper or for the 6 printed pages of a short paper, and the excess page charge of NT$ 1500 per extra printed page for both full and short papers.
2) For color figures or tables, an additional cost will be charged. The cost, depending on the number of color figures/tables and the final editing result, will be given upon the acceptance of this paper for publication.

Copyright

It is the policy of the RST to own the copyright of the technical contributions. It publishes on behalf of the interests of the RST, its authors, and their employers, and to facilitate the appropriate reuse of this material by others. Authors are required to sign a RST Copyright Form before publication.

Manuscripts (in PDF Format) Submission Website: http://www.rst.org.tw

Editor-in-Chief: Prof. Ching-Chih Tsai, Department of Electrical Engineering, National Chung Hsing University, Taiwan
Email: cctsai@nchu.edu.tw
Prof. Tzuu-Hseng S. Li, Department of Electrical Engineering, National Cheng Kung University, Taiwan
Email: thsli@mail.ncku.edu.tw

Managing Editor: Dr. Feng-Chun Tai, Department of Electrical Engineering, National Chung Hsing University, Taiwan
Email: fctai@nchu.edu.tw

iRobotics

VOLUME 2, NUMBER 4 DECEMBER, 2019

CONTENTS

REGULAR PAPERS

TECHNICAL NOTE

iRobotics Volume 2, Number 4, DECEMBER, 2019